MODELING OF RADIATION-INDUCED SEGREGATION (RIS) IN NI-CR ALLOYS

A Thesis

by

MERVE GENCTURK

Submitted to the Graduate and Professional School of
Texas A&M University
in partial fulfillment of the requirements for the degree of

MASTER OF SCIENCE

Chair of Committee,	Karim Ahmed
Committee Members,	Lin Shao
	Pavel Tsvetkov
	Michael Demkowicz
Head of Department,	Michael Nastasi

August 2021

Major Subject: Nuclear Engineering

ABSTRACT

In the nuclear reactor core, materials perform under harsh operating environments, including high temperature, high stress, and severe radiation damage. These conditions weaken the operational performance of the material. Radiation-induced segregation (RIS) is one of the primary material degradation problems in nuclear reactors. Irradiation creates excess vacancy and interstitial point defects in alloys. These point defects can be canceled by mutual recombination or annihilation of defects at grain boundaries, surfaces, or dislocations. Consequently, irradiation gives rise to point defect fluxes toward the sinks, leading to enrichment or depletion of alloying elements at defect sinks. For Ni-Cr alloys, the depletion of Cr at grain boundaries can cause irradiation-assisted stress corrosion cracking (IASCC). This is one of the problems associated with RIS. Thus, a quantitative understanding of RIS is crucial for the design and development of nuclear materials. To better understand RIS in Ni–Cr alloys, the rate theory approach is employed. The balance equations for point defects and alloy atoms were solved simultaneously using a fully-coupled and fully-implicit scheme implemented in the Multiphysics Object-Oriented Simulation Environment (MOOSE) framework, considering the combined effects of dose rate, temperature, grain size, sink density, and production bias. Simulations have been conducted and compared with the experimental data. We demonstrate a strong dependence of RIS on size, production bias, and temperature. It was shown that the magnitude of enrichment/depletion of Ni/Cr at the boundary increases with size, and the width of the enrichment/depletion layer also increases with size. As the temperature decreases, RIS becomes more apparent with higher segregation of Ni and depletion of Cr at the boundary as the production bias increases. It is also noteworthy to the point that RIS shows dependency on the irradiation type and conditions. Adding different sink density tend to alter the width of the enrichment/depletion layer of RIS. Moreover, when surface and size effects are considered, qualitative differences in the irradiation response of materials to different irradiation types are expected. Here, we proved that, in addition to its known dependence on material and size/microstructure, the surface/boundary sink strength is dependent on irradiation type.

DEDICATION

"To my parents"

ACKNOWLEDGMENTS

I would like to thank my committee chair, Prof. Karim Ahmed, and my committee members, Prof. Lin Shao, Prof. Pavel Tsvetkov, and Prof. Michael Demkowicz, for their guidance and support throughout the research.

My sincere thanks also go to my friends and colleagues and the department faculty and staff for making my time at Texas A&M University a great experience.

Finally, thanks to my mother and father. Words cannot express how much I appreciate their support and encouragement.

CONTRIBUTORS AND FUNDING SOURCES

Contributors

This work was supported by a thesis committee consisting of Professor Karim Ahmed [advisor] and Professors Lin Shao, Pavel Tsvetkov of the Department of Nuclear Engineering, and Professor Michael Demkowicz of the Department of Materials Science and Engineering, Texas A&M University.

NOMENCLATURE

RIS	Radiation Induced Segregation
Ni	Nickel
Cr	Chromium
TNES	Thermal Non-equilibrium Segregation
SIA	Self-interstitial atom
FP	Frenkel Pairs
IKE	Inverse Kirkendall Effect
DPA	Displacements per atom
TEM	Transmission Electron Microscopy
SRRT	Spatially Resolved Rate-Theory
LWRs	Light Water Reactors
NRC	Nuclear Regulatory Commission
IASCC	Irradiation-Assisted Stress Corrosion Cracking
MOOSE	Multiphysics Object-Oriented Simulation Environment

TABLE OF CONTENTS

Page

LIST OF FIGURES

FIGURE Page

1. INTRODUCTION

1.1 Motivation and Objectives

Nuclear power reactors are not directly emitting carbon dioxide and therefore, they are a fundamental element of a clean energy strategy. Over the past two decades, nuclear energy has contributed 20 percent of electrical generation in the US [7]. Global energy demand is proliferating, exceptionally cleanly generated energy. While nuclear power plays a vital role in the reliable and sustainable energy that the world demands, understanding long-term environmental degradation and predicting material performance are essential.

Most nuclear reactors were completed between 1970 and 1980, nearing their lifetimes. Nuclear Regulatory Commission (NRC) issues licenses for commercial nuclear reactors to operate for 40 years, and these licenses can be extended for 20 years more. Building new nuclear reactors are costly, and their long construction times are challenging. Additionally, extending the operating lifetimes of those reactors beyond 60 years is vital to support energy demands [7]. Therefore, the industry is concentrating on renewals to operate beyond their lifetime. For example, in 2019, Florida Power&Light's renewal process application for Turkey Point Nuclear Units is approved by NRC. This approval allows the utility to operate units 3 and 4 until 2052 and 2053, respectively [8]. It should be noted that it was the first time NRC had issued renewed licenses allowing reactor operation from 60 to 80 years.

To sustain the safety and reliability of nuclear reactors, predict and measure changes in materials is more critical than ever. In the nuclear reactor core, materials perform under harsh operating environments, including high temperature, high stress, and severe radiation damage. These conditions decrease the operating performance of the material and cause failures in the alloy systems. Developing efficient and more reliable nuclear power systems depends on the proper choice of materials that work under harsh conditions [9] [10] [11] [12] [13] .

Nuclear fission is the primary process of generating nuclear energy. Fission gives rise to various

radiation (i.e., fission products, neutrons, and gamma rays), affecting materials. Fission product damage is limited to the fuel due to where they originated. Gamma radiation can raise the temperatures of components and cause corrosion problems. However, they have insignificant importance for displacement damage. Neutrons are the main source of displacement damage. Displacement damage eventually can induce local microstructure and composition changes near grain boundaries, voids, defects and dislocations, and this phenomenon is known as radiation induced segregation (RIS). These changes can degrade materials inside the nuclear reactor core and its construction components [14] [9] [15] [16] [4].

The main purpose of this study is to model and simulate radiation induced segregation (RIS) to better understand microstructure changes in materials and investigate the effect of size, dose rate, production bias, and temperature on the response of materials to irradiation. In this study, we utilize Ni-Cr alloys as a model system. Ni-Cr binary alloys provide significant strength and toughness advantages at high temperatures, moreover excellent corrosion resistance [7]. Due to their excellent corrosion resistance at high temperatures, Ni-Cr alloys are used for steam generator tubes and core internals. This highlights the importance of Ni-Cr alloys. Nevertheless, despite its numerous advantages, radiation can lead to the degradation of Ni-Cr alloys mechanical properties. To take the most striking example, Ni-Cr alloys contain a high amount of Cr to strengthen corrosion resistance, and Cr depletion may drastically alter the corrosion resistance. The depletion of Cr at grain boundaries due to radiation is suspected of playing a role in irradiation-assisted stress corrosion cracking (IASCC) [17]. Significantly, IASCC is increasing concern in commercial nuclear reactors. Since corrosion is a significant factor considering the operation time of nuclear reactors, understanding the mechanism of radiation-induced segregation is required to guide the development of mitigation approaches [18] [3] [7][19] [20] [21] [22].

1.2 Contribution to Research

This work focuses on radiation-induced segregation (RIS) and calculates the concentration profiles of the components of a binary Ni-Cr alloy system and point defects. In this study, we utilize the spatially-resolved rate-theory modeling approach. Additionally, we applied the production bias model (PBM) to investigate radiation-induced segregation (RIS) and its effect on radiation damage. Moreover, we consider the effects of dose rate, temperature, defects recombination, and reactions with sinks in addition to production bias. In contrast to previous studies, we demonstrate that heterogeneous patterns can be developed in the steady-state concentrations of point defects, which in turn can trigger the formation of non-uniform distributions of solute atoms and extended defects. Therefore, we showed the importance of resolving the spatial dependence of both the underlying microstructure and irradiation defects to better understand the behavior of materials under irradiation. The present study makes noteworthy contributions to the dependence of RIS on size, production bias, and temperature.

Additionally, adding different sink density tend to alter the width of the enrichment/depletion layer of RIS. The magnitude of enrichment/depletion of Ni/Cr at the boundary increases with size, and the width of the enrichment/depletion layer also increases with size. As the temperature decreases, RIS becomes more apparent with higher segregation of Ni and depletion of Cr at the boundary as the production bias increases. It is also noteworthy to the point that RIS shows dependency on the irradiation type and conditions.

This work presents the importance of considering the combined effects of size, dose rate, production bias, and temperature on the response of materials to irradiation. This work will contribute to our understanding of radiation-induced segregation in order to determine better design and development of nuclear materials.

1.3 Thesis Layout

This work is organized as follows. In Section 2, background information regarding radiation-induced segregation is reviewed. In the first part of Section 2, radiation damage and characterization of irradiation was discussed in detail. Further, literature models which were developed to investigate radiation-induced segregation were summarized. Finally, Section 2 explains the simulation and models for understanding and predicting radiation-induced segregation in materials.

In Section 3, we introduced the development of the spatially-resolved rate-theory modeling approach. First, general equations and their definitions were presented, and then we discussed the initial and boundary conditions and model parameters.

In Section 4, the results obtained by solving the balance equations for point defects and alloy atoms using a fully-coupled and fully-implicit scheme implemented in the Multiphysics Object-Oriented Simulation Environment (MOOSE) framework presented and discussed.

Lastly, in Section 5, summary and concluding observations are represented, and recommendations for future studies are given.

2.1 Radiation Damage

Radiation damage describes the state of the material irradiated by energetic neutrons, ions or electrons. Energy and mass of bombarding species make effect on displacement per atom which is related to radiation damage in material. The collisions between lattice atoms and energy particles lead to atoms displace from its site. Moreover, this displaced atoms leave a vacancies behind and rest in the lattice as an interstitial atoms. Vacancies and interstitial atoms are produced in this way in equal numbers are called Frenkel Pairs. Frenkel Pairs can be eliminated by mutual annihilation. However, recombination is not perfect all the time. TEM image captured from irradiated elemental Ni shows void microstructure in elemental Ni after 1.5 $MeV\ Ni^2+$ ion bombardment at 773 K to a fluence of 1.5e16 $ions/cm^2$ is illustrated in Fig. 2.1 [1]. Interstitials are exceptionally mobile than vacancies, hence they can interact with sinks before vacancies. Vacancies that are less mobile than interstitials can interact with each other and cause void swelling problem [14] [3] [9].

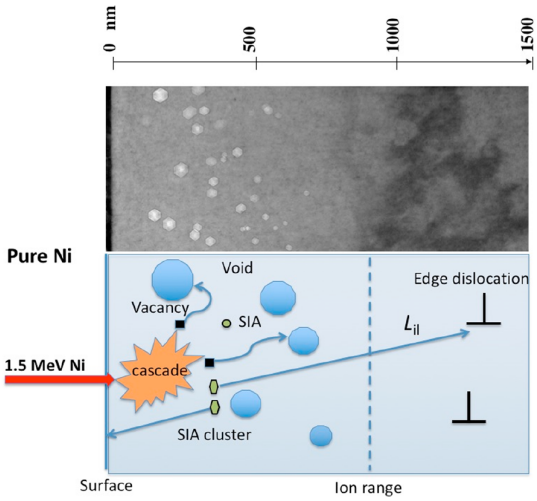

Figure 2.1: Void structure in elemental Nickel. Reprinted with permission from [1]

Fig.2.2 shows void structures of irradiated Ni-5Cr and Ni-18Cr alloys. [2].

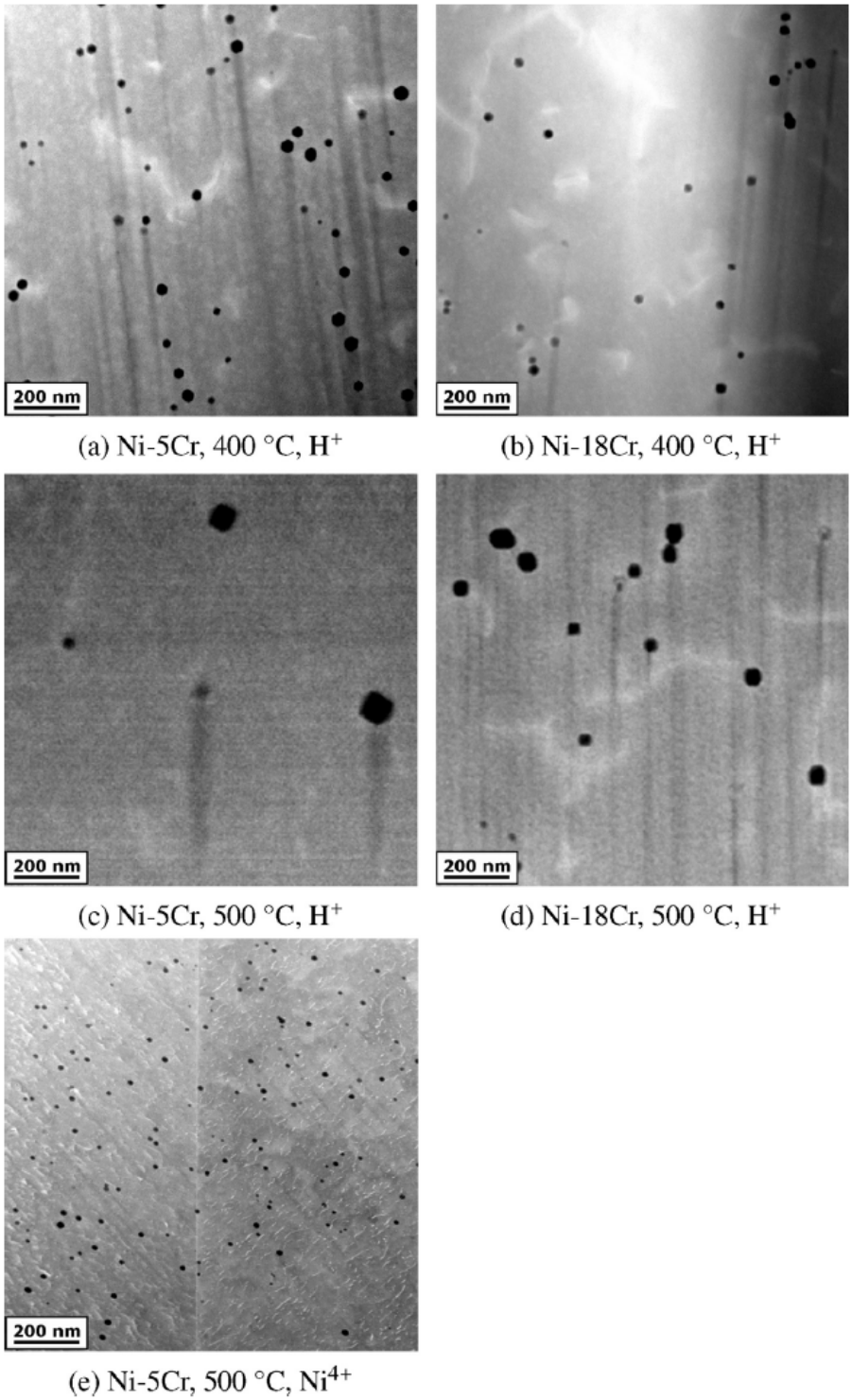

(a) Ni-5Cr, 400 °C, H^+

(b) Ni-18Cr, 400 °C, H^+

(c) Ni-5Cr, 500 °C, H^+

(d) Ni-18Cr, 500 °C, H^+

(e) Ni-5Cr, 500 °C, Ni^{4+}

Figure 2.2: Void structures of irradiated Ni-Cr binary alloys. Reprinted with permission from [2]

2.1.1 Grain Size Effect on Radiation Tolerance

Singh et al. [23] carried out several experiments on austenitic stainless steel with the dispersions of fine aluminum oxide particles and without in order to show grain size effect on void volume swelling. They showed that the void formation is strongly influenced by grain size. In addition to that, void volume swelling is smaller in the samples containing particles. Therefore, their findings suggested that the presence of particles makes an additional contribution to the grain size effect. Moreover, the effect of grain size is more significant than the only considering void-denuded zone in the vicinity of the grain boundary. It is because void number density that away from the denuded zone decreases with decreasing grain size, and it could not be attributed to the void denuded zone. Furthermore, the reduction of point defects arises from not only the denuded zone but also from the entire grain due to the presence of grain boundary. Their work draws attention to grain refinement, which can lead to material profoundly resistant to swelling. In a comprehensive study of austenitic stainless steel, Singh et al. [24]. found that the void number density in the grain center under irradiation decreases considerably with decreasing grain size at any dose level. Together these studies provide important insights into the void number density is significant in larger grain than in smaller grain. Additionally, their results showed that void volume swelling decreases by reducing the grain size in electron irradiated austenitic stainless steel. Nevertheless, here, it is important to mention that the effect of the grain size on void swelling for electron irradiation and higher recoil energies generate different qualitative patterns. For example, for higher recoil energy cases, void swelling was observed to be considerably intensified in the vicinity of the void-denuded zone [25][26] [27]. Previous studies implied that the irradiation-induced defects diffuse and precipitated randomly in the form of dislocation loops and voids. However, experimental studies showed that the irradiation-induced defects precipitate highly heterogeneous during the low dose neutron irradiations [28]. Moreover, the microstructure is heterogeneous and also it is segregated. In other words, the dislocation and void densities are segregated from each other [29]. Nevertheless, understanding the mechanism of the early stages of irradiation-induced defects toward voids and dislocations is limited.

Standard rate theory (SRT) calculations of the steady-state point defect distributions near the planar perfect sink have been implemented by many researchers. These implementations also included internal sink density and the dislocation bias effects. Their results showed that the supersaturation of vacancy in the vicinity of the grain boundary increases quickly with increasing length from the grain boundary. Therefore, vacancy supersaturation reaches an asymptotic value at a certain length from the grain boundary [30] [31]. Grain size effect on void swelling under electron irradiation was attributed to the dislocation bias effect, i.e., the preferential absorption of interstitials by dislocations. Moreover, vacancy absorption at grain boundary creates a decrease in the vacancy concentration in the grain interior. Therefore, vacancy absorption generates a decrease in voids concentration and swelling. However, the dislocation bias model failed in explaining void swelling under neutron and ion irradiation, where cascade damage is dominant. Later, Woo and Singh showed that considering SIAs intracascade clustering is crucial for understanding void swelling under cascade damage conditions. Moreover, they demonstrated that such effect can be incorporated into SRT via the utilization of the concept of production bias [32] [33]. Additionally, Singh and Foreman pointed that the one-dimensional glide of SIA clusters plays an important role in the removal of SIA clusters that is necessary to maintain the driving force for the void swelling in the production bias model [34]. Singh et al. performed numerical calculations with the production bias model (PBM) to determine the grain size dependence of the local void swelling only in the grain interiors, excluding the void-denuded zone. In addition to this, they performed calculations for average void swelling, including the void denuded zone. Their results reveal that the model predictions for the grain size dependence of local void swelling and the average void swelling agree well with the experimental data [35]. Trinkaus demonstrated that consideration of production bias and one-dimensional glide of SIA clusters can reveal the enhanced swelling near the grain boundary under the cascade damage. Therefore, their results showed that this consideration creates a great depletion of SIAs and a corresponding vacancy increase in the region of a specific width near the void-denuded zone along the grain boundary. This was attributed to the source of the enhanced swelling in the peak zone in the vicinity of the grain boundary [36] [37].

2.2 Characterization of Irradiation

Run-in-reactor experiments are costly, and the handling of the radioactive material requires special treatment and equipment. Furthermore, it is complicated to set up reactor experiments to simulate the response of the material to transient and abnormal conditions such as in accident circumstances. Finally, the data collected from the experiments carried out in a specific reactor might be irrelevant to new reactor designs with different working conditions.

Radiation-induced segregation is a process that depends on the temperature and displacement rate. Results from earlier studies have indicated that ion irradiation is utilized to mimic neutron irradiation. However, due to their high dose rate, accelerated irradiation experiments can be completed in a matter of hours/days [38] [39]. A notable amount of radiation-induced segregation data has been investigated by electrons and heavy ions irradiations [40] [2] [4] [41] [21].

Fig. 2.3 should be treated with caution. A couple of points are worth mentioning here: Firstly, the proton damage rate is still flat after several grain boundaries and a large irradiated volume. Secondly, the dose rate of proton irradiation is approximately two orders of magnitude lower than the dose rate of electrons or ions. Therefore, these irradiations occur at different displacement rates, and the irradiation occurring at the same temperature will not display the same segregation results. Examining data from neutron irradiations and data from other particle irradiations must be considered carefully. Although different types of irradiation are used in studies since they show similar segregation results, each kind of irradiation has advantages and disadvantages compared to each other [3].

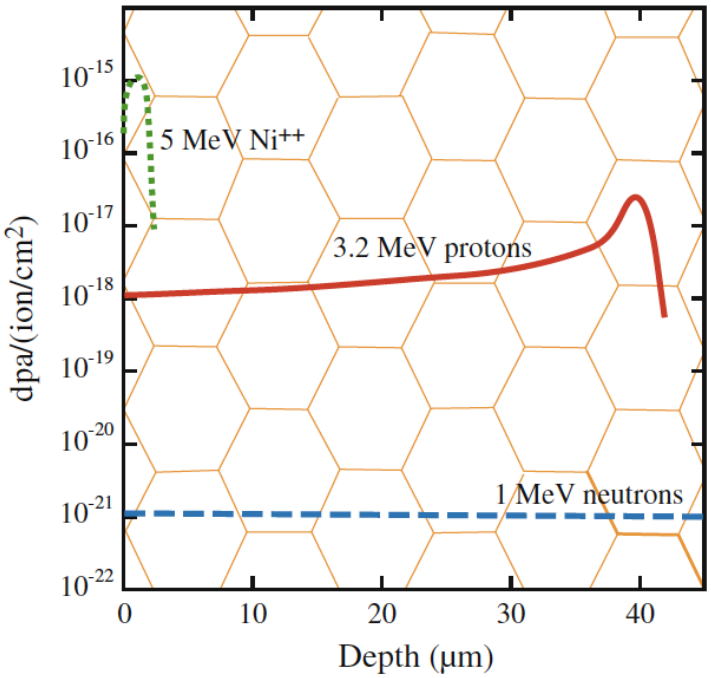

Figure 2.3: 3.2 MeV protons and 5 MeV Ni++ ions damage profiles in stainless steel. Reprinted with permission from [3]

2.2.1 Neutron Irradiation

The purpose of studying radiation-induced segregation (RIS) is to understand material degradation problems in nuclear reactors. For this reason, the most consistent data would come from neutron irradiations. However, producing neutron irradiation data for RIS is a time-consuming method because neutron irradiation experiments need years of exposure to reach the significant flux of the specific reactor. Moreover, the necessity of special sample handling is very high for neutron irradiation experiments due to high residual radioactivity. As a consequence, obtaining new data and developing new designs poses a challenge for researchers [9].

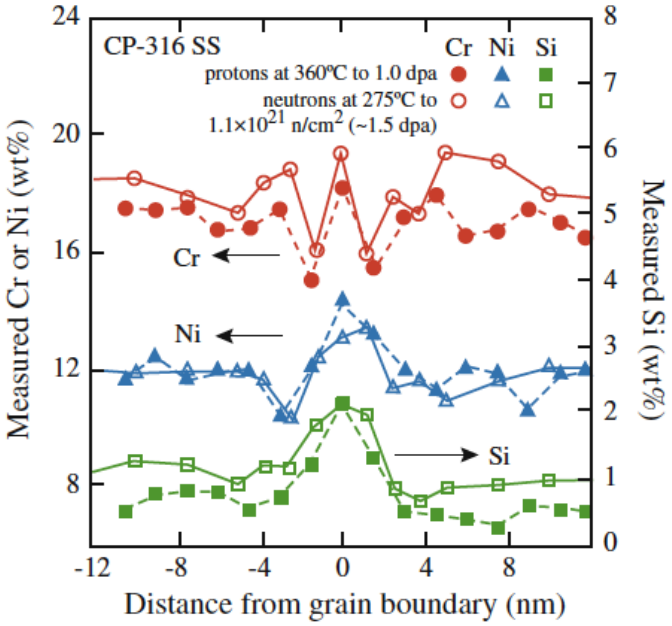

Figure 2.4: Cr, Ni, and Si segregation profiles with proton and neutron irradiation [4]. Reprinted with permission from [3]

2.2.2 Electron Irradiation

Electron irradiation is carried in a high-voltage transmission electron microscope. Since electron irradiation does not produce highly radioactive products, it provides great convenience for researchers. Moreover, they are advantageous because they reach the high dose rate in a short time. However, electron irradiation holds some limitations. Electrons are insufficient to create a cascade since their energy is limited to 1 MeV [3]. They can relocate only single atoms in the lattice site due to their low mass. Thus, point defects created by electron irradiation can easily migrate in the lattice and play a role in the segregation. Another potential problem is that electron irradiation causes significant changes in temperature due to the high dose rate compared to neutrons. Furthermore, electron irradiated materials show very wide segregation profiles compared to sample irradiated with neutrons. Fig 2.5 depicts electron and deuteron irradiation of the same alloy. It can be seen that segregation effect is more significant and more tapered nearby the grain boundary in the deuteron irradiated specimen [3].

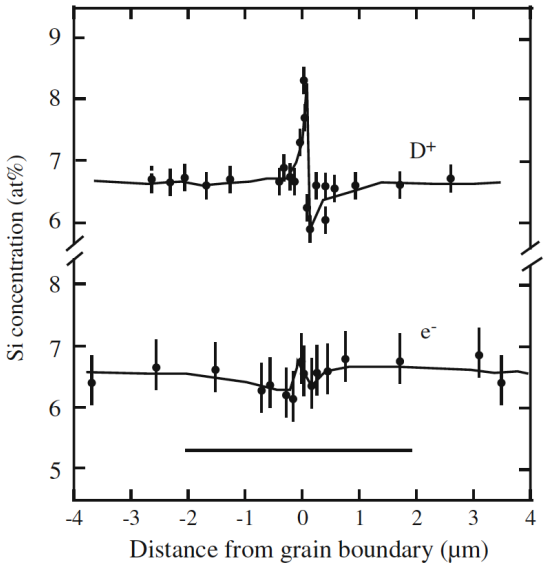

Figure 2.5: Segregation profile of deuteron and electron irradiated sample. Reprinted with permission from [3]

2.2.3 Proton Irradiation

The proton damage profile is relatively flat. It reflects a better displacement rate throughout the material, comparing to heavy ions. Furthermore, proton irradiation reflects the cascade better than electron irradiation since they have higher mean recoil energy than electrons. Fig. 2.6 depicts the damage profiles results for the proton and Ni-ion irradiations. It can be seen that the damage profiles of proton and Ni ion are similar [2] [3].

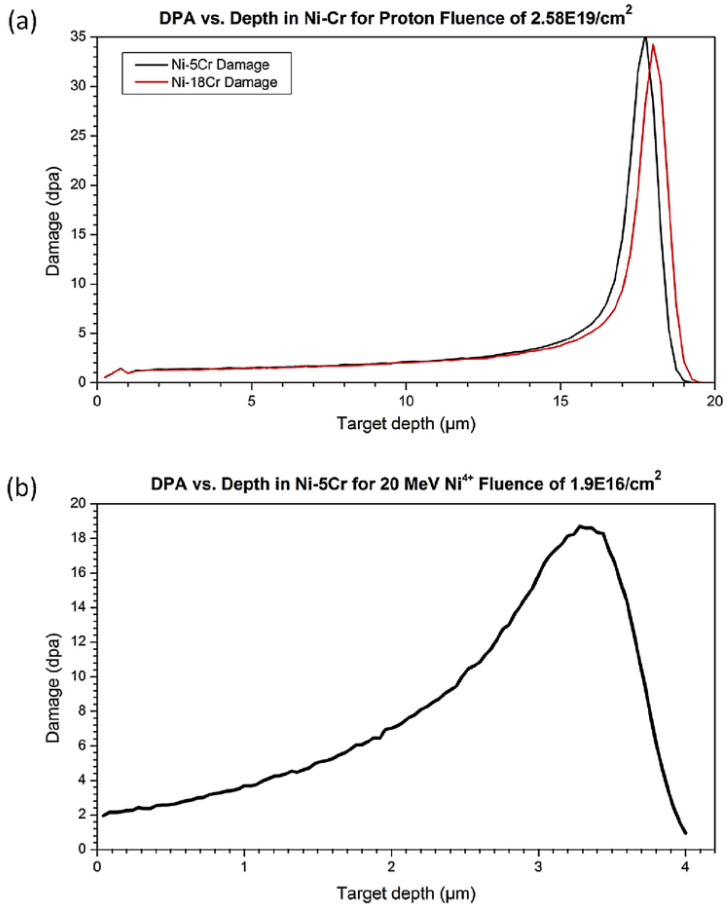

Figure 2.6: Damage profiles a) for Ni-Cr alloys irradiated with protons of 2 MeV b) for Ni-5Cr irradiated with Ni^{4++} of 20 MeV. Reprinted with permission from [2]

2.2.4 Heavy Ion Irradiation

Heavy ions are highly effective at creating dense cascades due to their high range of energy. Hence, they represent more suitable neutron cascade production [42]. Additionally, their displacement rate is significantly higher than the neutron irradiation, so it requires short irradiation times. These advantages give researchers cost and time-effective alternatives. However, using heavy ions has several disadvantages. There is a possibility of composition differences at high doses due to implanted ions. Also, the penetration depth of the heavy ions in the material is short compared to neutrons. For that reason, research needs to be done in a smaller area [3].

2.3 Thermal Non-Equilibrium Segregation (TNES)

Thermal non-equilibrium segregation occurs at grain boundaries due to heat treatments. Quenching after heat treatment may cause point defects to prevail in the microstructure. Subsequently, the concentration of vacancies and their local distribution changes. Since the grain boundaries act as a sink for vacancies, the vacancy concentration near the grain boundary decreases rapidly than the vacancy concentration within the grain. Thus, the vacancy gradient is developed, and the vacancies move towards the grain boundaries [14]. Allen et al. [14] studied three different materials, Ni–18Cr, Ni–18Cr–0.08P, and Ni–18Cr–9Fe in order to determine thermal non-equilibrium and radiation-induced segregation. They reported that thermal treatments to create TNES associated annealing at 1023 and 1373 K resulted from either furnace cooling or water quenching. TNES induced segregation in these Nickel-based alloys as well as TNES induced Cr enrichment reported for Iron-based austenitic alloys indicates that possible explanations for ‘W’ profile are light elements such as B-C-N or attractive forces that occur between Ni and Cr [14].

2.4 Radiation Induced Segregation (RIS)

Radiation Induced Segregation is first predicted by Anthony in 1970 [5], Anthony observed non-equilibrium segregation in aluminum alloys quenched from high temperature. They found that the flux of excess vacancy caused the zinc to enrich around the cavity (Fig. 2.7). They suggested segregation should be more vital under irradiation because the excess vacancy concentration can remain for an extended period.

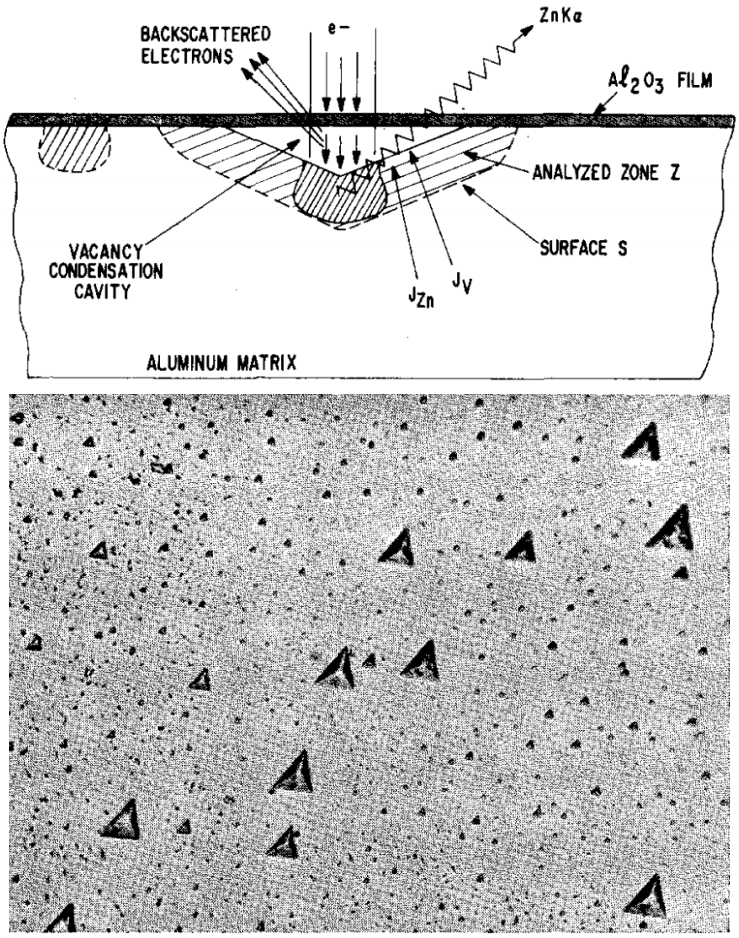

Figure 2.7: a) Schematic diagram of a vacancy cavity under the aluminum oxide film b) Quenched Al–Zn alloy sample, vacancy condensation cavities formed in Al. Reprinted with permission from [5]

First experimental observation was made by Okamoto et al.[43] They observed strain contrast around voids during austenitic stainless steel irradiation, as anticipated by Anthony.

Okamoto and Wiedersich measured chemical segregation at the surfaces of irradiated austenitic stainless steel by Auger spectroscopy [43]. Their analysis suggested that undersized atoms, which are easy to accommodate in interstitial sites, were moving towards point defect sinks while oversized atoms were moving away. Later, Marwick [44] pointed out that solute depletion by the vacancy flux toward point defect sinks could lead to solute segregation. Marwick coined this "inverse Kirkendall effect". In the Kirkendall effect, unequal mobility of chemical species give rise to defect flux. The inverse Kirkendall effect has the same mechanism, but defect flux drives a corresponding solute flux.

Radiation-induced segregation can cause depletion or enrichment of alloying elements in regions close by surfaces, dislocations, voids, and grain boundaries. Fig. 2.8 for profile of RIS in a 300 series stainless steel and depicts Cr depletion, also Ni and Si enrichment. Concentration changes in the vicinity of the grain boundary degrade the stability of the material [6]. Therefore, it is crucial to understand the effect of radiation-induced segregation mechanism.

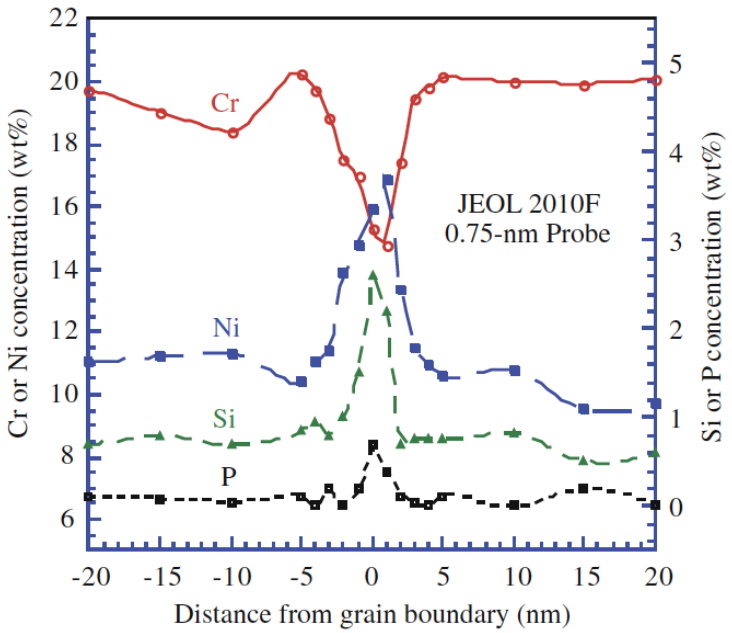

Figure 2.8: RIS concentration profile of irradiated 300 series stainless steel at $300°C$ [6]. Reprinted with permission from [3]

2.4.1 Modelling RIS

There are many developed models for radiation-induced segregation (RIS) in the literature. One of them is the rate theory approach, which numerically solves the coupled diffusion equations of defects and alloy elements. Mainly radiation-induced segregation models describe point defect concentration gradients and atom diffusion due to the local change in point defect concentration.

Perks et al. described one of the first models of RIS. Their model relied on the inverse Kirkendall effect that presumes that produced vacancies move toward a sink, and vacancies lead to a corresponding solute flux. In their model, they assumed interstitial kinetics are equal for all alloy components, and tracked all source and loss terms for atoms, interstitials, and vacancies. Therefore, enriched and depleted elements near the defect sinks are determined by vacancy diffusivities and compositions of alloy components. At low and intermediate temperatures, this model can predict RIS with proper parameters [45]. However, Allen et al. noted diffusivities are compatible with measurements of high-temperature diffusion coefficient in the Fe-based materials. Hence, it can be said vacancy flux is the primary driving force for segregation. In contrast to Fe-based materials, diffusivities in Ni-18Cr-9Fe are incompatible with high-temperature diffusion data. Consequently, they noted that the driving force concerning segregation is more complicated than the inverse Kirkendall effect. [14].

Later, Allen et al. calculated parameters of diffusion based on composition to include short-range order forces, and they modified Perk's inverse Kirkendall model to include composition-dependent migration energies. They introduced this new model as a modified inverse Kirkendall (MIK). The MIK model presents sufficient accuracy with experimental results in contrast to Perk's model at high temperatures. Nevertheless, input parameters were obtained from experimental fitting in the MIK model, limiting its applicability when experimental data is not available [46].

Nastar et al. fitted the vacancy diffusion parameters to thermodynamic and diffusion data and observed that interstitial diffusion contribution was essential to generate experimentally determined segregation. Like the MIK model, Nastar's model performs in good agreement with RIS data [9].

Later, Barnard et al. to determine the parameter values they used ab initio density functional

theory (DFT) calculations which combine the effects of vacancy and interstitial diffusion without taking parameters from experimental data. Their DFT based model presents that role of interstitial diffusion in RIS is essential [47].

3. MODELING METHODOLOGY

3.1 Equations for Radiation-Induced Segregation (RIS)

Under irradiation, interstitial and vacancy concentrations alter with time correspondent with the point defect balance equations. In this model, the continuity equations for the atomic species are coupled and solved concurrently. We will consider a binary Ni-Cr system [48].

$$\frac{dC_i}{dt} = -\nabla \cdot J_i + K_0 - K_{iv}C_iC_v - K_{is}C_iC_s \tag{3.1}$$

$$\frac{dC_v}{dt} = -\nabla \cdot J_v + K_0 - K_{iv}C_iC_v - K_{vs}C_iC_s \tag{3.2}$$

$$\frac{dC_{Cr}}{dt} = -\nabla \cdot J_{Cr} \tag{3.3}$$

The time derivatives in Eq.3.22, Eq.3.5, Eq.3.3 represent the evolution of the concentration of interstitials C_i, concentration of vacancies C_v, and concentration of Cr atoms C_{Cr}. On the right-hand side, first terms $\nabla \cdot J_i$, $\nabla \cdot J_v$ and $\nabla \cdot J_{Cr}$ are the divergences of the interstitial, vacancy and Cr atoms fluxes. The second term is a source term representing defect generation with rate constant of K_0. Third term $K_{iv}C_iC_v$ is a reaction term, referring to the recombination between interstitials and vacancies. The last term is also a reaction term, representing the reaction between the defect x and the sink s with a rate constant of K_{xs}.

3.2 Partial Diffusion Coefficients

In order to describe the alloy atom and defect fluxes, we need to write diffusion coefficients as the sum of the partial diffusion coefficients for the various species. We expressed the partial diffusion coefficients $D = dN$ form, and the spatial dependence resides in the N. In contrast, the d is composition independent and contains the kinetic and diffusion information [3].

$$D_I^{Ni} = d_{NiI} N_{Ni} \tag{3.4}$$

$$D_V^{Ni} = d_{NiV} N_{Ni} \tag{3.5}$$

$$D_I^{Cr} = d_{CrI} N_{Cr} \tag{3.6}$$

$$D_V^{Cr} = d_{CrV} N_{Cr} \tag{3.7}$$

$$D_{Cr}^{I} = d_{CrI} N_I \tag{3.8}$$

$$D_{Cr}^{V} = d_{CrV} N_V \tag{3.9}$$

Here, the expression for d_{CrV} and d_{CrI} are the vacancy and interstitial diffusivities for Cr and d_{NiV} and d_{NiI} are the interstitial and vacancy diffusivities for Ni. We can write the total diffusion coefficients for the various species:

$$D_V = d_{CrV} N_{Cr} + d_{NiV} N_{Ni} \tag{3.10}$$

$$D_I = d_{CrI} N_{Cr} + d_{NiI} N_{Ni} \tag{3.11}$$

$$D_{Cr} = d_{CrV} N_V + d_{CrI} N_I \tag{3.12}$$

3.3 Flux Equations

Assuming that the concentration gradient drives the flux, and for species k and j, D_{kj} contains the kinetics information.

$$J_k = \sum_{j=1} = D_{kj} \nabla C_k$$

Here, we coupled atom and defect fluxes. The flux of vacancies drives a flux of Ni and Cr atoms equal in size and opposite direction.

$$J_V = -(J_{Cr}^V + J_{Ni}^V) \tag{3.13}$$

Also, interstitials flux drives a flux of Ni and Cr atoms equal in size but same direction.

$$J_I = J_{Cr}^I + J_{Ni}^I \tag{3.14}$$

We represent the atoms and defects fluxes utilizing the partial and total diffusion coefficients.

$$J_V = d_{CrV}\Psi\Omega C_V \nabla C_{Cr} + d_{NiV}\Psi\Omega C_V \nabla C_{Ni} - D_V \nabla C_V \tag{3.15}$$

$$J_I = -d_{CrI}\Psi\Omega C_I \nabla C_{Cr} - d_{NiI}\Psi\Omega C_I \nabla C_{Ni} - D_I \nabla C_I \tag{3.16}$$

$$J_{Cr} = -D_{Cr}\Psi \nabla C_{Cr} + d_{CrV}\Omega C_{Cr} \nabla C_V - d_{CrI}\Omega C_{Cr} \nabla C_I \tag{3.17}$$

Here, Ψ is a thermodynamic factor and Ω is average atomic volume of the alloy. Also, we converted N into volume concentrations according to $N = \Omega C$,

3.4 Input Parameters

In this study, a Ni–5Cr binary alloy system was used as a model alloy. The segregation rate of element k by defect j is defined by a diffusivity of the general form:

$$d_{kj} = {d_0}^{kj} \exp(\frac{-{E_m}^{k,j}}{kT}) \tag{3.18}$$

Ni and Cr properties used in the radiation induced segregation model: lattice parameter is 0.352 nm, pre-exponential factor for Ni interstitial diffusivity 5.04e-8 m^2/s, pre-exponential factor for Cr interstitial diffusivity 3.20e-7 m^2/s, pre-exponential factor for Ni vacancy diffusivity 1.85e-4 m^2/s, pre-exponential factor for Cr vacancy diffusivity 2.26e-4 m^2/s, activation energy for Ni interstitial diffusivity 0.30 eV, activation energy for Cr interstitial diffusivity 0.37 eV, activation energy for Ni vacancy diffusivity 1.16 eV, activation energy for Cr vacancy diffusivity 1.10 eV,

vacancy formation energy 1.79 eV, interstitial formation energy 4.0 eV [49].

3.5 Initial and Boundary Conditions

In order to solve the set of continuity equations (Eq.3.22, Eq.3.5, Eq.3.3) suitable initial and boundary conditions are required. The initial concentrations of interstitials and vacancies are fixed to their thermal equilibrium values. Cr concentration is set to its nominal alloy composition.

Conditions at the boundaries are given below. At the free surface (x=0), the concentration of vacancy and interstitials are fixed to their thermal equilibrium values.

$$C_i(0,x) = {C_i}^{(eq)} \tag{3.19}$$

$$C_v(0,x) = {C_v}^{(eq)} \tag{3.20}$$

$$C_{Cr}(0,x) = C^0_{Cr} \tag{3.21}$$

At the other far end, the grain center, zero flux boundary conditions are considered for point defects and Cr atoms.

$$\frac{dC_I(t,x)}{dx} = \frac{dC_V(t,x)}{dx} = \frac{dC_{Cr}(t,x)}{dx} = 0 \tag{3.22}$$

4. RESULTS AND DISCUSSION

In this chapter, we will discuss the results of radiation induced segregation (RIS). First, We carried analysis to demonstrate the capabilities of the model. Then, we examined each parameter in greater detail. In this way, we were able to understand the effect of irradiation type and conditions.

We conducted simulations to investigate the effect of sink density, size, production bias, dose rate, and temperature on RIS in Ni-5Cr alloys. Three different temperatures were selected in order to examine the temperature effect, 473 K, 573 K, and 773 K. The reason for choosing these temperatures is that there are available experimental data for comparison for the model [47, 14, 49]. To good fit the experimental data, we assumed that the Ni and Cr atoms are randomly distributed throughout the grain and bulk sinks are uniformly distributed with a concentration of 1e18, 1e20, and 1e22 m^{-3} [2]. Our model predictions for the case of large grains and with bias agree well with the numerical results and experimental data in the literature, where Cr concentration at the boundary reported to be between 2-4% [49].

4.1 Size-Dependent Steady-State Patterns and Instabilities

Generally, larger grains are correlated with higher average defect concentrations. This is because of the high surface-to-volume ratio for smaller grain sizes. However, some expectations show that the transient vacancy concentrations in smaller grains are higher than their large counterparts, associating with the competition between the defect absorption by grain boundary and bulk recombination. Still, the steady-state vacancy concentration tends to accumulate fewer defects in the smaller grains [50]. Another anomaly related expectation is the accumulation of interstitials. Interestingly, unlike anomaly in the dependence of vacancy accumulation, this anomaly endures even under steady-state conditions [51]. This is due to fact that surfaces function as sinks for defects, and hence vacancy and interstitials concentrations increase in the center and decrease at the surfaces. Yet, as time proceeds, defect concentrations begin to show reverse trends, where vacancies lead to accumulating in the center and interstitials lead to accumulating in the vicinity of the surface. Here, we first demonstrated the anomaly in the dependence of interstitial accumulation on grain size, associating with instability. In order to examine the effect of the size and instability, we performed simulations at the lowest and highest dose rates (5.6e-6 and 1e-2 dpa/s) in 7 different sizes (20, 30, 100, 300, 500, 5000, and 7500 nm). The results of our simulations also show that instability is sensitive to grain size, dose rate, and production bias. Lastly, we discussed its effect on irradiation damage.

First, in order to show the role of grain size in the instability, simulations were performed with 1% production bias. The results of these simulations are summarized in Fig. 4.1 for various grain sizes at the dose rate of 5.6e-6 dpa/s. The steady-state vacancy concentration increases with grain size for all cases at the dose rate of 5.6e-6 dpa/s and 1% bias. On the contrary, the steady-state interstitial concentration decreases with grain size and develops the opposite trend for larger grain sizes (>500 nm). The instability under discussion can be seen effectively in 5000 and 7500 nm (see Fig. 4.1b).

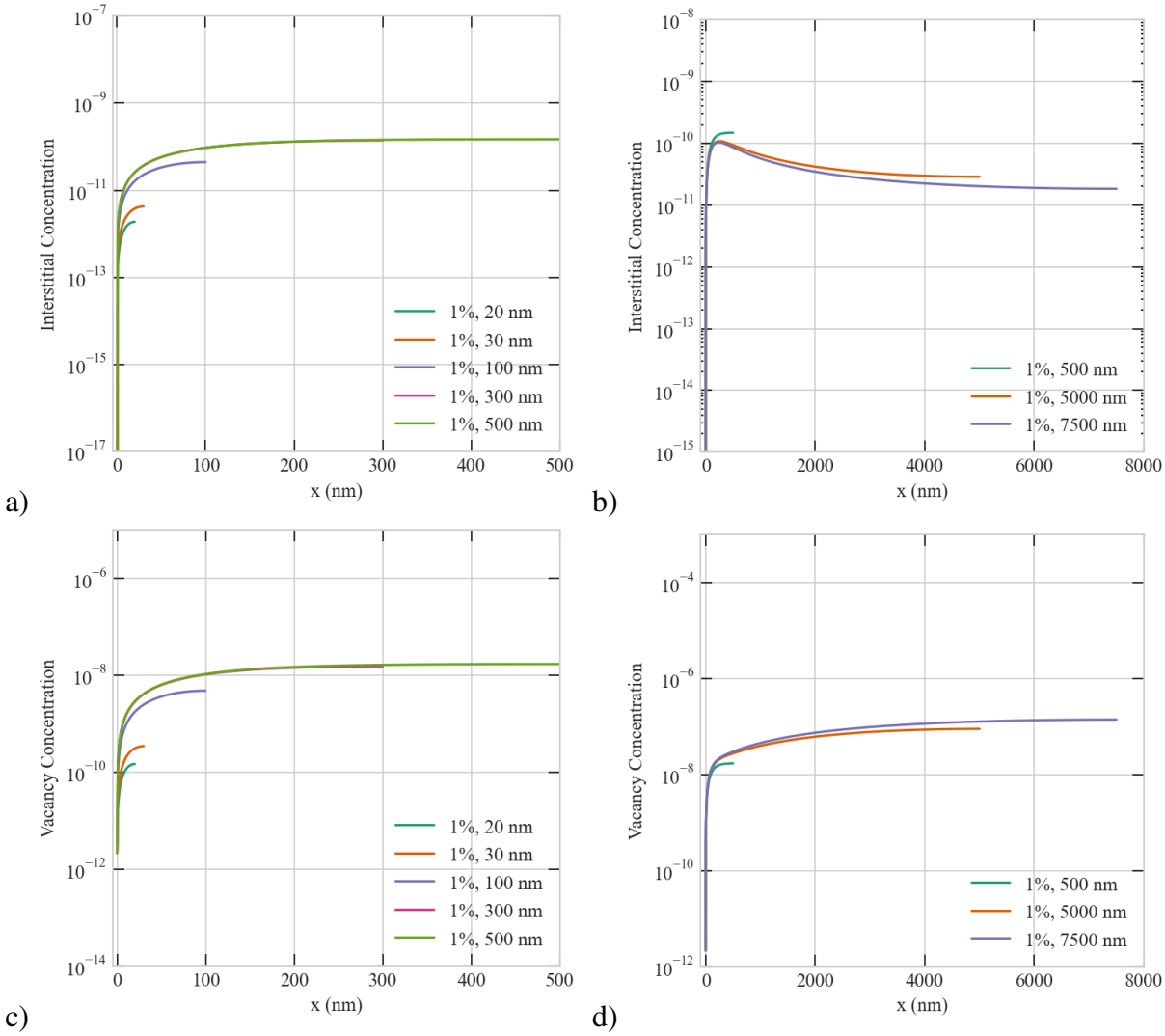

Figure 4.1: Effect of grain size on the steady-state concentration profiles of point defects at the dose rate of 5.6e-6 dpa/s and 1% production bias. Upper row: interstitials in a) fine grains, b) coarse grains. Lower row: vacancies in c) fine grains, d) coarse grains.

In order to better understanding sensitivity of instability to grain size, we simulated results at the dose rate of 1e-2 dpa/s and 1% bias and the results are summarized in Fig.4.2. At the dose rate of 1e-2 dpa/s, the steady-state interstitial concentration decreases with grain size as in 5.6e-6 dpa/s cases. However, the steady-state interstitial and vacancy concentration show opposite trends in 500 nm, and hence this instability appears effectively in 500 nm. Notably, the size at which instability appeared decreased with the dose rate. It demonstrates that instability is sensitive to

grain size and dose rate.

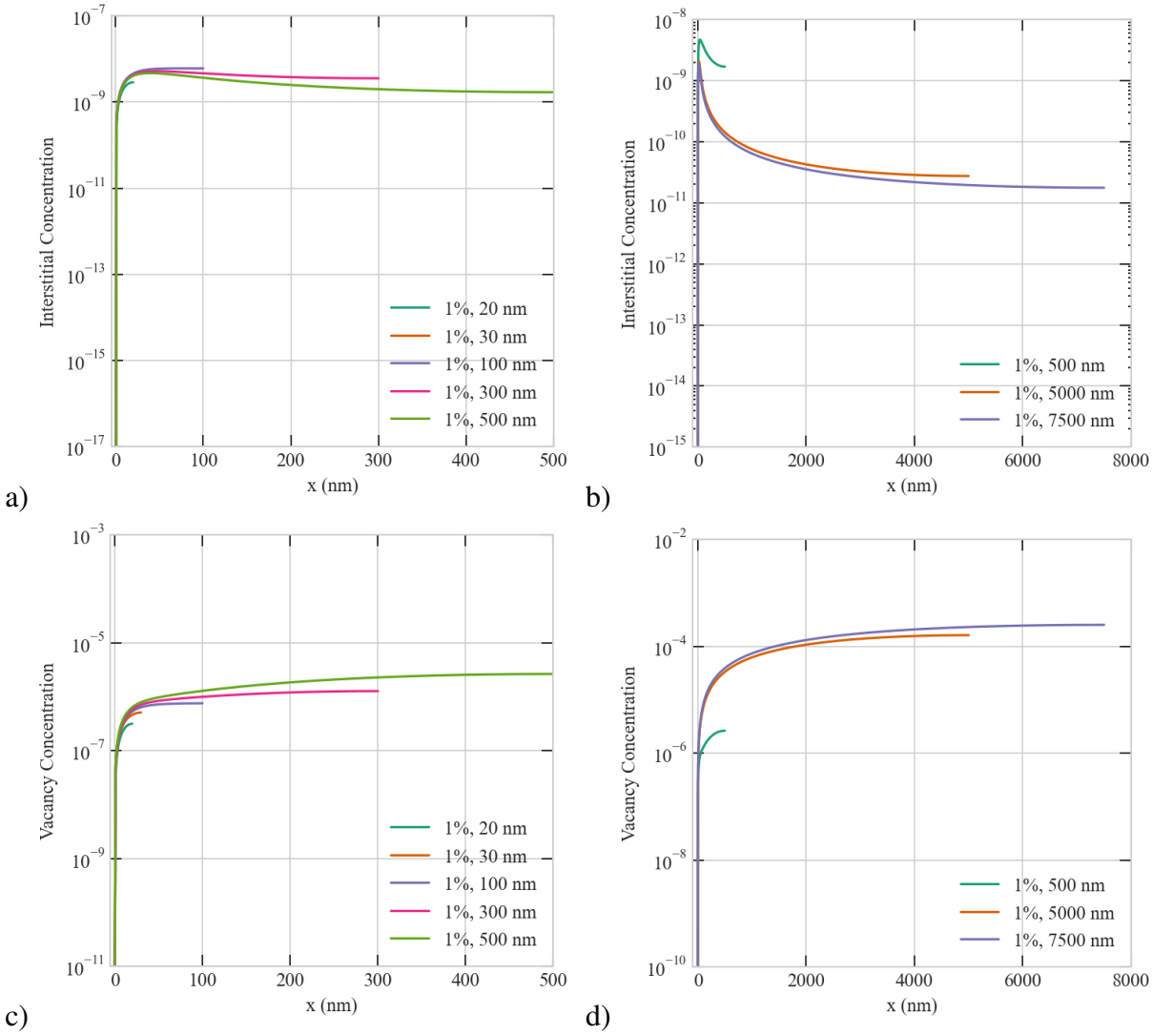

Figure 4.2: Effect of grain size on the steady-state concentration profiles of point defects at the dose rate of 1e-2 dpa/s and with 1% production bias. Upper row: interstitials in a) fine grains, b) coarse grains. Lower row: vacancies in c) fine grains, d) coarse grains.

So far, we have demonstrated that this instability is sensitive to grain size and dose rate. Here, we showed the sensitivity of instability on grain size with a higher production bias (20%). The results of these simulations are summarized in Fig. 4.3 and Fig. 4.4. Since the opposite trend based on this instability favors the separation of vacancies and interstitials, it will intensify the

possibility of clustering different point defects. For example, at the center of the domain, vacancies tend to cluster into voids or vacancy loops, and interstitials close to the boundaries tend to produce dislocation loops. At the dose rate of 5.6e-6 dpa/s and 20% production bias cases, this anomaly initially begins in 500 nm size. In 500 nm size, the steady-state concentration of interstitials decreases while the vacancy counterpart rises. However, this instability was observed only at larger grain sizes (>500 nm) for the same dose rate and 1% bias (see Fig.4.1) . Hence, effective size reduced with production bias. Furthermore, as the different irradiation types produce the different cascade structures and densities, higher production bias will break the symmetry of the balance of point defects. Therefore, instability results in the development of distinct steady-state profiles.

Fig. 4.4 shows effect of grain size on the steady-state concentration profiles of point defects at the dose rate of 1e-2 dpa/s and 20% production bias. Here, this instability, as discussed above, becomes more apparent above 100 nm. We demonstrated that at the dose rate of 5.6e-6 dpa/s and 20% production bias cases, this anomaly observed in 500 nm size. Moreover, our results showed that this instability is suppressed in with sizes smaller than 100 nm. Notably, the developed pattern of point defects promotes the clustering and formation of extended defects for larger sizes (>100 nm). However, we did not observe these anomalies in nanomaterials (<100 nm), and hence it provides new understanding of the stability of nanomaterials.

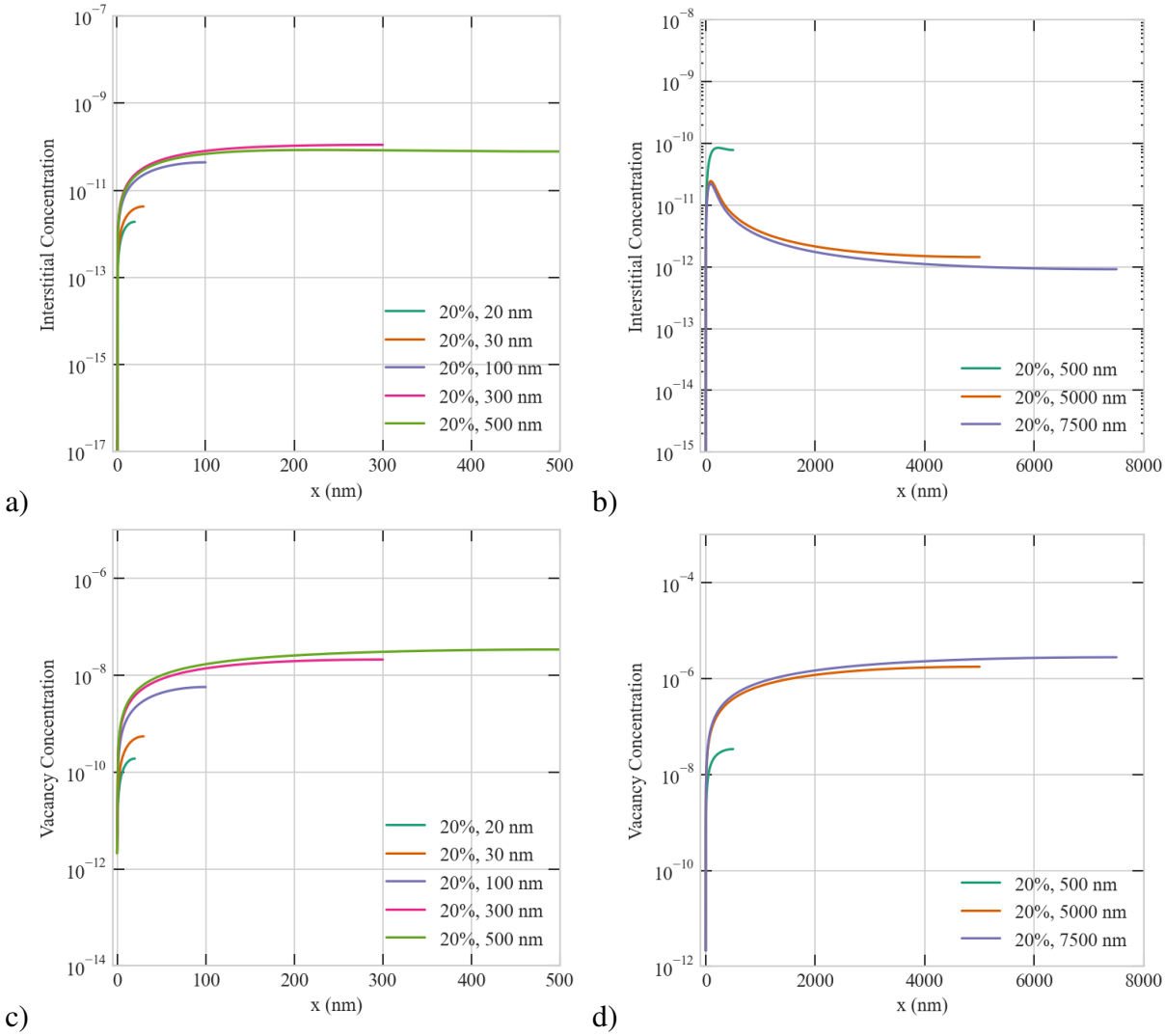

Figure 4.3: Effect of grain size on the steady-state concentration profiles of point defects at the dose rate of 5.6e-6 dpa/s and 20% production bias. Upper row: interstitials in a) fine grains, b) coarse grains. Lower row: vacancies in c) fine grains, d) coarse grains.

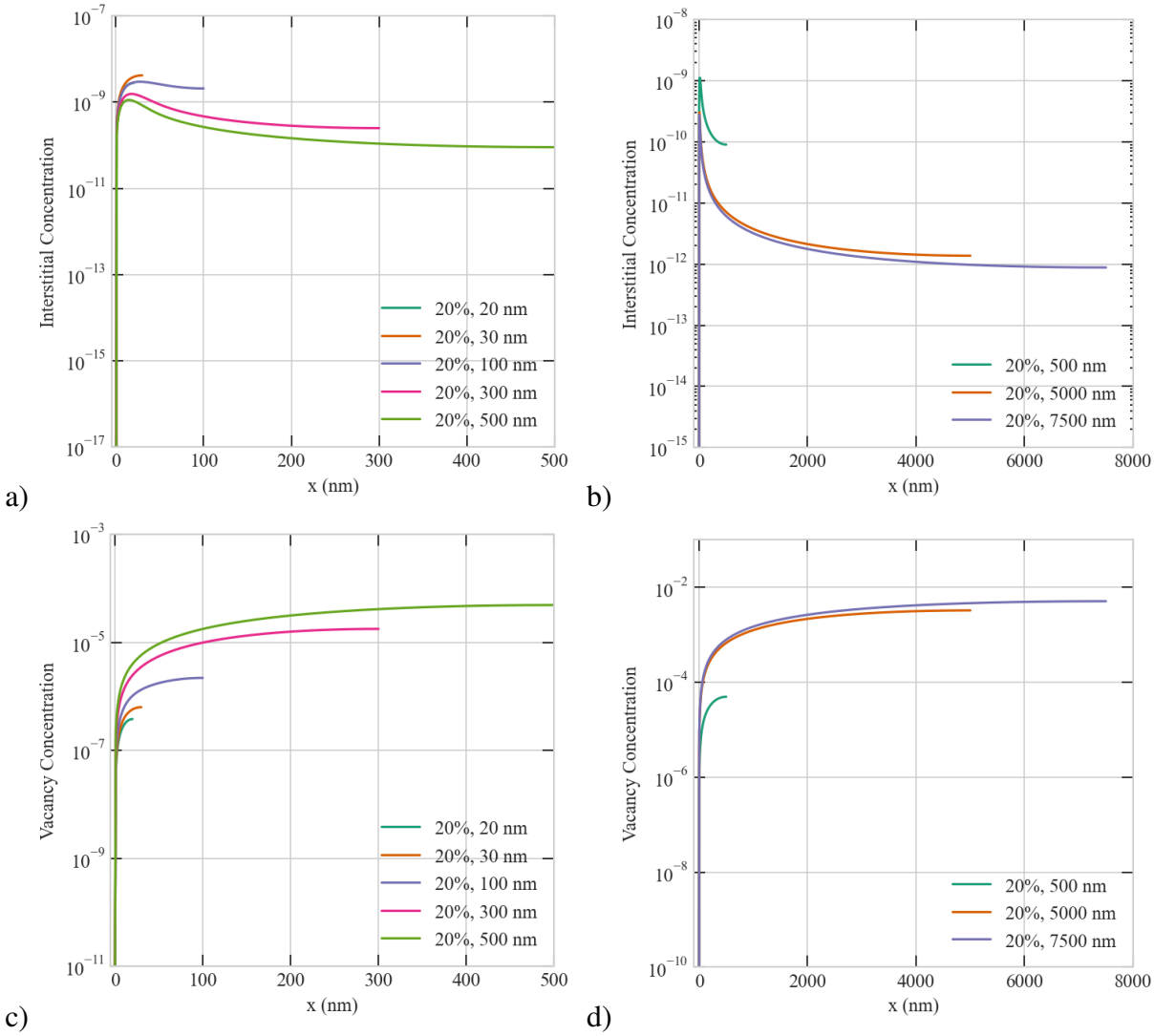

Figure 4.4: Effect of grain size on the steady-state concentration profiles of point defects at the dose rate of 1e-2 dpa/s and with 20% production bias. Upper row: interstitials in a) fine grains, b) coarse grains. Lower row: vacancies in c) fine grains, d) coarse grains.

4.1.1 Effect of Size and Instability on Cr concentration profile

We discussed the effect of instability and size in detail. Moreover, we pointed out that it would increase the irradiation damage. Here, we will examine the effect of grain size and instability on the Cr concentration profile.

In order to examine the grain size effect on Cr profile, we performed simulations at the lowest and highest dose rates (5.6e-6 and 1e-2 dpa/s) in 7 different sizes (20, 30, 100, 300, 500, 5000,

and 7500 nm).

Fig. 4.5 presents effect of grain size on the steady-state concentration profiles of Chromium in various grain size at the dose rate of 1e-2 dpa/s. The grain size effect on Cr concentration at the dose rate of 1e-2 dpa/s is remarkable for grain sizes smaller than 500 nm with 1% and 20% production bias. However, bias factor effect has become less significant for 5000 nm and 7500 nm sizes at the dose rate of 1e-2 dpa/s. On the other hand, the grain size effect on Cr concentration at the dose rate of 5.6e-6 dpa/s is less effective for all grain sizes with 1% bias cases. It becomes more significant for 5000 nm and 7500 nm with 20% bias cases. Furthermore, at the high dose rate of 1e-2 dpa/s, the Cr concentration at boundary becomes negligibly small at sizes above 500 nm. A possible explanation for these results may be the perfect sink boundary treatment is probably no longer valid.

Overall, it is apparent from Fig. 4.6 that at the dose rate of 5.6e-6 dpa/s size dependence has become more significant with bias factor. Additionally, Fig. 4.5 shows that the magnitude of Cr depletion and its size dependence are increased even with 1% bias at the dose rate of 1e-2 dpa/s. These findings demonstrate that there is a strong dependence of RIS on grain size and the instability, including on dose rate and production bias.

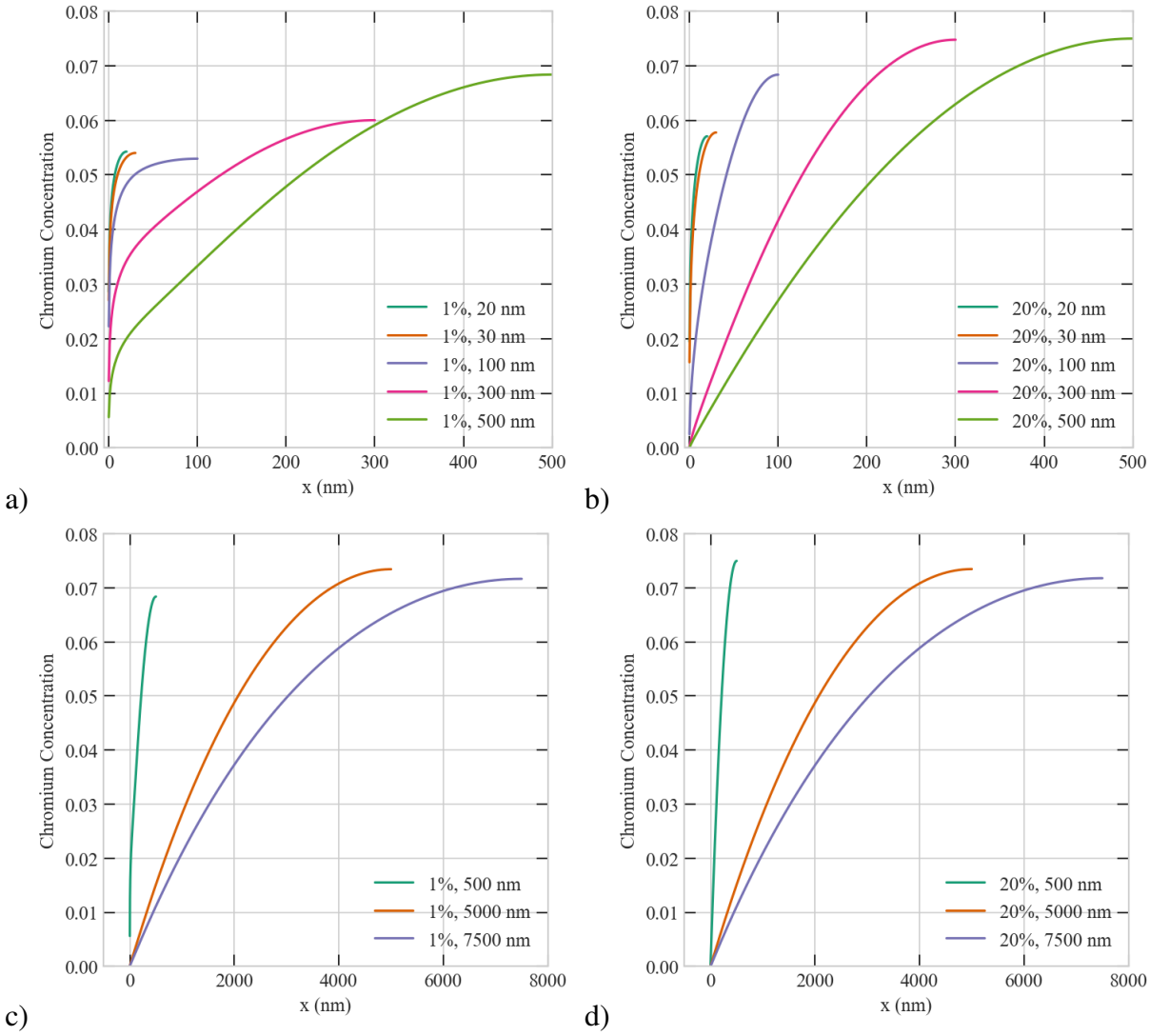

Figure 4.5: Effect of grain size on the steady-state concentration profiles of Chromium in various grain size at 1e-2 dpa/s a) 1% bias, Cr concentration in 20, 30, 100, 300, 500 nm b) 20% bias, Cr concentration in 20, 30, 100, 300, 500 nm c) 1% bias, Cr concentration in 500, 5000, 7500 nm d) 20% bias, Cr concentration in 500, 5000, 7500 nm

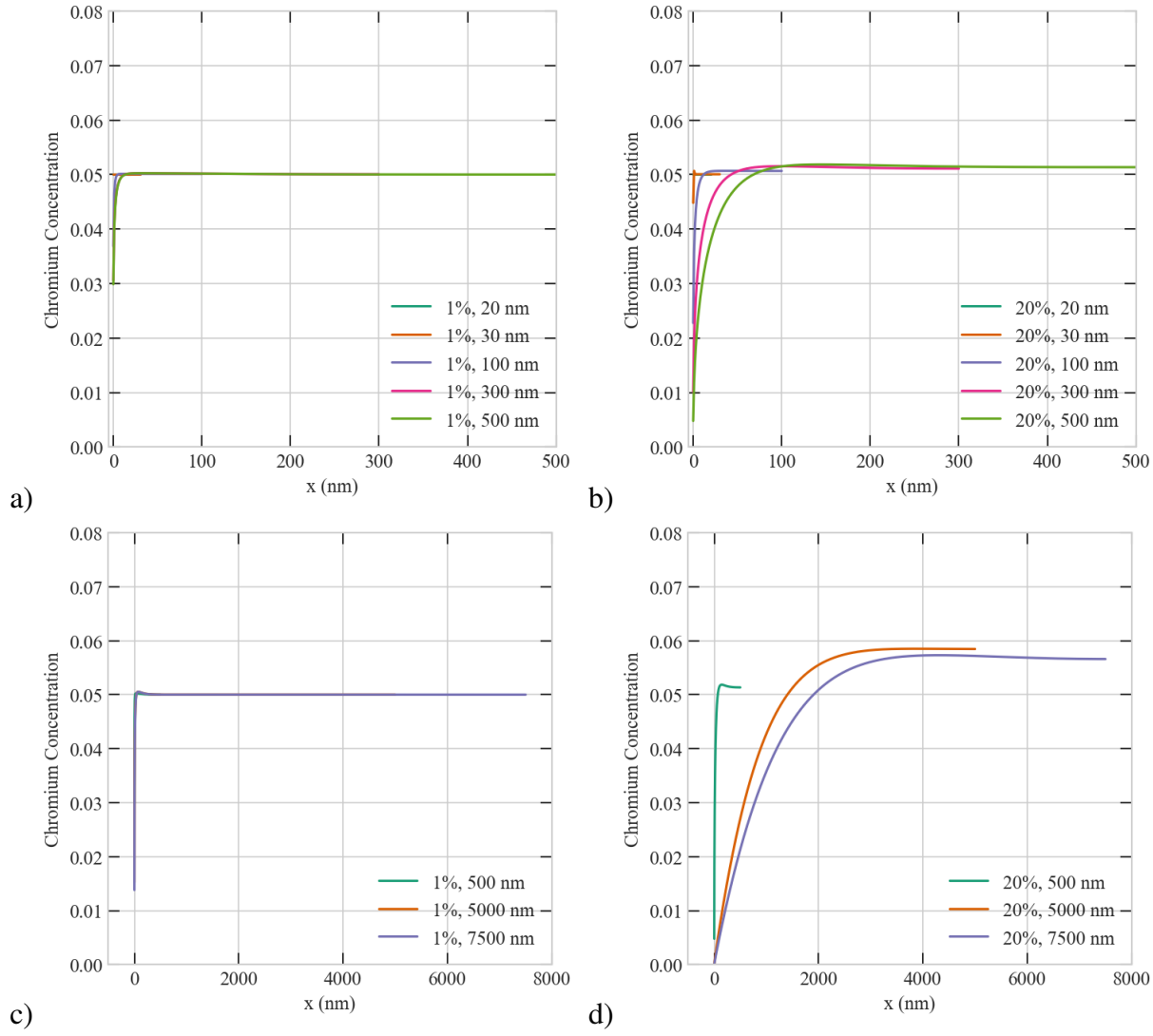

Figure 4.6: Effect of grain size on the steady-state concentration profiles of Chromium in various grain size at 5.6e-6 dpa/s a) 1% bias, Cr concentration in 20, 30, 100, 300, 500 nm b) 20% bias, Cr concentration in 20, 30, 100, 300, 500 nm c) 1% bias, Cr concentration in 500, 5000, 7500 nm d) 20% bias, Cr concentration in 500, 5000, 7500 nm

4.2 Effect of Dose Rate

In this section, effect of dose rate on RIS investigated. Before conducting a detailed examination, we first selected 100 nm and 500 nm grain sizes and performed the study with three different dose rates, 1e-2, 1e-4, and 5.6e-6 dpa/s at 773 K. Here, we also assumed sinks are present in the bulk uniformly distributed with a concentration of 1e18 m^{-3}.

A lower dose rate at a given temperature indicates that vacancies and interstitials are added to the lattice gradually. As a result, their recombination probability is decreased because interstitials will annihilate at sinks earlier. In other words, the role of the sink increases at the low dose rate [52]. In Fig. 4.7 and Fig. 4.8, the effect of dose rate is shown for two different grain sizes at a temperature of 773 K. Interstitial and vacancy concentrations are not significant enough to overcome the concentrations of thermal equilibrium at low dose rates. The vacancy concentration gradients in the vicinity of the boundary increases when the dose rate increases from 5.6e-6 dpa/s to 1e-2 dpa/s. As a result of this change in dose rate, Cr depletion at the boundary increases.

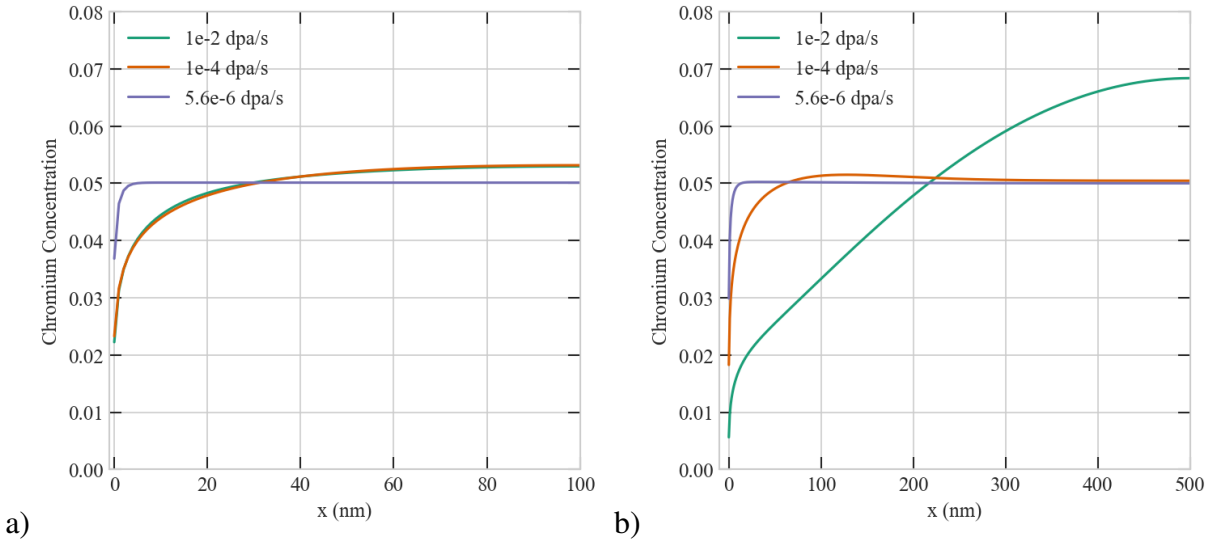

Figure 4.7: Effect of dose rate on the steady-state concentration profiles of Chromium a) Cr concentration in a 100 nm b) Cr concentration in a 500 nm

In Fig. 4.8b, at the dose rate of 1e-2 dpa/s interstitial concentrations start to show opposite trends in the vicinity of the boundary in 500 nm size. However, under the same parameters, this result was not observed in 100 nm size (see Fig. 4.8a). Taken together, these results suggest that there is an association between the dose rate and grain size. Additionally, these results indicate that we need to carefully analyze effect of the dose rate and grain size on Cr concentration profile.

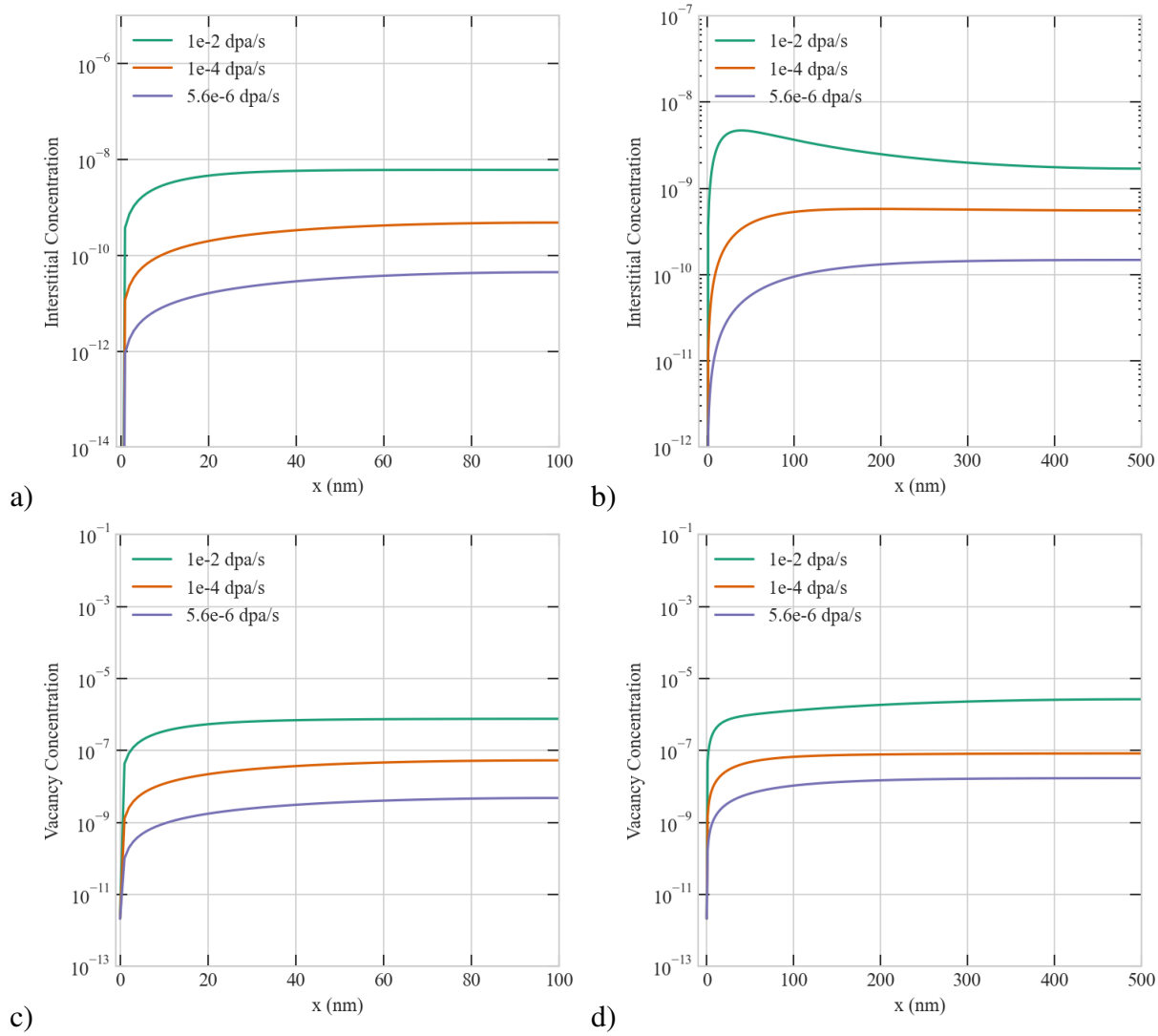

Figure 4.8: Effect of dose rate on the steady-state concentration profiles of point defects a) interstitial concentration in a 100 nm b) interstitial concentration in a 500 nm c) vacancy concentration in a 100 nm d) vacancy concentration in a 500 nm

4.3 Effect of Production Bias

We expanded our investigation to include the effect of production bias on RIS. Here, we introduced a production bias factor in order to simulate the effect of immobile clusters that result in unbalanced numbers of vacancies and interstitials [53]. To interpret the effect of production bias, simulations were performed with 1% 10% and 20% production bias at 773 K. Again, for these simulations we assumed sinks are uniformly distributed with a concentration of 1e18 m^{-3}. The

results of these simulations are summarized in Fig. 4.9, Fig. 4.10, Fig. 4.11, Fig. 4.12 at the dose rate of 1e-2, 1e-4 and 5.6e-6 dpa/s in 100 nm and 500 nm sizes. The simulations established a strong impact of production bias on the depletion of Cr.

Interstitials and vacancies can create immobile defect clusters under irradiation. Following this, interstitials are more likely to be lost in these clusters than vacancies. Although early studies suggested that the possible effect of production bias on RIS, we also demonstrated the importance of resolving the spatial dependence [54] [22] [53]. The unbalanced effective production rate of mobile defects, therefore, needs to be interpreted with caution. It is important to bear in mind a different type of irradiation creates different cascade structures and densities. Therefore, the defect production bias depends on the type of irradiation. Neutrons and heavy ions create highly dense cascades, leading to high bias. Despite this, electrons result in isolated point defects, including low bias. Protons and light ions fall between these two limits [3]. Here, the production bias values are aimed to show the general effect on the Cr concentration profiles.

In the Fig. 4.9, when production bias increases, Cr depletion becomes more noticeable in the vicinity of the boundary. Moreover, as shown in Fig. 4.9a, at the high dose rate of 1e-2 dpa/s, Cr concentration at the boundary is drastically reduced, and the depletion layer is widened with 20% production bias. At the dose rate of 1e-4 dpa/s, it is less severe than at the dose rate of 1e-2 dpa/s. However, the width of Cr depletion layer is limited at the low dose rate of 5.6e-6 dpa/s in 500 nm size (see Fig. 4.9c).

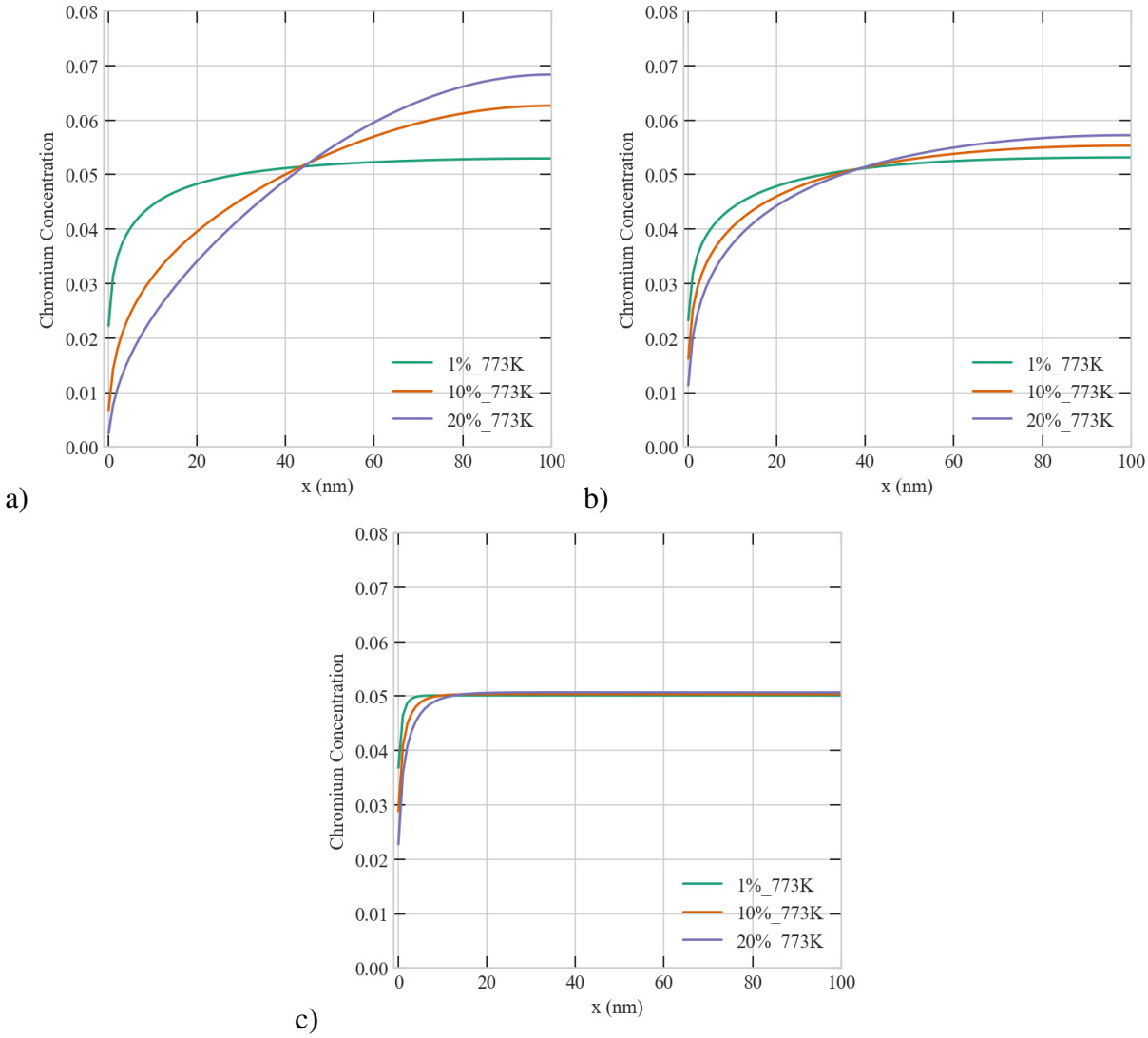

Figure 4.9: Effect of production bias on the steady-state concentration profiles of Chromium in a 100 nm a) Cr concentration at 1e-2 dpa/s b) Cr concentration at 1e-4 dpa/s c) Cr concentration at 5.6e-6 dpa/s

Additionally, at the highest dose rate of 1e-2, the steady-state interstitial concentration with 20% bias is one order of magnitude lower than its corresponding value with 1% bias in 500 nm ((see Fig. 4.12)). However, for the smaller grain size (100 nm), the production bias is less significant on the defect concentrations with 1%, 10%, and 20% biases (see Fig. 4.10).

In Fig. 4.12 for the 500 nm size with 1% production bias, the steady-state vacancy concentration is one order of magnitude higher than its corresponding value with 20% production bias at the

dose rate of 1e-2 dpa/s.

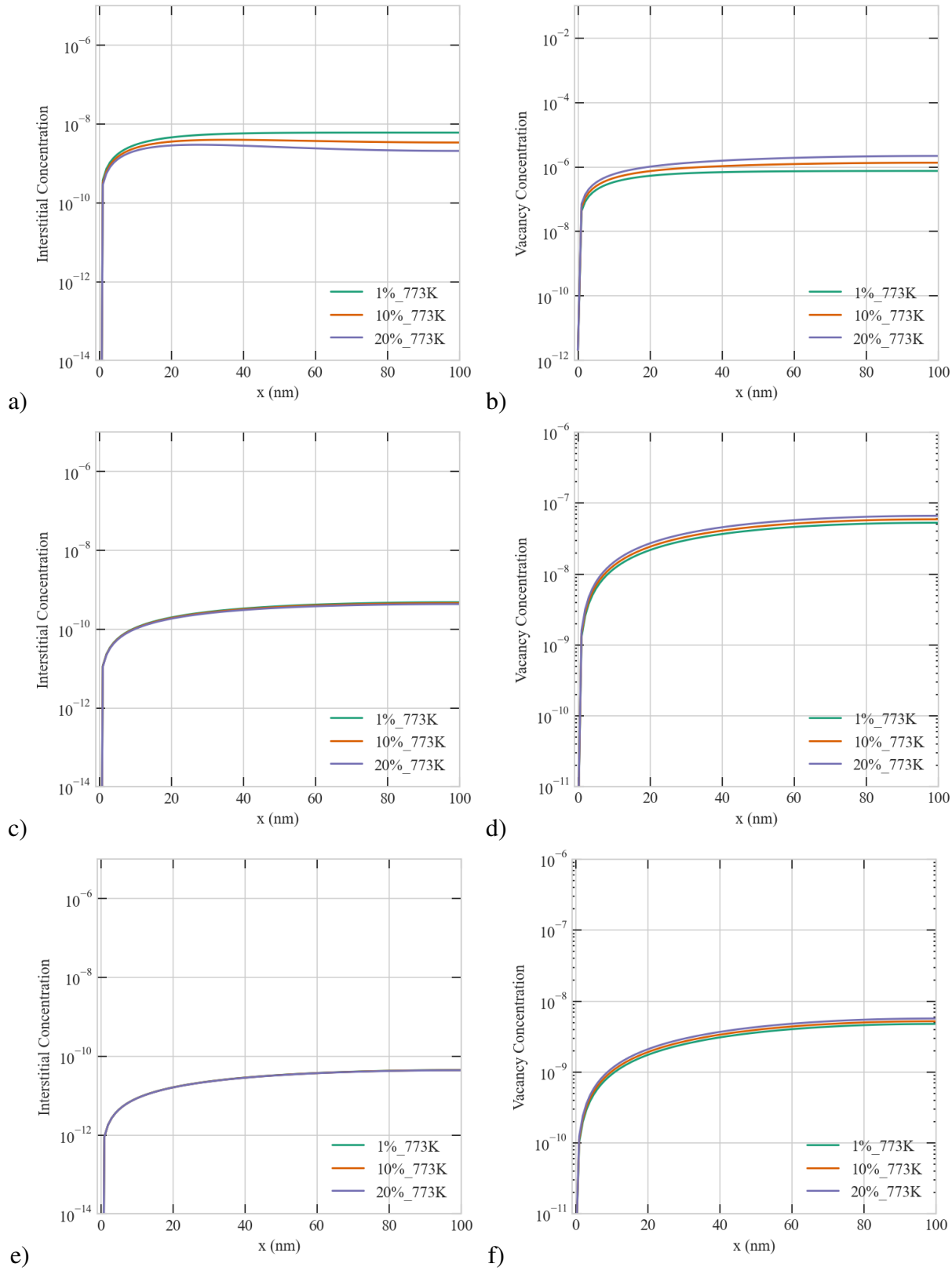

Figure 4.10: Effect of production bias on the steady-state concentration profiles of point defects in a 100 nm. Upper row: a) interstitial b) vacancy concentrations at 1e-2 dpa/s. Middle row: c) interstitial d) vacancy concentrations at 1e-4 dpa/s. Lower row: e) interstitial f) vacancy concentrations at 5.6e-6 dpa/s

With the increase in production bias, Cr depletion increases, and the Cr depletion layer is widened. Furthermore, we noticed that at the same dose rate, temperature, and size, depletion of Cr with 20% bias is higher than depletion of Cr with 1% bias. This could be attributed to the bias factor since Cr exchange preferably with vacancies. Additionally, at the same dose rate, temperature, and production bias, depletion of Cr in 500 nm is higher than depletion of Cr in 100 nm. Together these studies provide important insights into the effect of production bias on RIS. Here, we demonstrated that production bias modify the resulting distribution of Cr concentration and its effect is more apparent in the larger grains (size>100 nm).

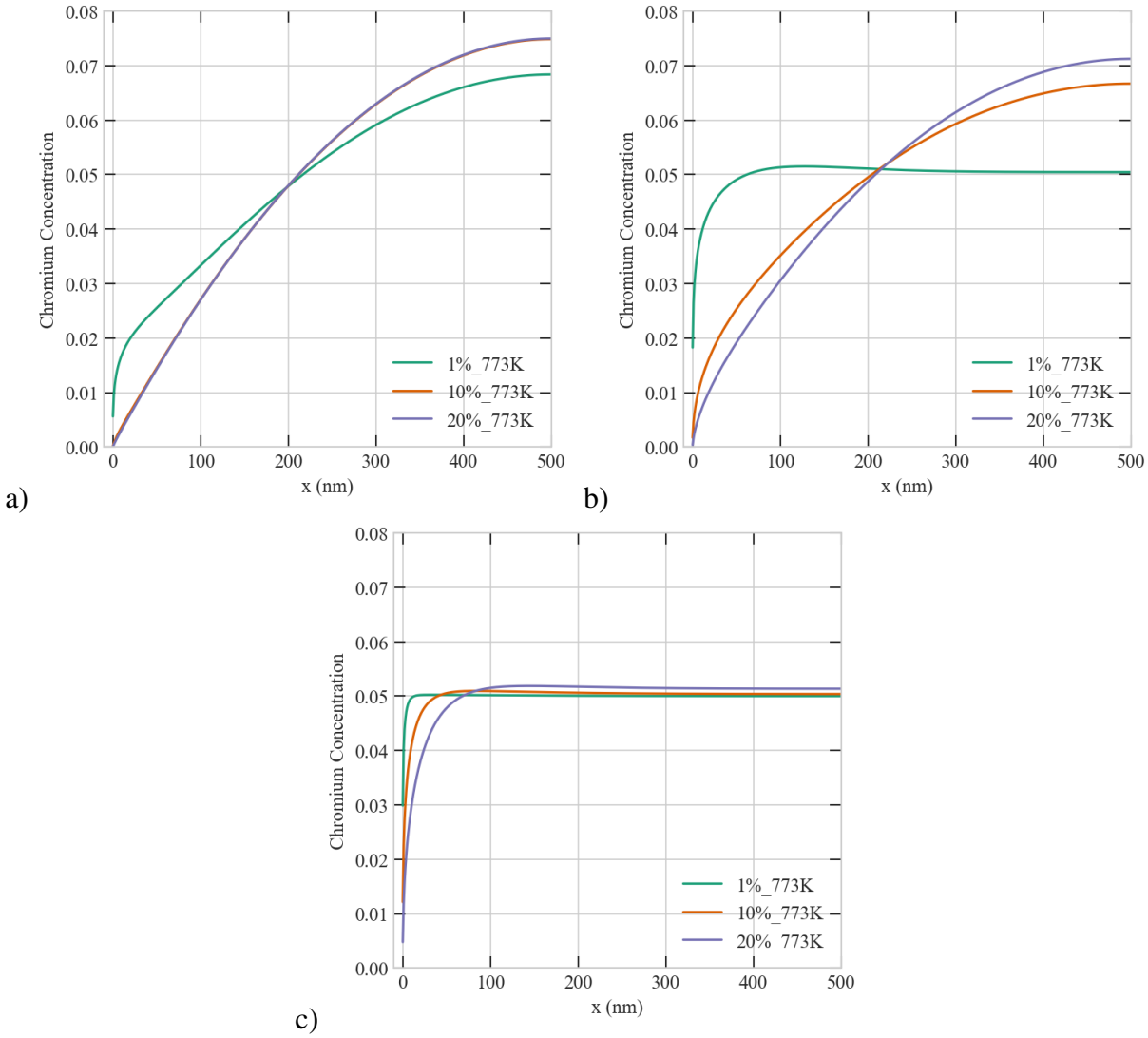

Figure 4.11: Effect of production bias on the steady-state concentration profiles of Chromium in a 500 nm a) Cr concentration at 1e-2 dpa/s b) Cr concentration at 1e-4 dpa/s c) Cr concentration at 5.6e-6 dpa/s

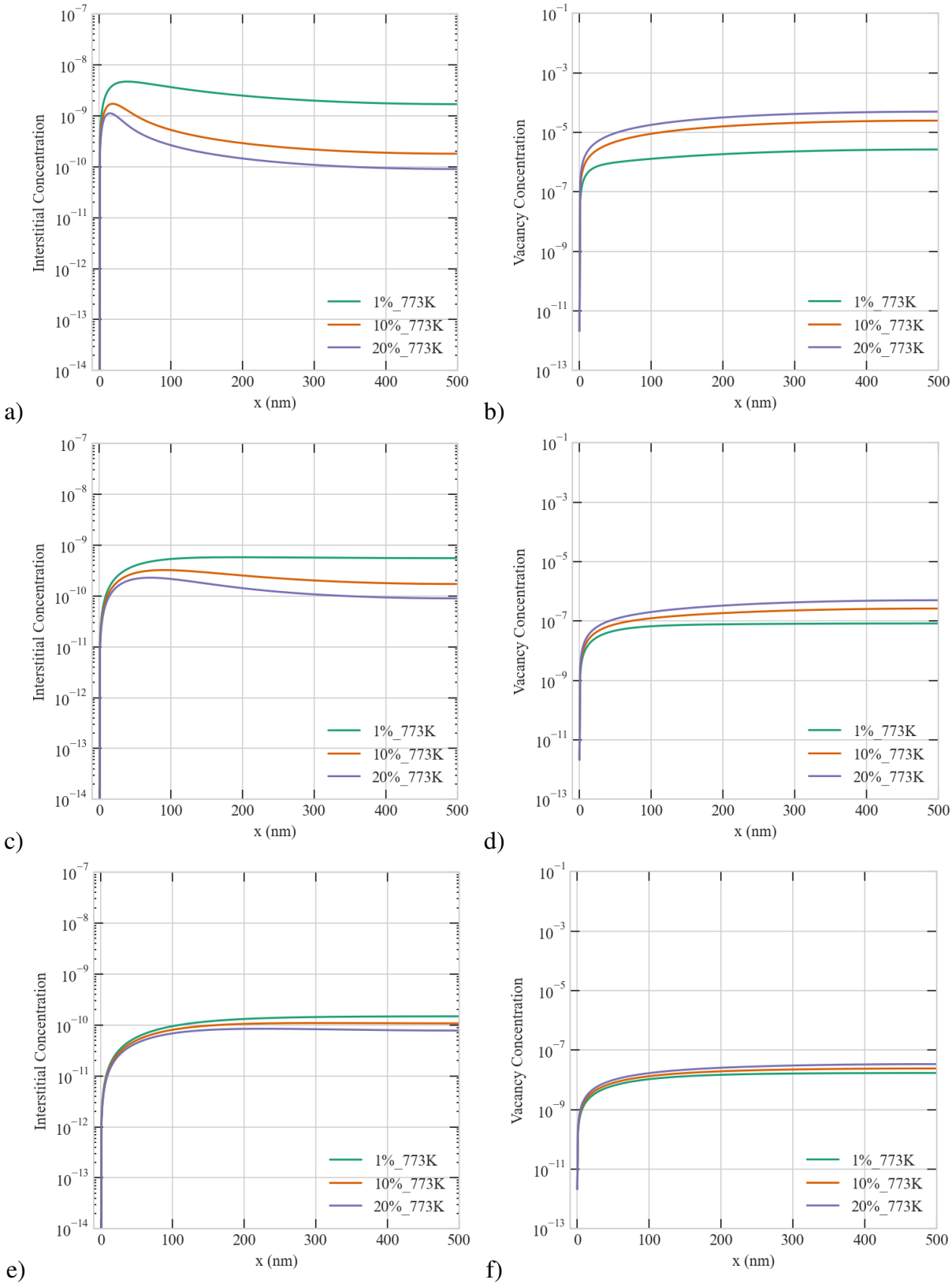

Figure 4.12: Effect of production bias on the steady-state concentration profiles of point defects in a 500 nm. Upper row: a) interstitial b) vacancy concentrations at 1e-2 dpa/s. Middle row: c) interstitial d) vacancy concentrations at 1e-4 dpa/s. Lower row: e) interstitial f) vacancy concentrations at 5.6e-6 dpa/s

4.4 Effect of Temperature

First, we investigated effect of temperature on RIS. Ni-5Cr alloys were simulated to determine the importance of the shift in temperature and dose rate. We analyzed the evaluated results at three different temperatures, 437 K, 573 K, and 773 K. In this section, we assumed sinks are present in the bulk uniformly distributed with a concentration of 1e18 m^{-3}. Effect of sink density will be examined in greater detail later in this work.

It is also important to note that the rate of defect recombination influences radiation-induced segregation because defects that survive from recombination determine the degree of atom segregation. Thus, we can say that if recombination dominates, segregation becomes less severe. Since recombination rate is altered by temperature and defect concentration, it is essential to understand the temperature effect on concentration profile. Thus, we employed three different dose rates (1e-2, 1e-4, and 5.6e-6 dpa/s) to examine the effect of the dose rate with the temperature on the concentration profile.

Fig. 4.13 shows effect of temperature on the steady-state concentration profiles of Chromium. While the highest Cr depletion is observed at 473 K, the lowest is observed at 773 K for three dose rates. When temperature increases from 473 K to 773 K, the steady-state concentration of vacancies decreases, while the interstitial concentration increases. Therefore, the difference between the vacancy and interstitial concentrations is reduced at 773 K. As a result of this, the Cr depletion at the grain boundary has become less severe. Our model prediction matches this trend reasonably well at 773 K.

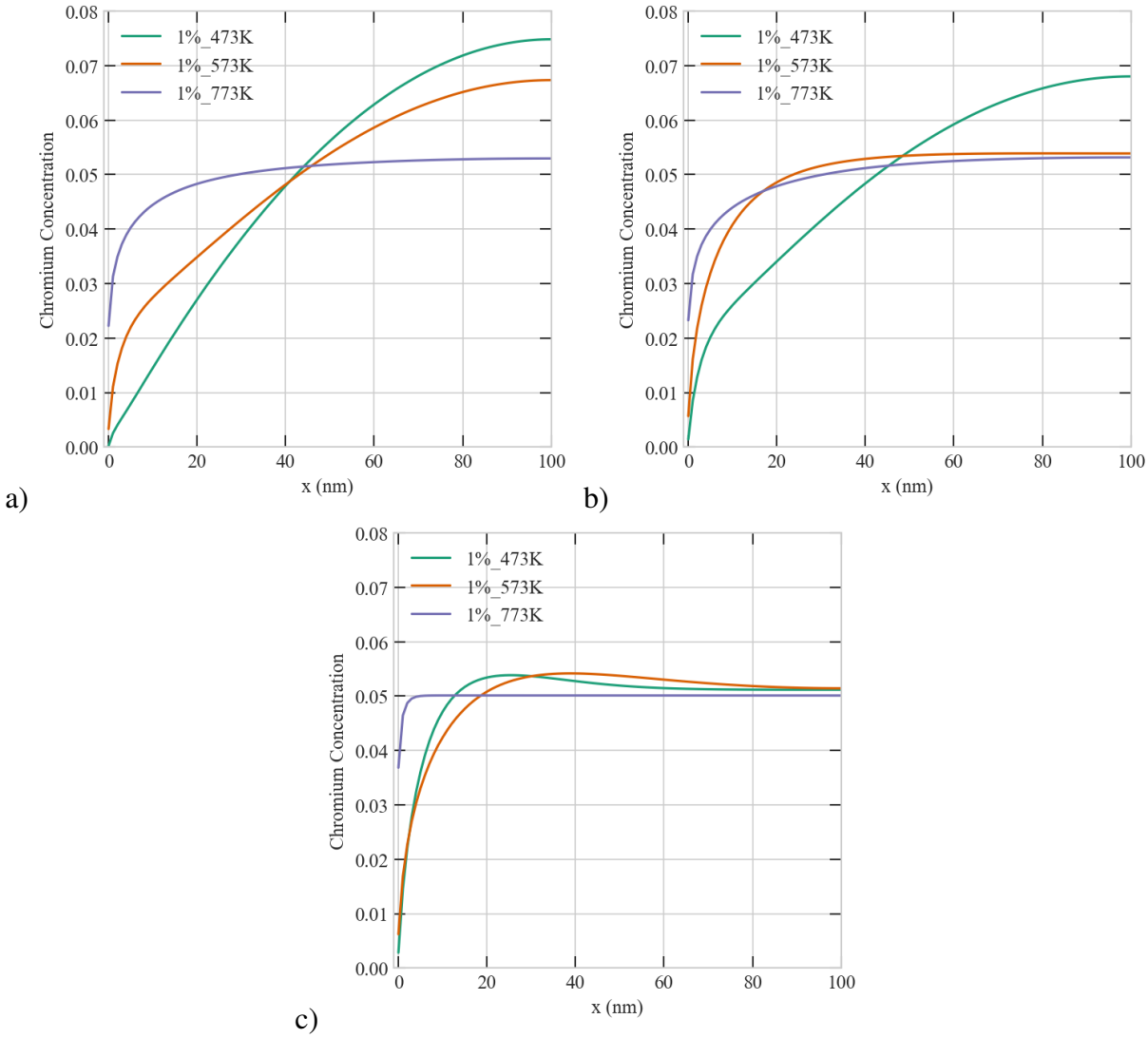

Figure 4.13: Effect of temperature on the steady-state concentration profiles of Chromium a) Cr concentration at 1e-2 dpa/s b) Cr concentration at 1e-4 dpa/s c) Cr concentration at 5.6e-6 dpa/s

At the dose rate of 5.6e-6 dpa/s, we observed that steady-state interstitial concentration at 573 K is higher than other temperatures (see Fig. 4.14), and this might have caused the Cr depletion layer is widened. Together these results provide importance of interstitials at the lower temperatures, and it could be attributed to the uncertainties associated with interstitial diffusivities at low temperatures [55].

Overall, the results of the various simulations indicate that the irradiation temperature has a

distinct effect on depletion of Cr as in experimental studies [18][56][53].

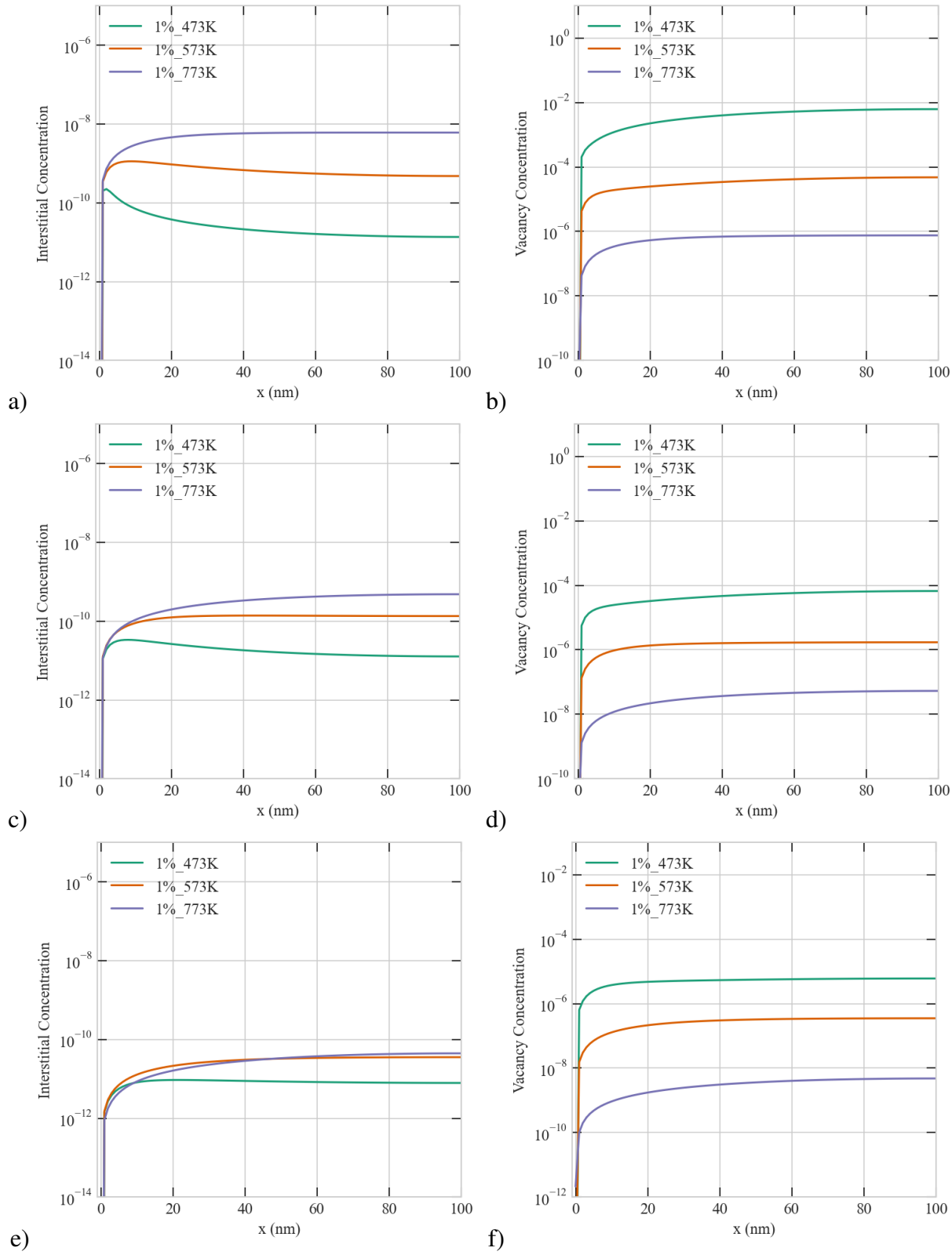

Figure 4.14: Effect of temperature on the steady-state concentration profiles of point defects in a 100 nm. Upper row: a) interstitial b) vacancy concentrations at 1e-2 dpa/s. Middle row: c) interstitial d) vacancy concentrations at 1e-4 dpa/s. Lower row: e) interstitial f) vacancy concentrations at 5.6e-6 dpa/s

4.5 The Combined Effects of Microstructure and Irradiation Parameters

In this section, we extended our work by combining the parameters we mentioned in previous sections. We will discuss the effect of sink density, grain size, temperature, production bias, and dose rate in detail.

Consideration of inner sinks such as dislocation loops and voids allows better agreement with experimental measurements. This agreement may be explained by the fact that irradiation temperature could change the internal sink strength [57]. Previous studies have reported that sink density can be significantly influenced by the temperature increase from 673 K to 773 K. Moreover, irradiations at 673 K seem to result in a high sink density than irradiations at 773 K in Ni-Cr alloys. Conversely, higher temperature irradiations produced a low void density [19, 58]. These experimental observations suggest that an increment in point defect recombination and annihilation due to enhanced mobility at 773 K coupled with prolonged thermal emission diminishes sink density. Additionally, another study showed that by increasing the proton irradiation temperature from 673 K to 773 K, a decrease in density was seen for dislocation and voids. Moreover, heavy-ion irradiated Ni-Cr alloys displayed high void density than the proton-irradiated Ni-Cr alloys [2]. This indicates a need to understand the effect of sink density in order to emulate better neutron irradiation damage. Therefore, we performed simulations at three different temperatures, 473 K, 573 K, and 773 K with uniformly distributed bulk sinks with a concentration of 1e18, 1e20, and 1e22 m^{-3}. We have conducted simulations for 5 different grain sizes (100, 300, 500, 5000 and 7500 nm) and three different dose rates (1e-2 ,1e-4 and 5.6e-6 dpa/s).

4.5.1 The Combined Effects of Microstructure and Irradiation Parameters at 773K

In Fig.4.15, with the increase of bias, there is a noticeable change on Cr concentration profile. Low sink density (1e18 m^{-3}) leads to more Cr depletion at the boundary, but this effect is limited to the zone close to the boundary. The experimental results shows that high sink density reduces more vacancy, absorbing the vacancies. Moreover, sinks contribute to interstitial annihilation, depending on the temperature [59]. However, for 100 nm size, effect of the sink density 1e18 and 1e22 m^{-3}

on interstitial and vacancy concentrations is not apparent at all dose rates (see Fig.4.16, Fig.4.18 and Fig. 4.20). In addition, increasing the bias does not significantly affect vacancy concentration at the dose rate of 5.6e-6 dpa/s. Although the vacancy concentration increases with the dose rate, effect of the production bias and sink density is inadequate in 100 nm.

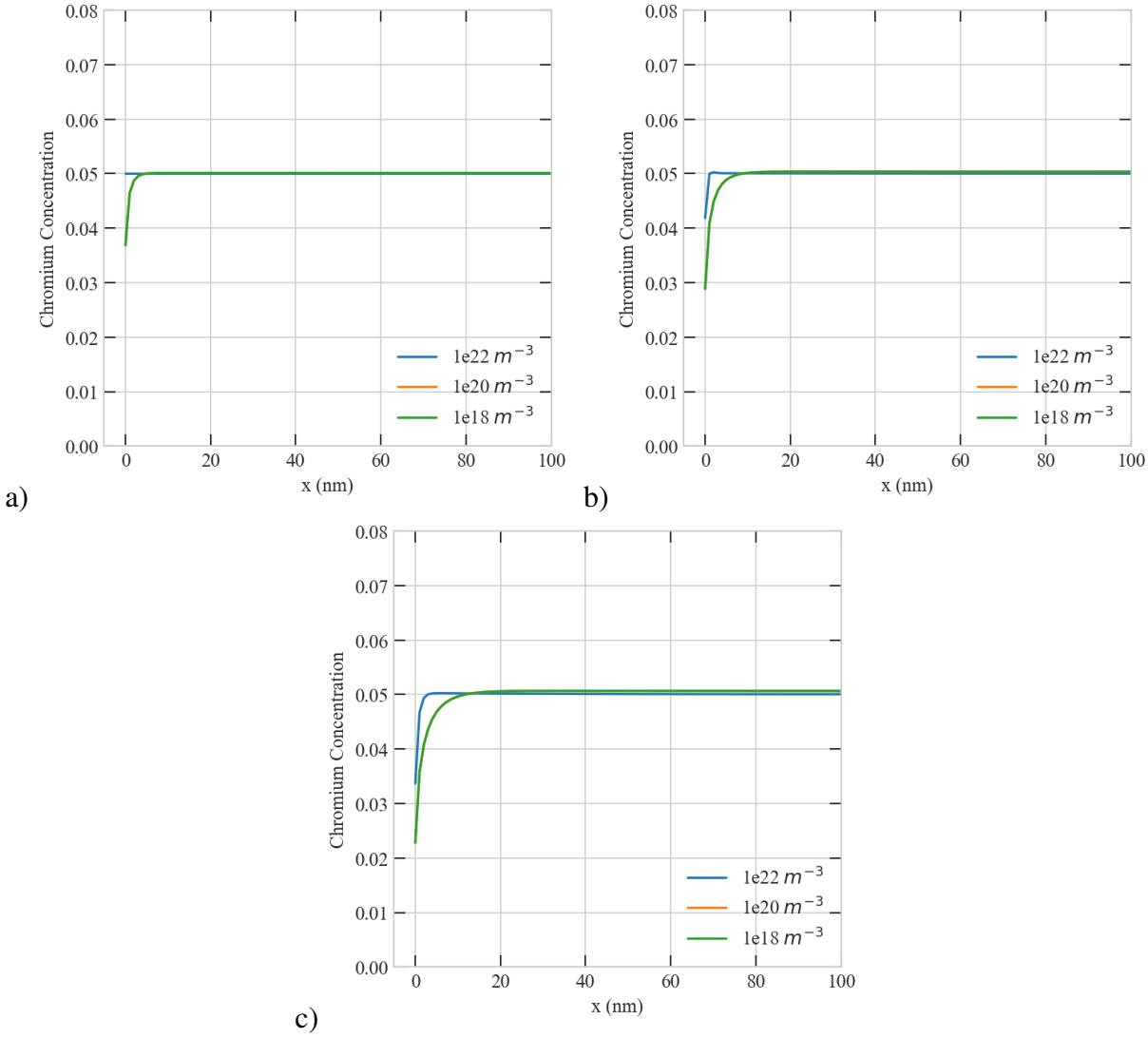

Figure 4.15: Effect of sink density on the steady-state concentration profiles of Chromium in 100 nm at 5.6e-6 dpa/s a) 1% bias, Cr concentration b) 10% bias, Cr concentration c) 20% bias, Cr concentration.

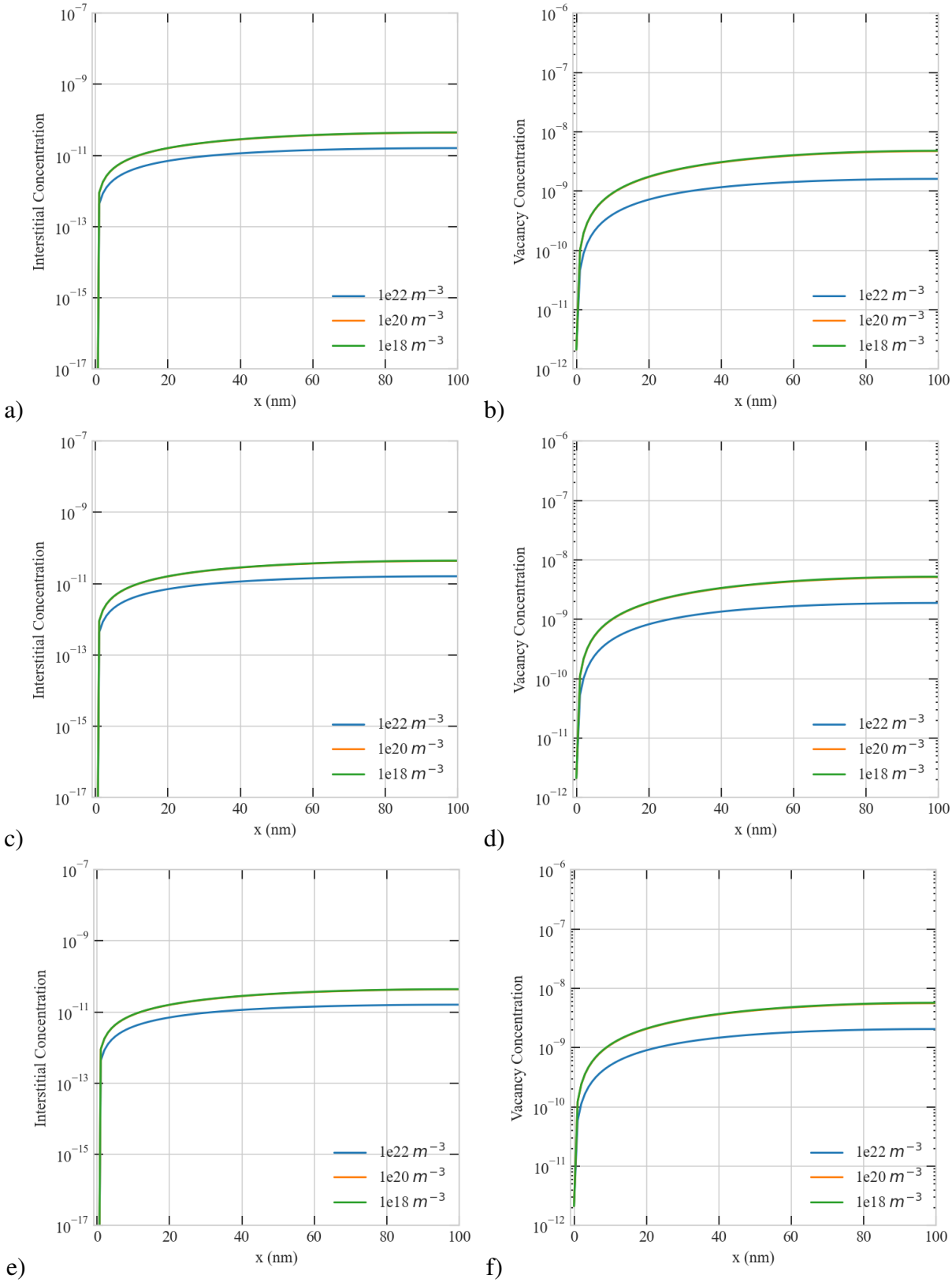

Figure 4.16: Effect of sink density on the steady-state concentration profiles of point defects in a 100 nm at 5.6e-6 dpa/s a) 1% bias, interstitial b) 1% bias, vacancy c) 10% bias, interstitial d) 10% bias, vacancy e) 20% bias, interstitial and f) 20% bias, vacancy concentrations.

At the dose rate of 1e-4 dpa/s, the increase in Cr depletion in the vicinity of the boundary becomes more pronounced with increasing the dose rate. The depletion in Cr is higher for 1e18 m^{-3} sink density, and changing the sink density does not have a significant effect on the width of the Cr depletion layer (see Fig. 4.17). In Fig. 4.18, interstitial and vacancy concentrations show no strong dependence on production bias in 100 nm.

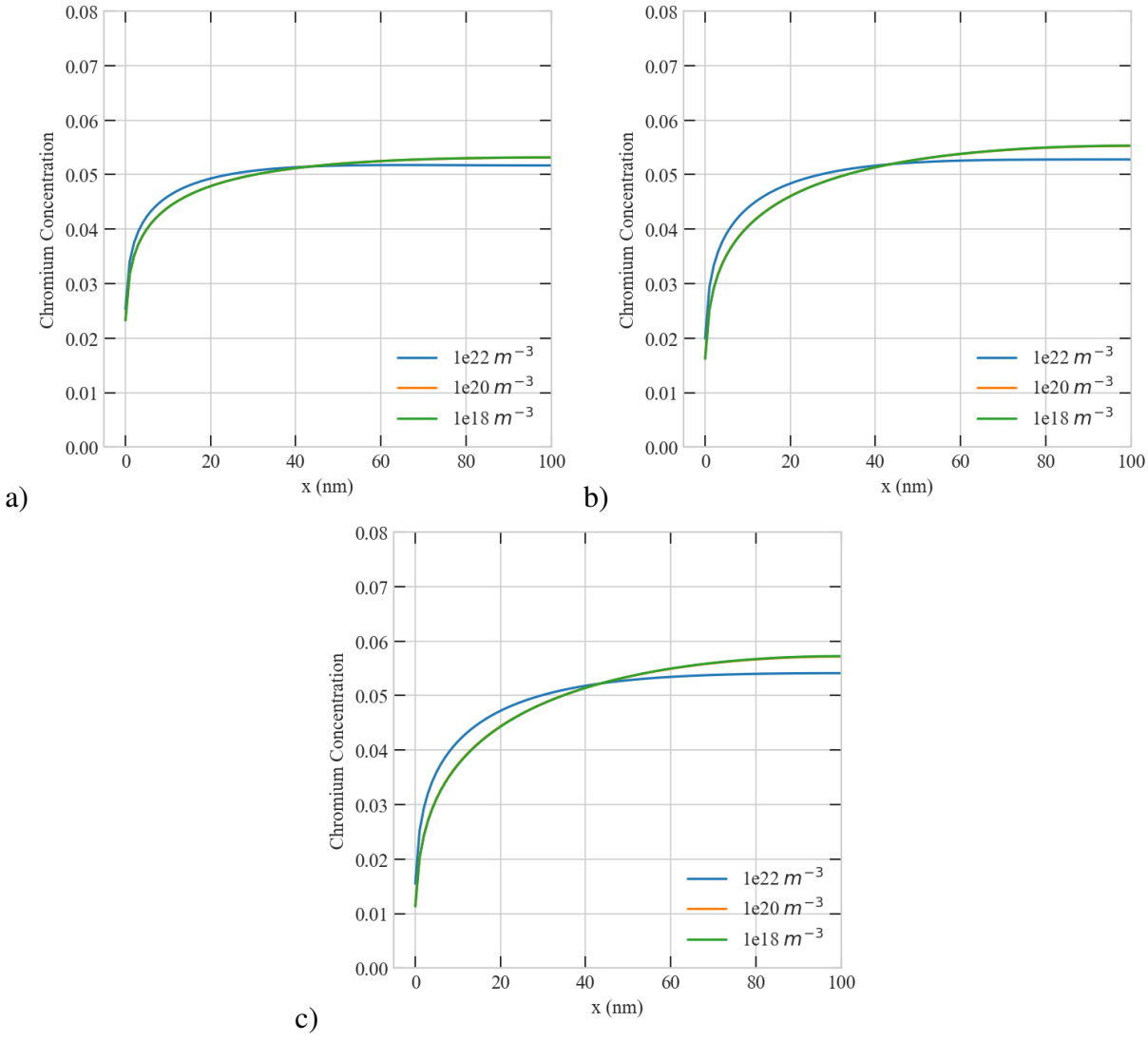

Figure 4.17: Effect of sink density on the steady-state concentration profiles of Chromium in 100 nm at 1e-4 dpa/s a) 1% bias, Cr concentration b) 10% bias, Cr concentration c) 20% bias, Cr concentration.

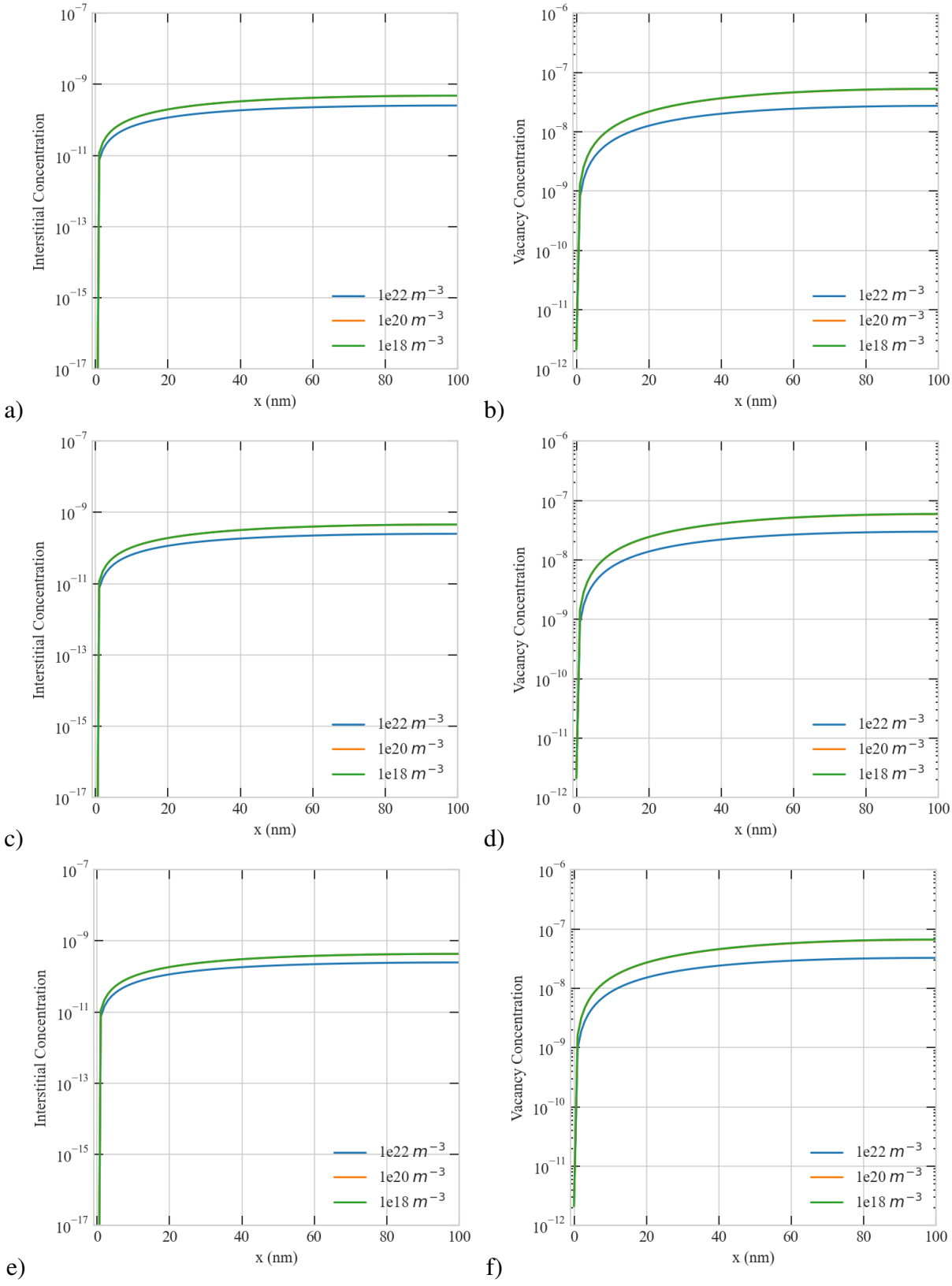

Figure 4.18: Effect of sink density on the steady-state concentration profiles of point defects in a 100 nm at 1e-4 dpa/s a) 1% bias, interstitial b) 1% bias, vacancy c) %10 bias, interstitial d) 10% bias, vacancy e) 20% bias, interstitial and f) 20% bias, vacancy concentrations.

At the dose rate of 1e-2 dpa/s, changing the sink density have a visible effect on the width of the Cr depletion layer. Width of the Cr depletion layer increases with production bias. Also, vacancy and interstitial concentrations for three sink densities follow similar trend at the high dose rate (1e-2 dpa/s) with 1% bias in 100 nm.

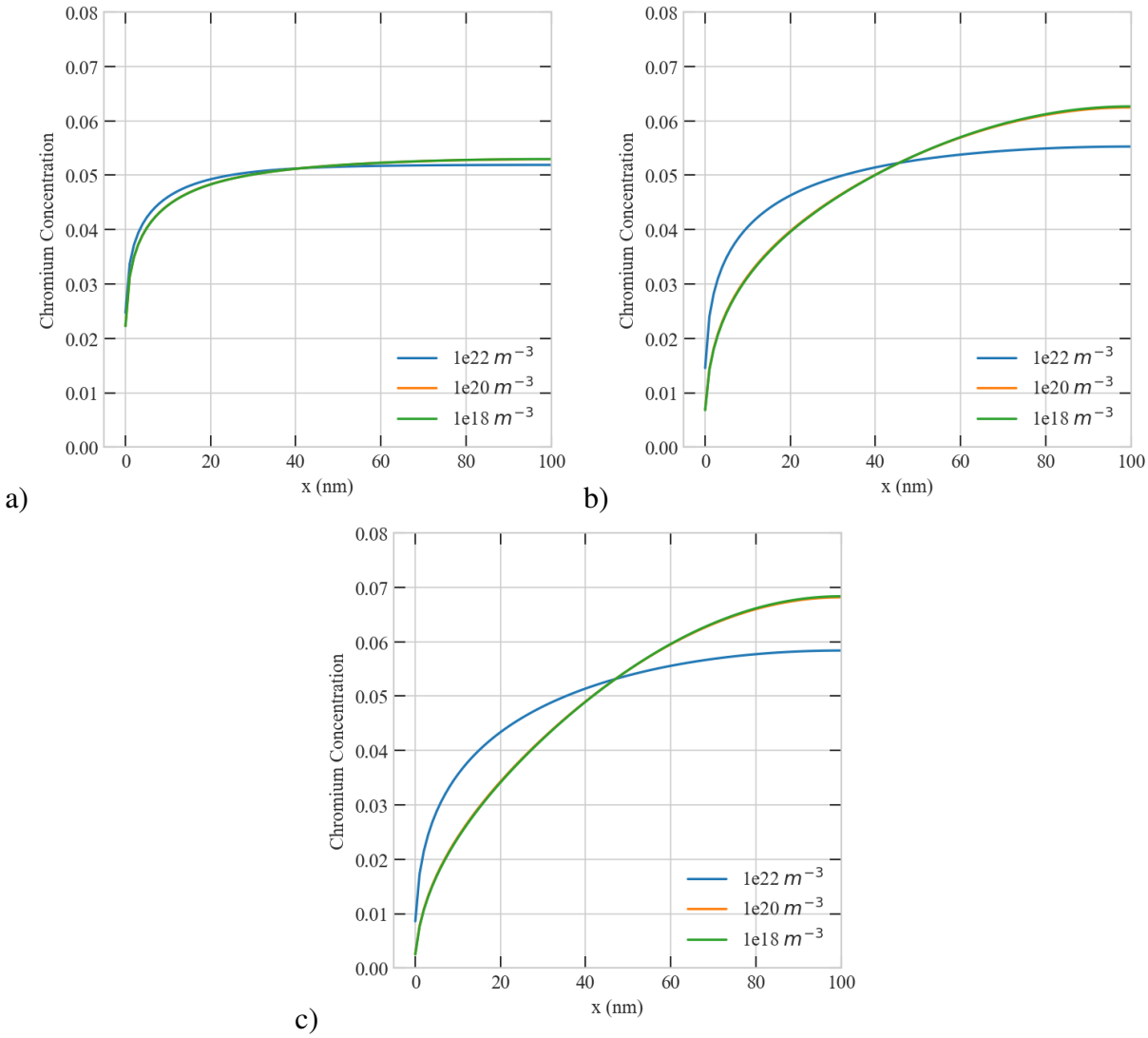

Figure 4.19: Effect of sink density on the steady-state concentration profiles of Chromium in 100 nm at 1e-2 dpa/s a) 1% bias, Cr concentration b) 10% bias, Cr concentration c) 20% bias, Cr concentration.

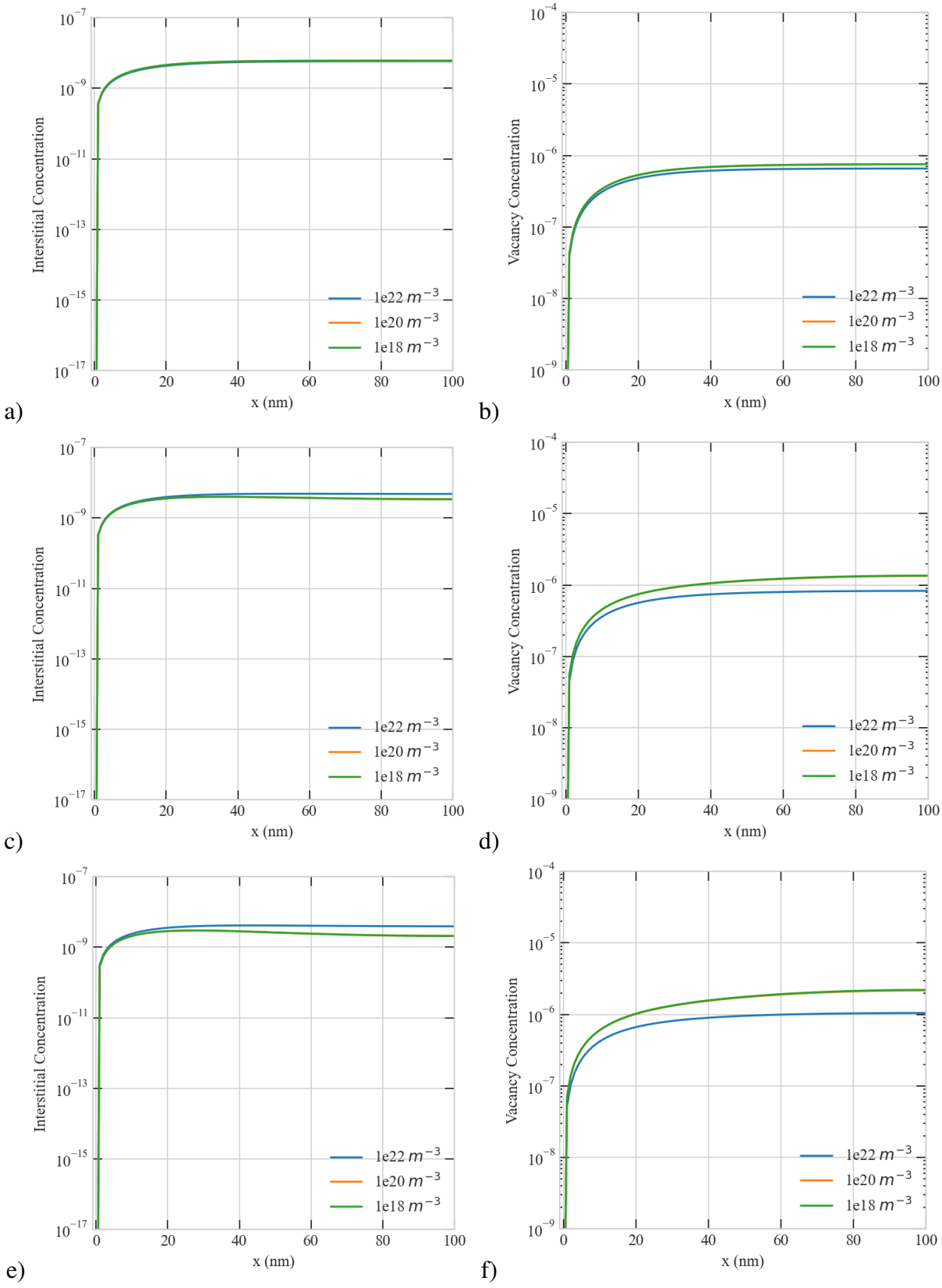

Figure 4.20: Effect of sink density on the steady-state concentration profiles of point defects in a 100 nm at 1e-2 dpa/s a) 1% bias, interstitial b) 1% bias, vacancy c) 10% bias, interstitial d) 10% bias, vacancy e) 20% bias, interstitial and f) 20% bias, vacancy concentrations.

For 300 nm size, the difference between 1e18 and 1e20 m^{-3} sink density becomes more pronounced on interstitial and vacancy concentration even at the low dose rate (5.6e-6 dpa/s). As can be seen from the Fig. 4.21, this effect is also reflected on the Cr depletion profile. Furthermore, with the bias effect, the increase in vacancy concentration becomes more evident. While the behavior of the interstitial concentration at the dose rate of 5.6e-6 and 1e-4 dpa/s follows similar trend (see Fig. 4.24), this trend begins to differ at the dose rate of 1e-2 dpa/s.

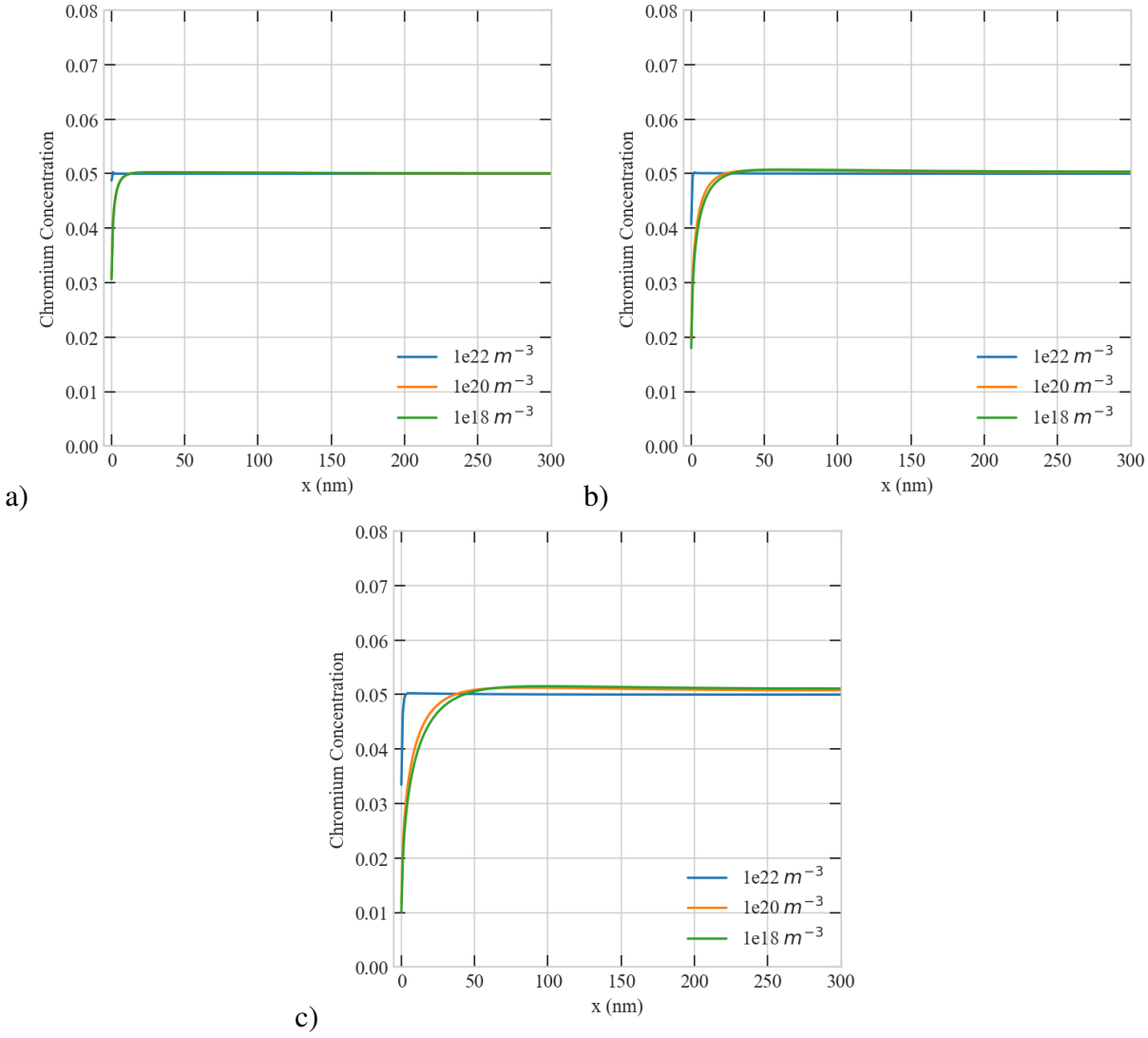

Figure 4.21: Effect of sink density on the steady-state concentration profiles of Chromium in 300 nm at 5.6e-6 dpa/s a) 1% bias, Cr concentration b) 10% bias, Cr concentration c) 20% bias, Cr concentration.

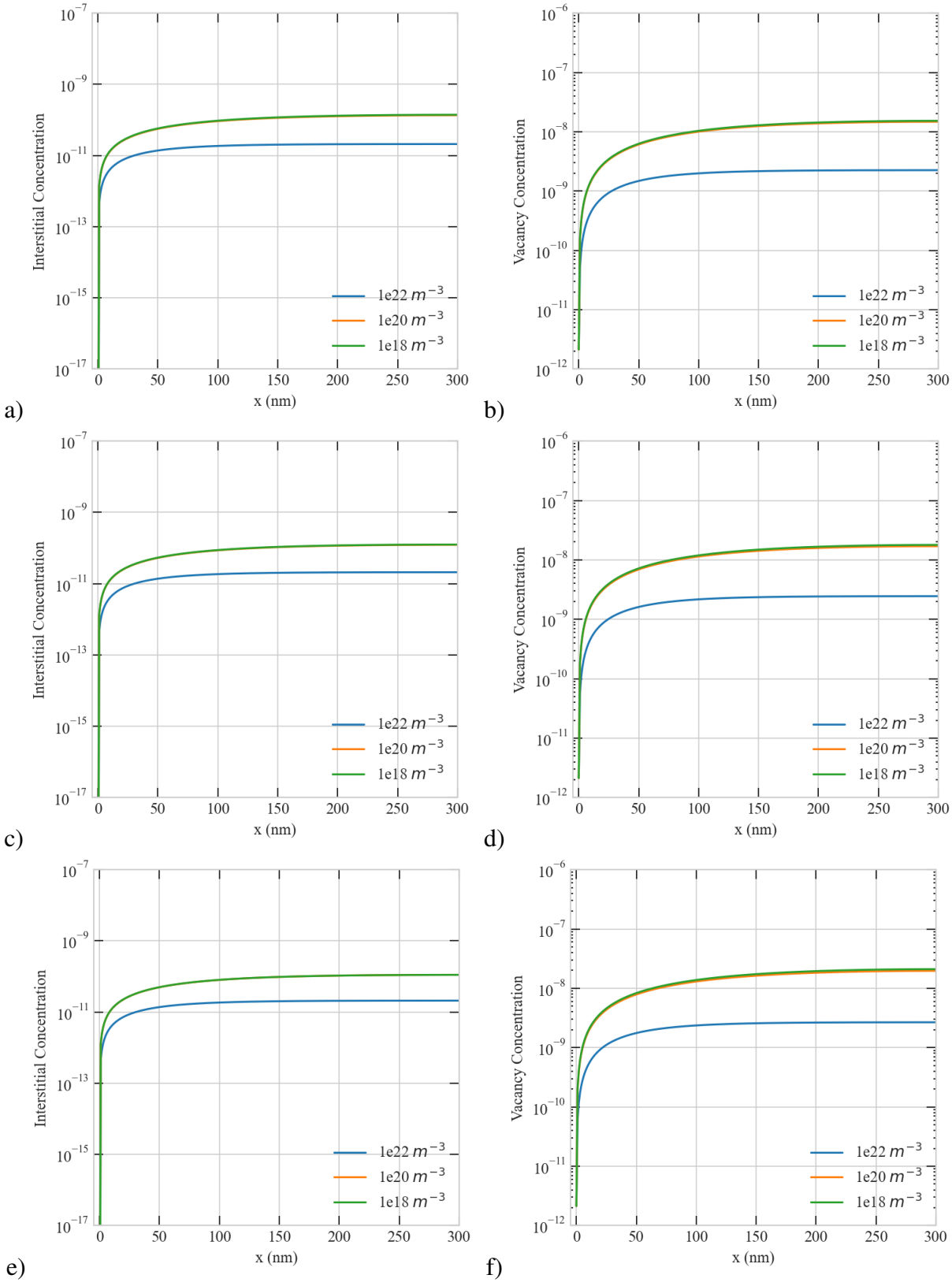

Figure 4.22: Effect of sink density on the steady-state concentration profiles of point defects in a 300 nm at 5.6e-6 dpa/s a) 1% bias, interstitial b) 1% bias, vacancy c) 10% bias, interstitial d) 10% bias, vacancy e) 20% bias, interstitial and f) 20% bias, vacancy concentrations.

Fig. 4.26 depicts that interstitial and vacancy concentration begins to show opposite trends. It causes an instability, and hence it becomes more noticeable with 10% and 20% biases. Vacancies tend to accumulate in the center of the domain and interstitials tend to accumulate by the boundary. The beginning of this instability is attributed to the fact that production bias breaks the balance of point defects, leading to non-uniform bulk recombination and non-uniform losses to the boundary.

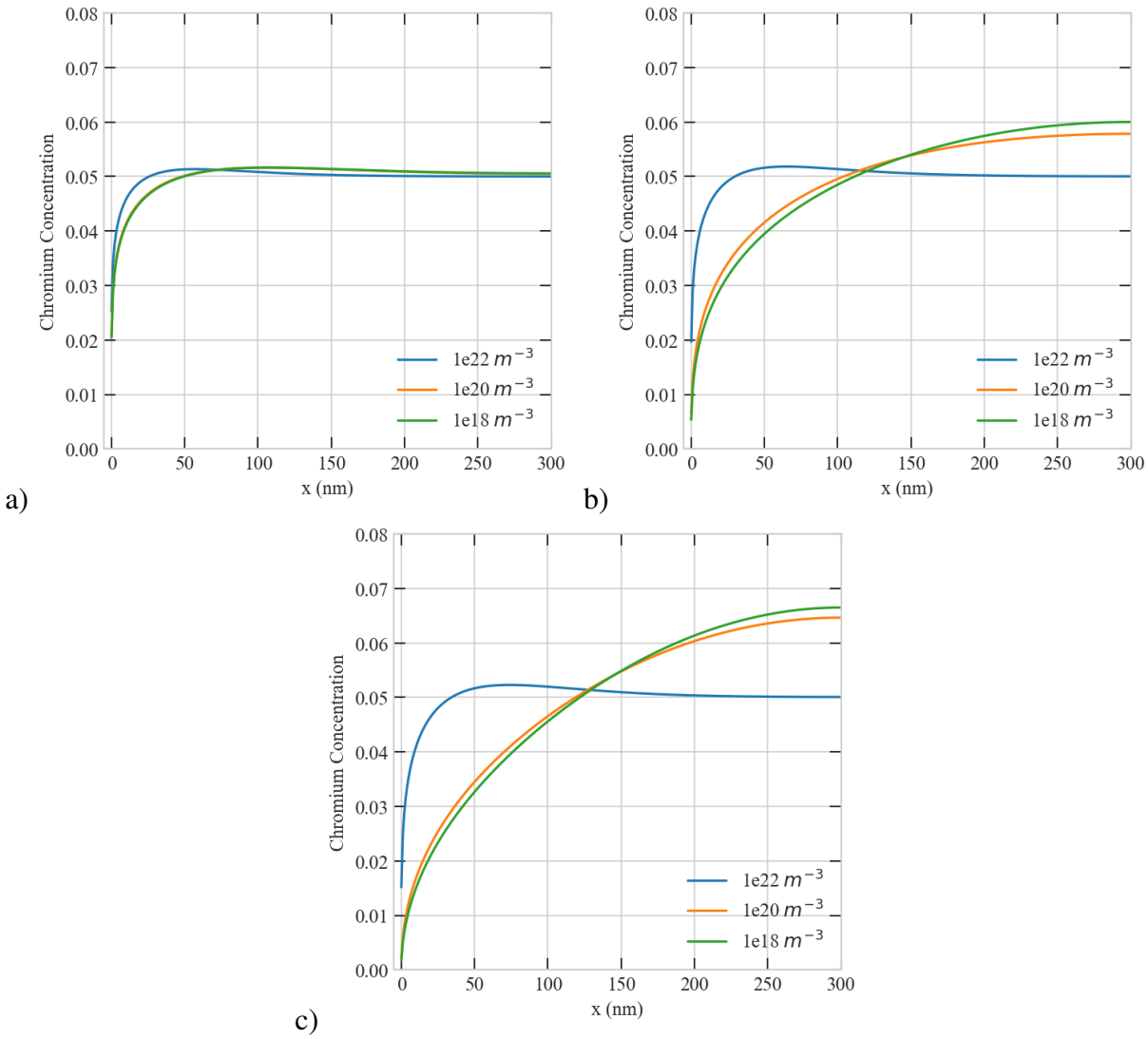

Figure 4.23: Effect of sink density on the steady-state concentration profiles of Chromium in 300 nm at 1e-4 dpa/s a) 1% bias, Cr concentration b) 10% bias, Cr concentration c) 20% bias, Cr concentration.

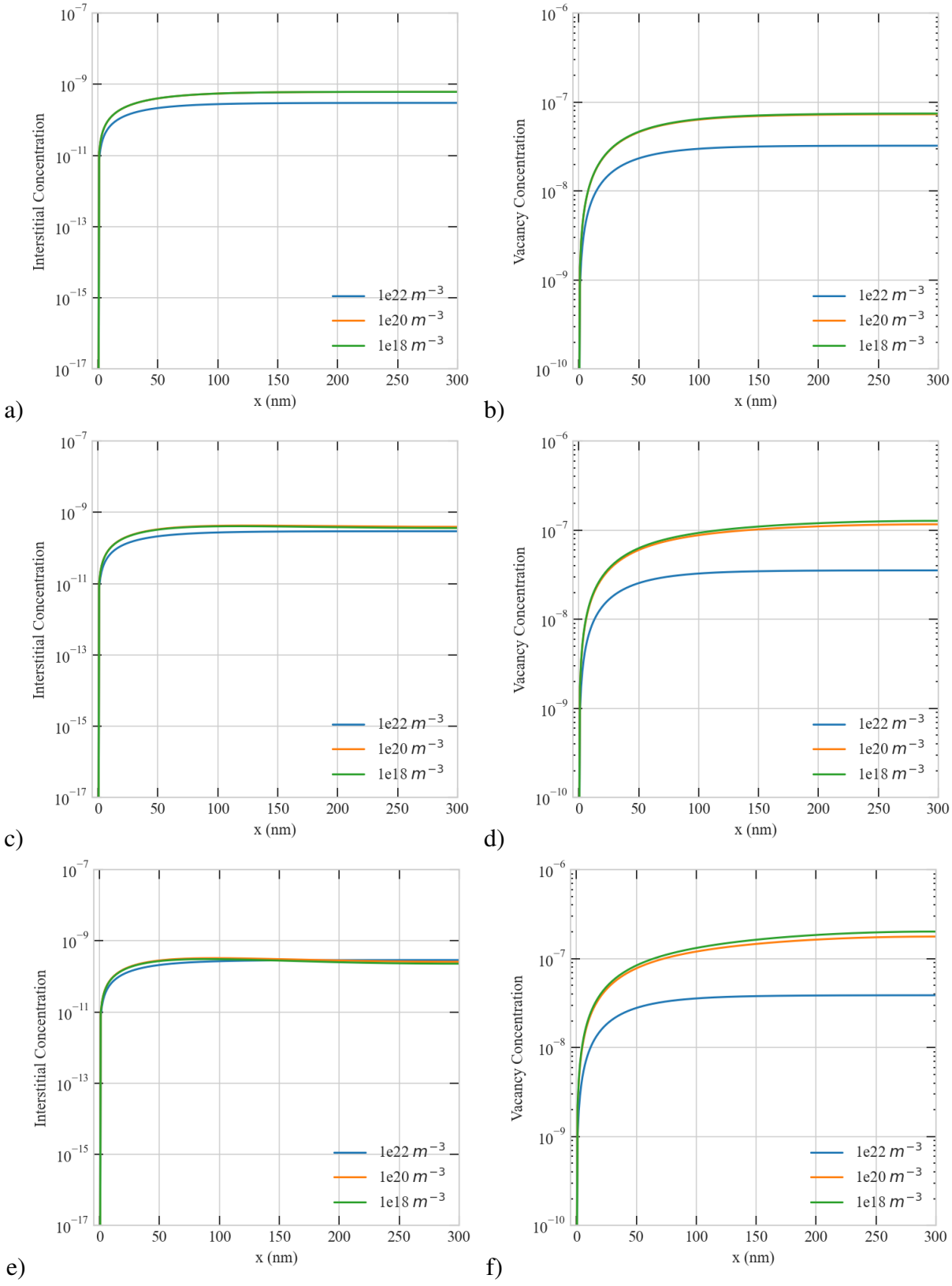

Figure 4.24: Effect of sink density on the steady-state concentration profiles of point defects in a 300 nm at 1e-4 dpa/s a) 1% bias, interstitial b) 1% bias, vacancy c) 10% bias, interstitial d) 10% bias, vacancy e) 20% bias, interstitial and f) 20% bias, vacancy concentrations.

Instability was observable for 1e18 and 1e20 m^{-3} sink densities, but not for 1e22 m^{-3} in 300 nm (see Fig. 4.26). A possible explanation for these results is that interstitial annihilation at sinks dominates first and is followed by recombination and later vacancy loss to sinks at the high sink density (1e22 m^{-3}).

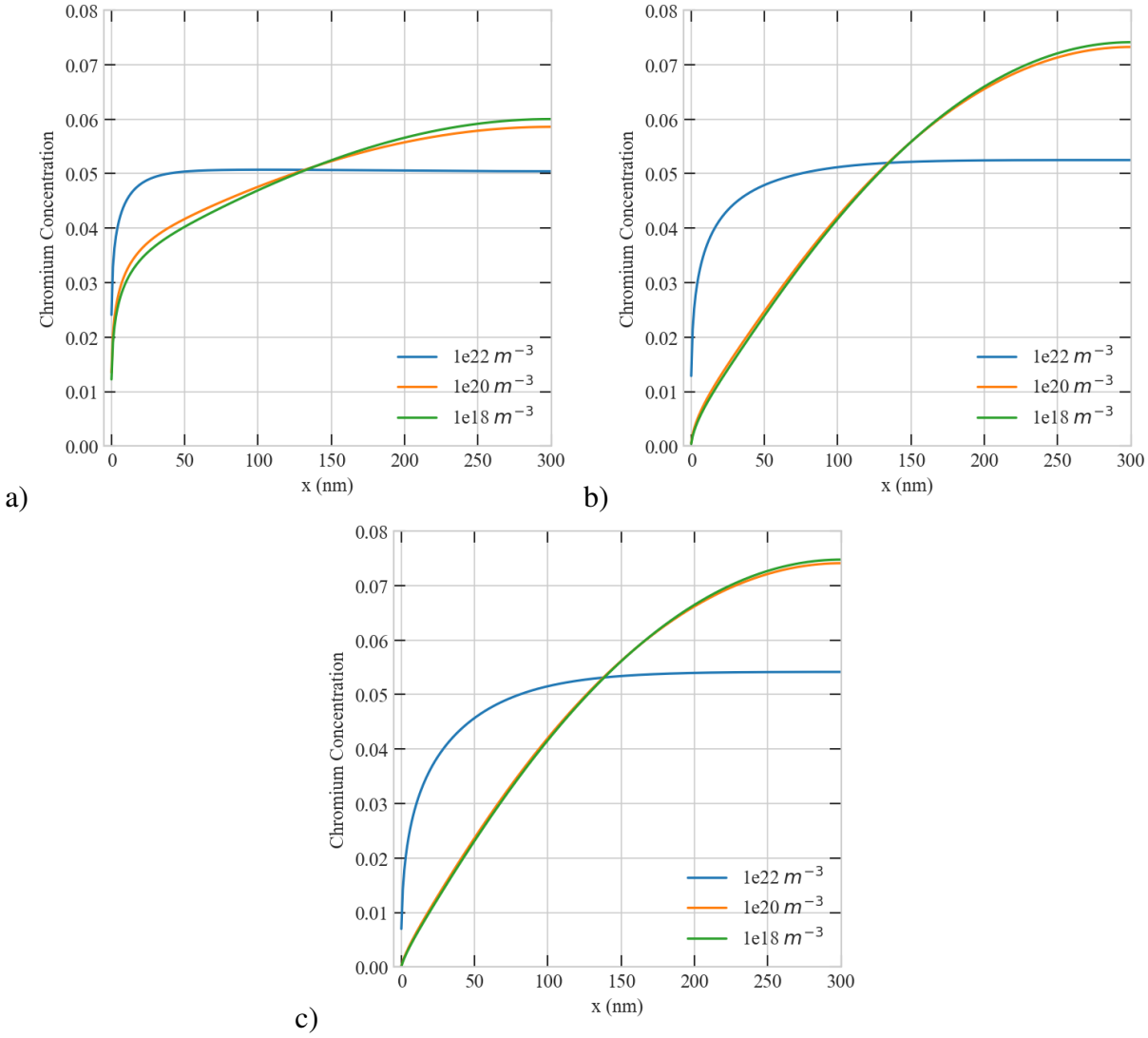

Figure 4.25: Effect of sink density on the steady-state concentration profiles of Chromium in 300 nm at 1e-2 dpa/s a) 1% bias, Cr concentration b) 10% bias, Cr concentration c) 20% bias, Cr concentration.

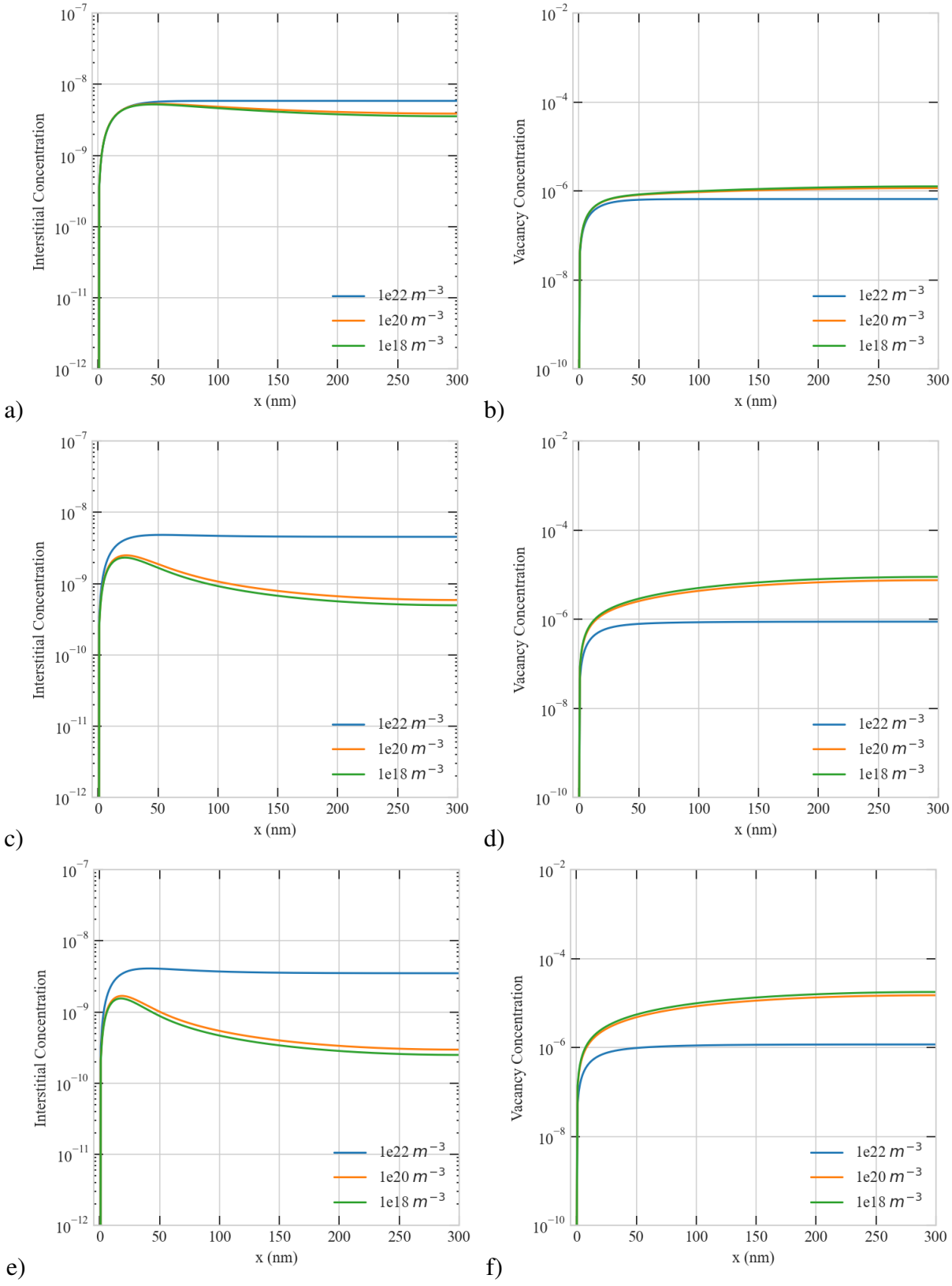

Figure 4.26: Effect of sink density on the steady-state concentration profiles of point defects in a 300 nm at 1e-2 dpa/s a) 1% bias, interstitial b) 1% bias, vacancy c) 10% bias, interstitial d) 10% bias, vacancy e) 20% bias, interstitial and f) 20% bias, vacancy concentrations.

For 1e18 and 1e20 m^{-3} sink densities, the effect of sink density on interstitial and vacancy concentrations at the low dose rate is not clearly apparent in 500 nm . Fig. 4.28 shows changing the sink density from 1e18 to 1e20 m^{-3} had no clear impact on interstitial and vacancy concentration. However, the effect of the difference between 1e18 and 1e20 m^{-3} becomes more pronounced with an increase in production bias. Besides, the increase in difference for sink densities has made its effect on Cr depletion more pronounced with bias as seen in Fig. 4.27.

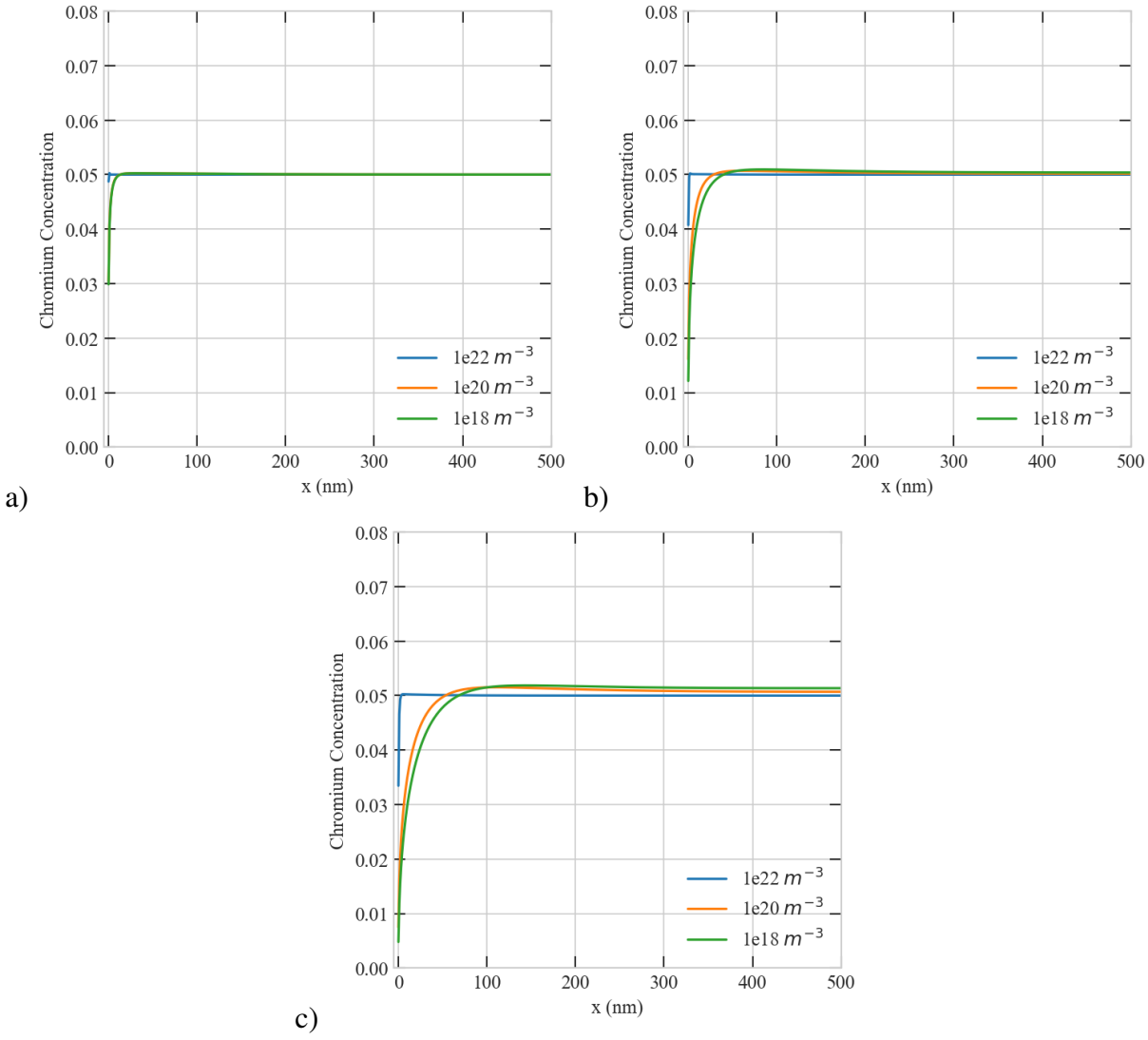

Figure 4.27: Effect of sink density on the steady-state concentration profiles of Chromium in 500 nm at 5.6e-6 dpa/s a) 1% bias, Cr concentration b) 10% bias, Cr concentration c) 20% bias, Cr concentration.

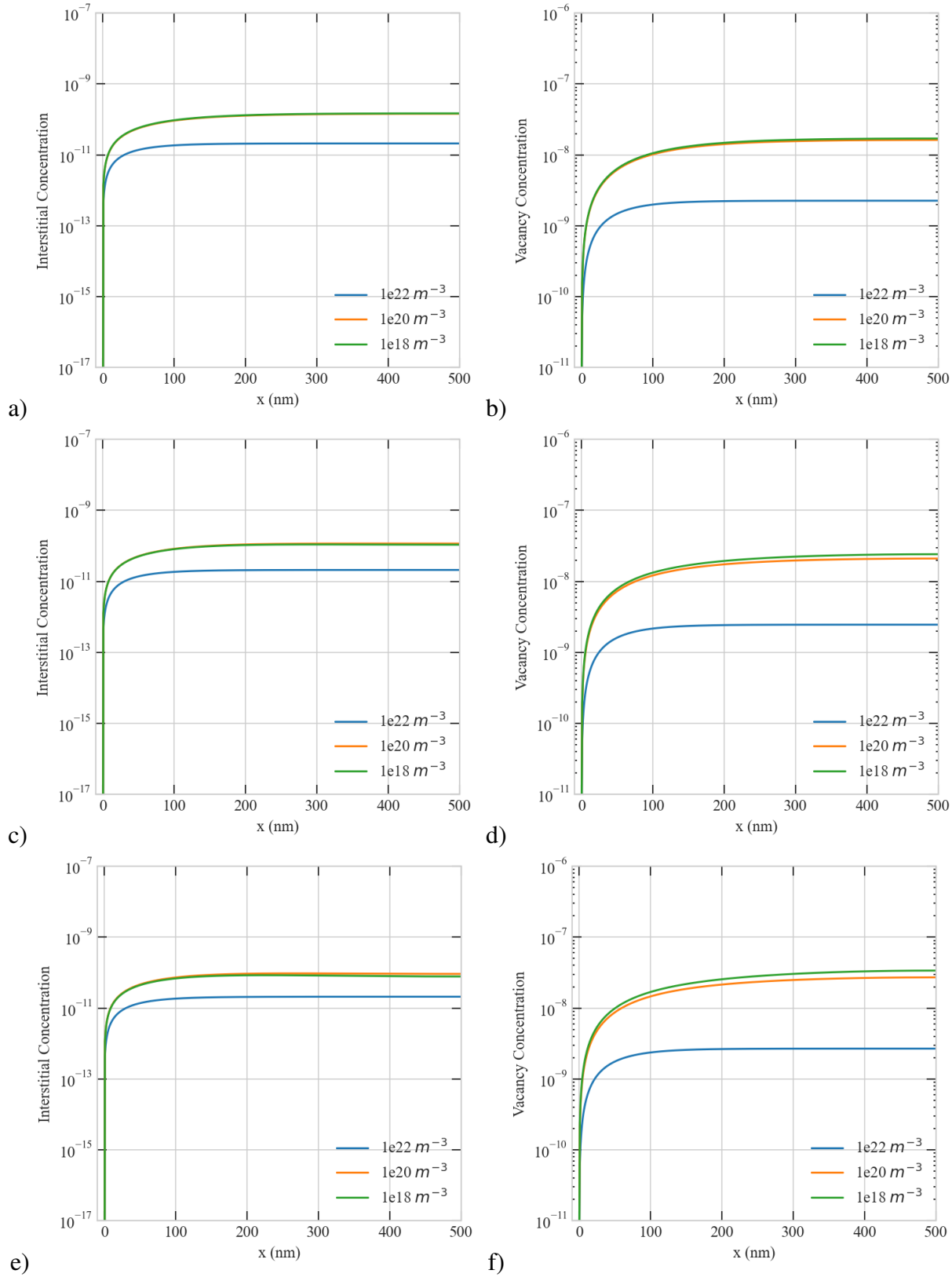

Figure 4.28: Effect of sink density on the steady-state concentration profiles of point defects in a 500 nm at 5.6e-6 dpa/s a) a) 1% bias, interstitial b) 1% bias, vacancy c) 10% bias, interstitial d) 10% bias, vacancy e) 20% bias, interstitial and f) 20% bias, vacancy concentrations.

In Fig. 4.29, we observed that at the dose rate of 1e-2 dpa/s, the amount of Cr depletion at the boundary decreases drastically when the sink density increases in 500 nm. Furthermore, the concentration of interstitials and vacancies also decreases with sink density, and effect of the sink density on interstitial and vacancy concentrations become more evident (see Fig. 4.30). We have previously shown that this result was valid for 300 nm as well, but it becomes more noticeable in 500 nm. Thus, observations imply that increasing the sink density leads to a direct decrease in Cr concentration when the size is above 100 nm.

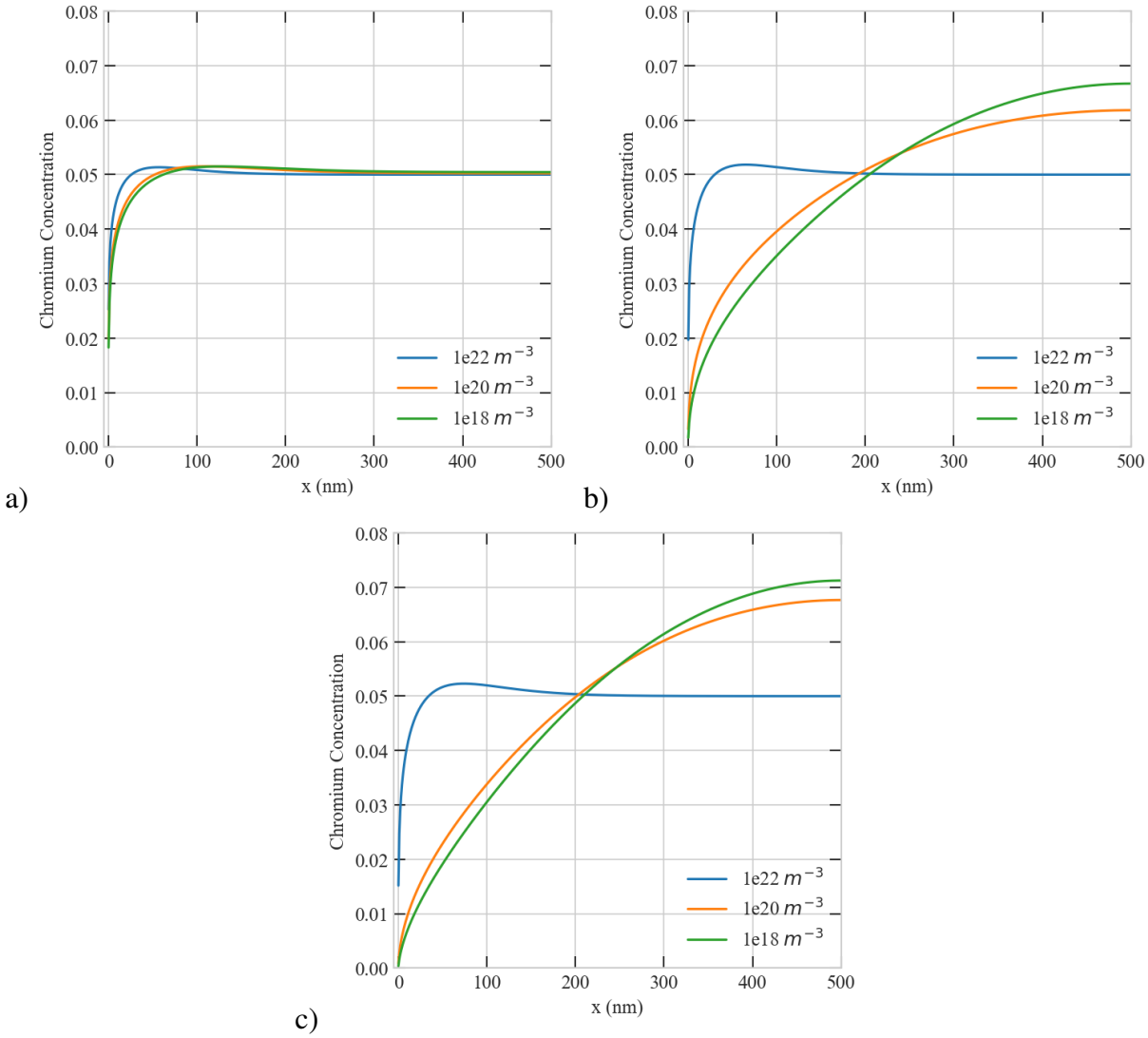

Figure 4.29: Effect of sink density on the steady-state concentration profiles of Chromium in a 500 nm at 1e-4 dpa/s a) 1% bias, Cr concentration b) 10% bias, Cr concentration c) 20% bias, Cr concentration.

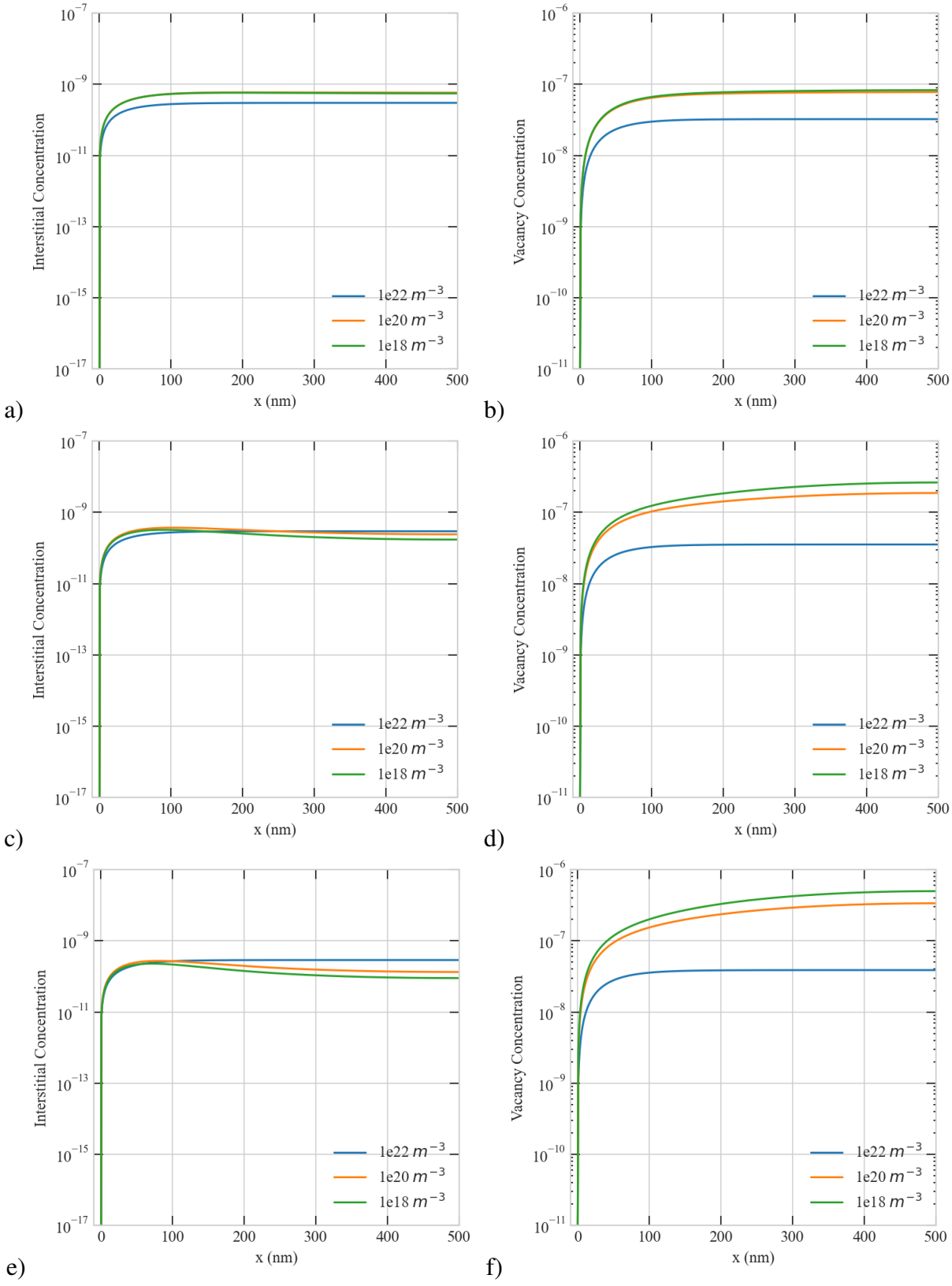

Figure 4.30: Effect of sink density on the steady-state concentration profiles of point defects in a 500 nm at 1e-4 dpa/s a) 1% bias, interstitial b) 1% bias, vacancy c) 10% bias, interstitial d) 10% bias, vacancy e) 20% bias, interstitial and f) 20% bias, vacancy concentrations.

In Fig. 4.32, vacancy and interstitial concentrations start to show opposite trends, as we discussed above. The anomaly in the dependence of interstitial accumulation leads to instability. While this instability is not seen at the dose rate of 1e-4 dpa/s with any biases, it begins to be evident even with 1% production bias at the dose rate of 1e-2 dpa/s. Therefore, the Cr concentration profile differed from the 1e-2 dpa/s dose rate and 1% bias than at the dose rate of 1e-4 dpa/s and 1% bias (Fig. 4.29 and Fig. 4.31). Here, we did not observe this instability for 1e22 m^{-3} sink density in 500 nm.

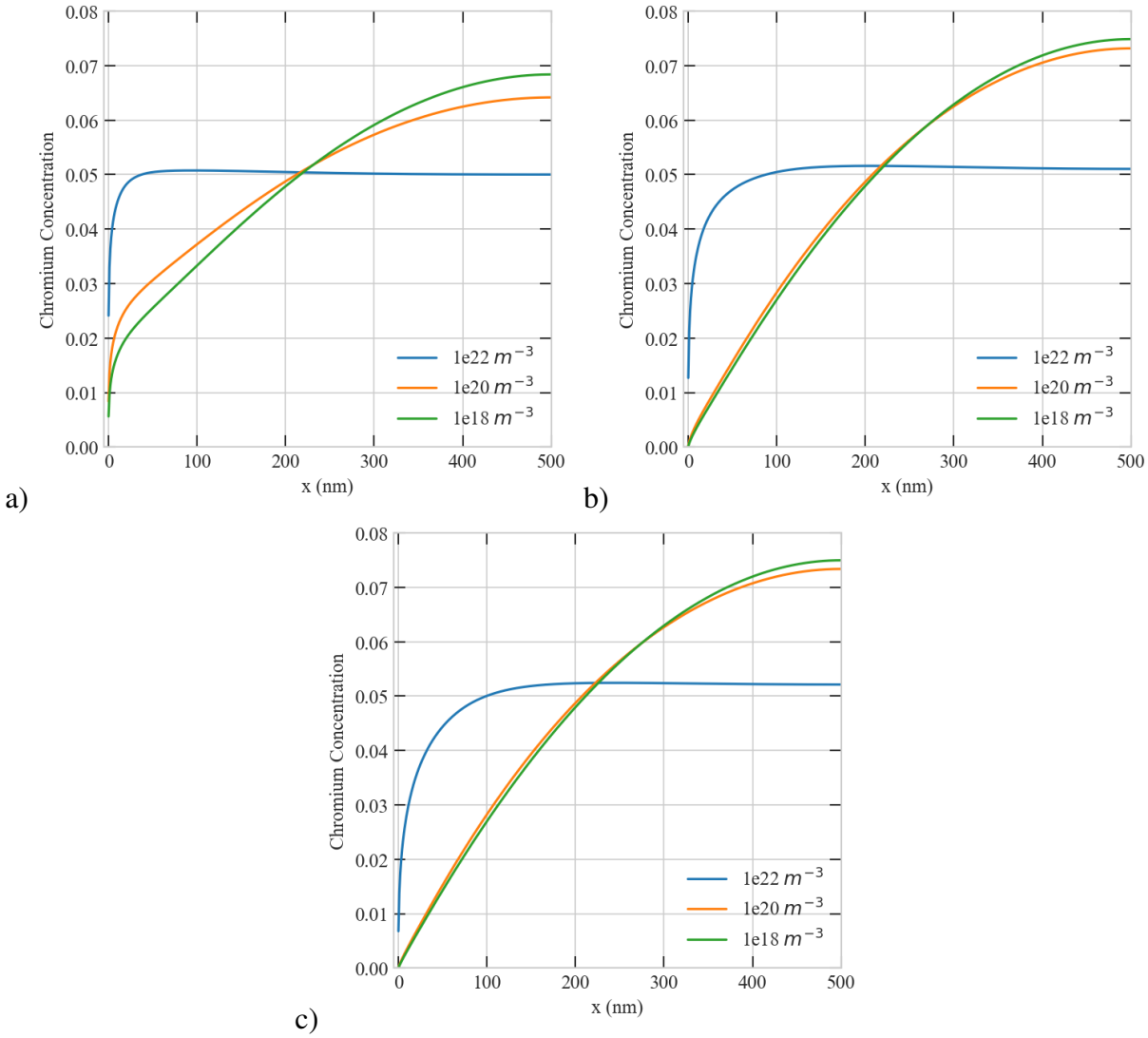

Figure 4.31: Effect of sink density on the steady-state concentration profiles of Chromium in a 500 nm at 1e-2 dpa/s a) 1% bias, Cr concentration b) 10% bias, Cr concentration c) 20% bias, Cr concentration.

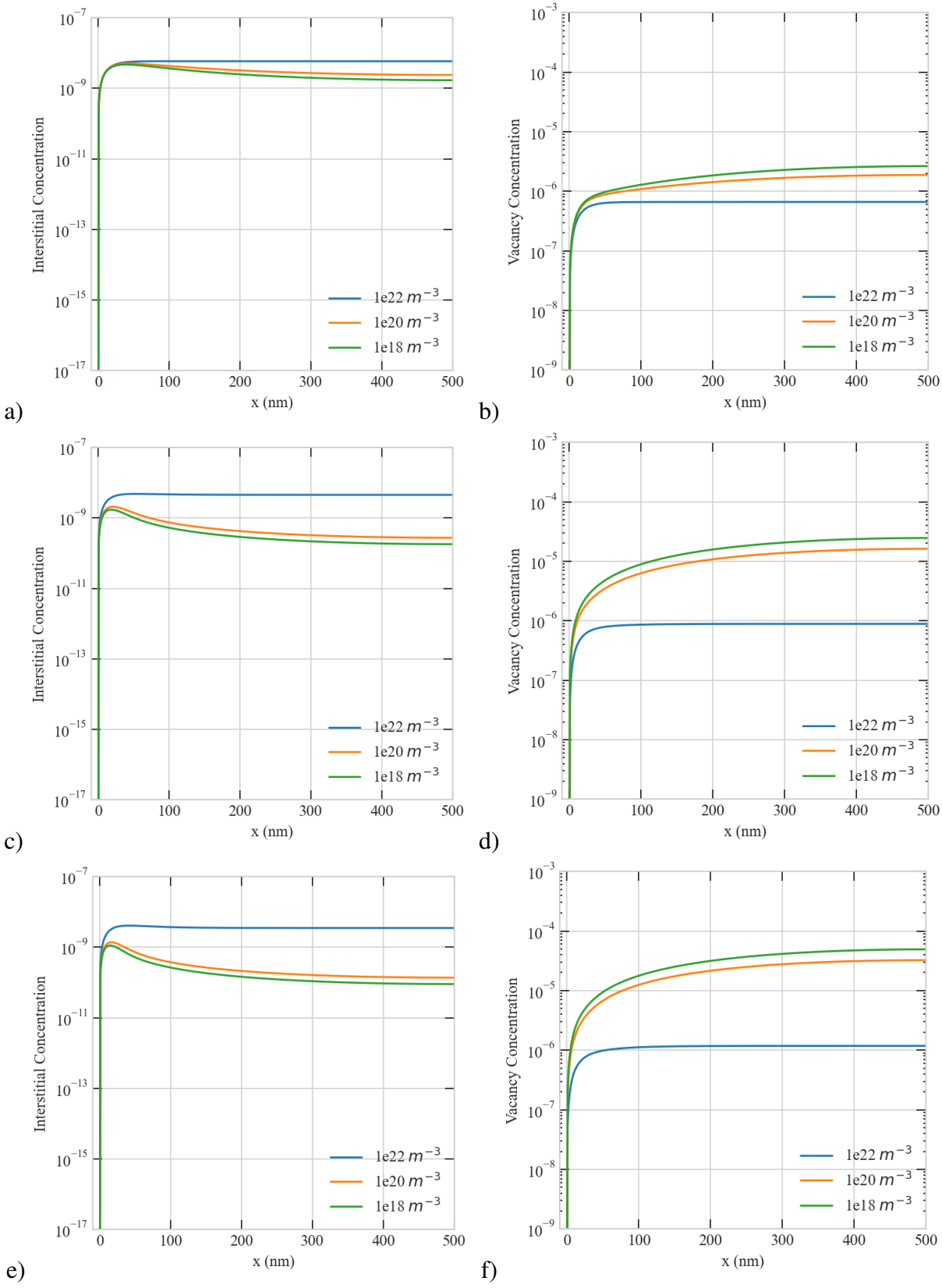

Figure 4.32: Effect of sink density on the steady-state concentration profiles of point defects in a 500 nm at 1e-2 dpa/s a) 1% bias, interstitial b) 1% bias, vacancy c) 10% bias, interstitial d) 10% bias, vacancy e) 20% bias, interstitial and f) 20% bias, vacancy concentrations.

Fig. 4.34 presents that at the dose rate of 5.6e-6 dpa/s, an anomaly in the dependence of interstitial concentration is more pronounced for 1e18 m^{-3} sink density in 5000 nm. Depending on instability, Cr depletion layer is widened with bias (see Fig. 4.33).

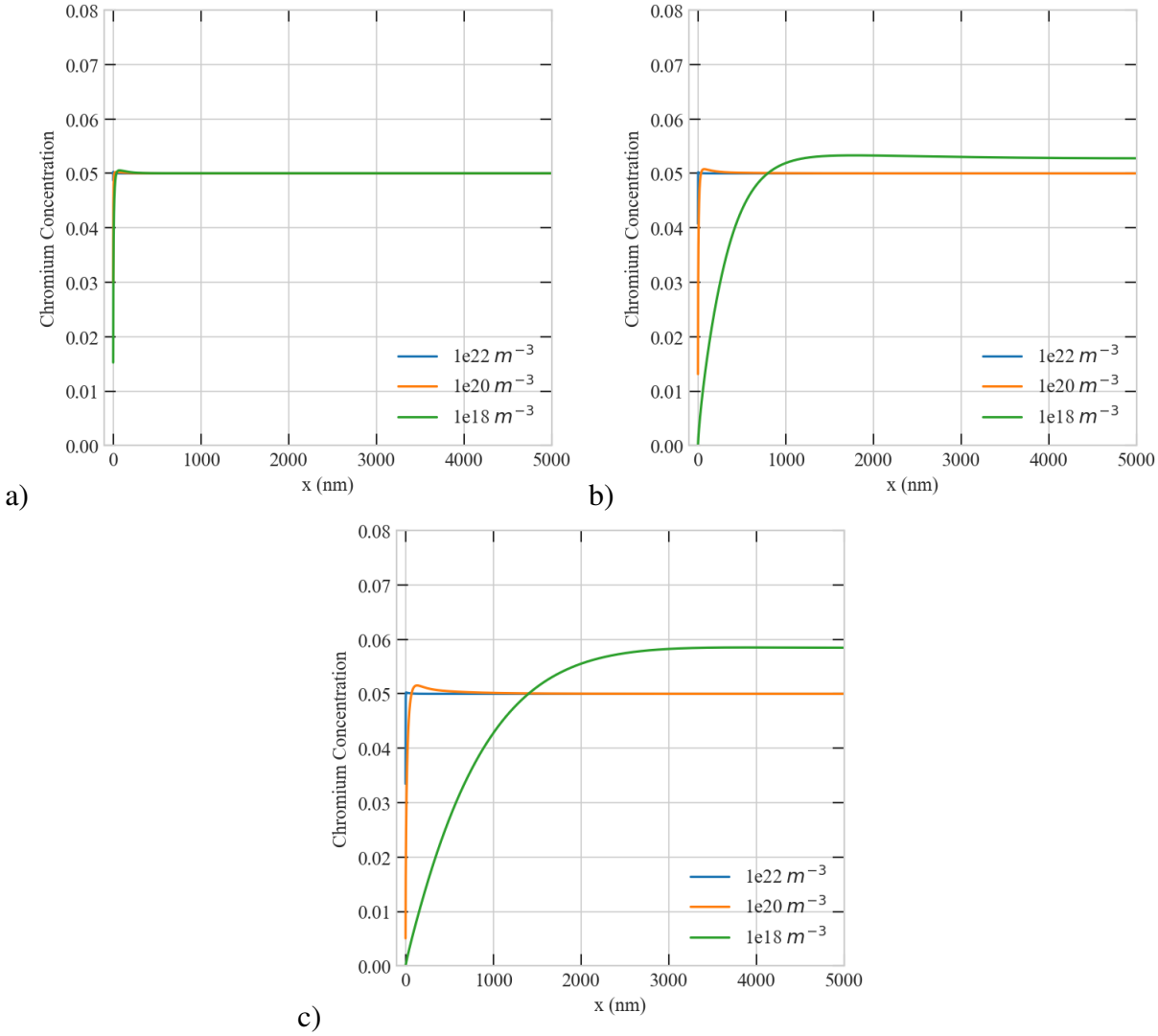

Figure 4.33: Effect of sink density on the steady-state concentration profiles of Chromium in a 5000 nm at 5.6e-6 dpa/s a) 1% bias, Cr concentration b) 10% bias, Cr concentration c) 20% bias, Cr concentration.

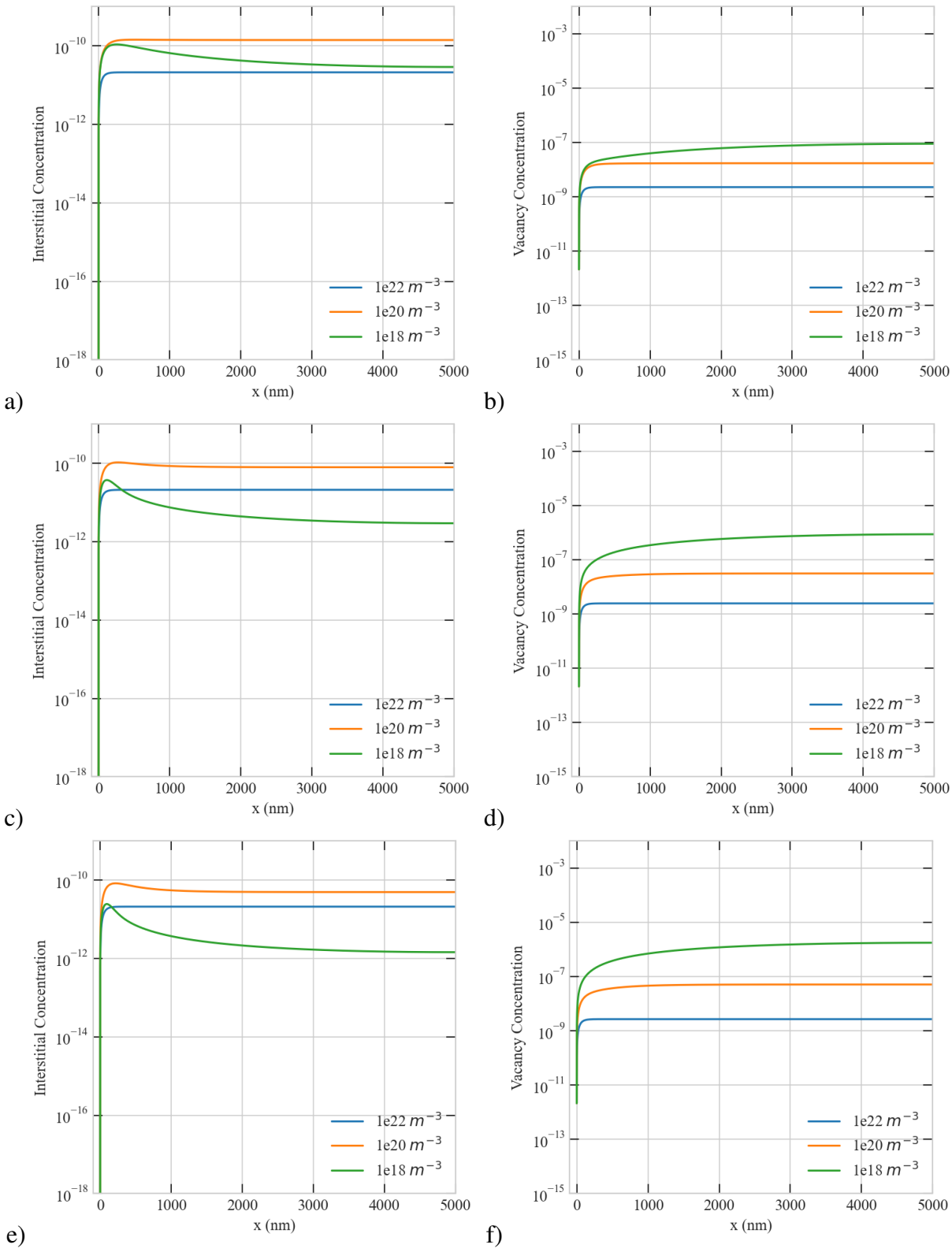

Figure 4.34: Effect of sink density on the steady-state concentration profiles of point defects in a 5000 nm at 5.6e-6 dpa/s a) 1% bias, interstitial b) 1% bias, vacancy c) 10% bias, interstitial d) 10% bias, vacancy e) 20% bias, interstitial and f) 20% bias, vacancy concentrations.

Fig. 4.36 shows that at the dose rate of 1e-4 dpa/s, instability becomes more noticeable for 1e18 m^{-3} sink density even with 1% bias. Hence, Cr depletion layer is wider than at the dose rate of 5.6e-6 dpa/s in 5000 nm (see Fig. 4.35).

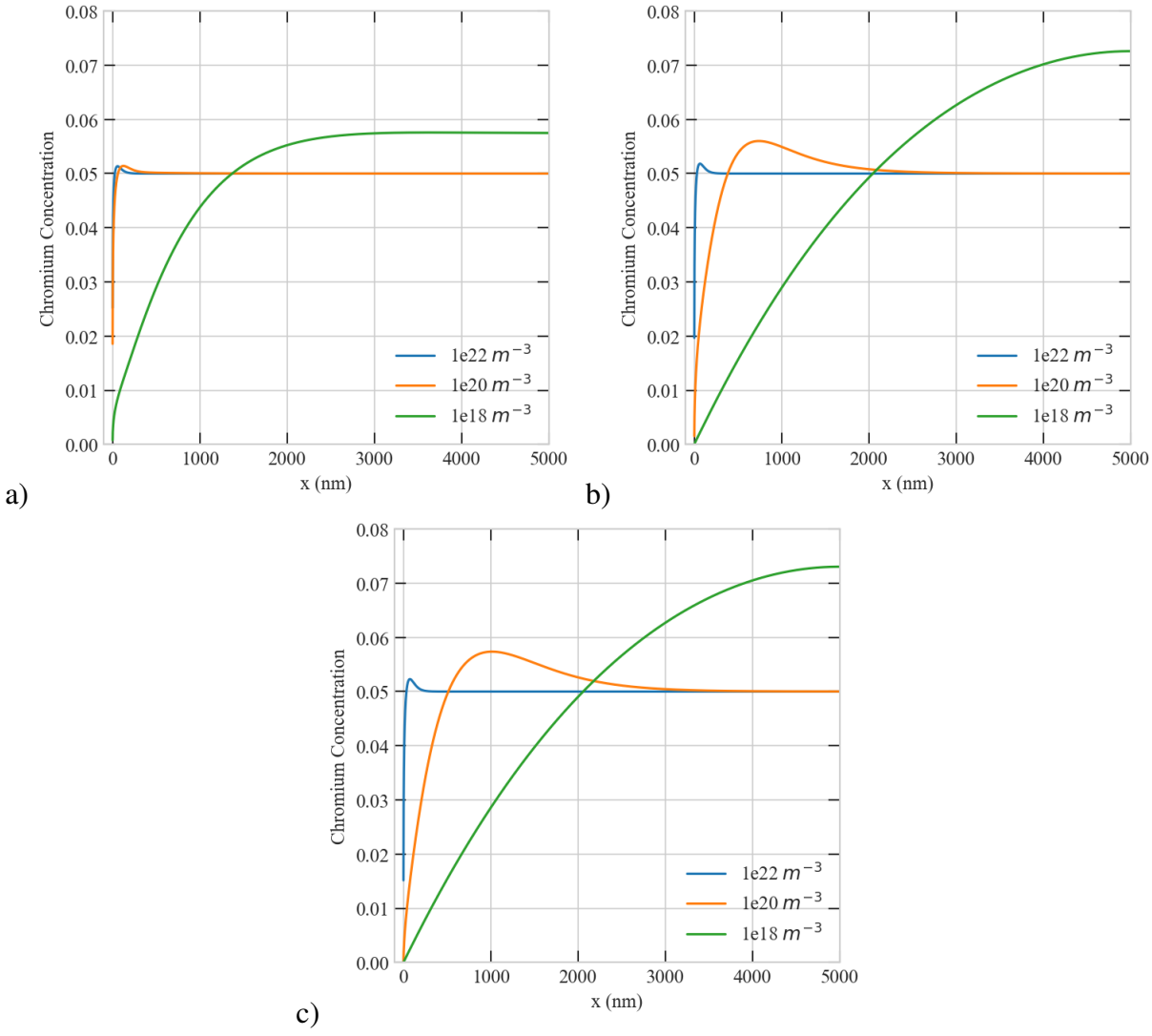

Figure 4.35: Effect of sink density on the steady-state concentration profiles of Chromium in a 5000 nm at 1e-4 dpa/s a) 1% bias, Cr concentration b) 10% bias, Cr concentration c) 20% bias, Cr concentration.

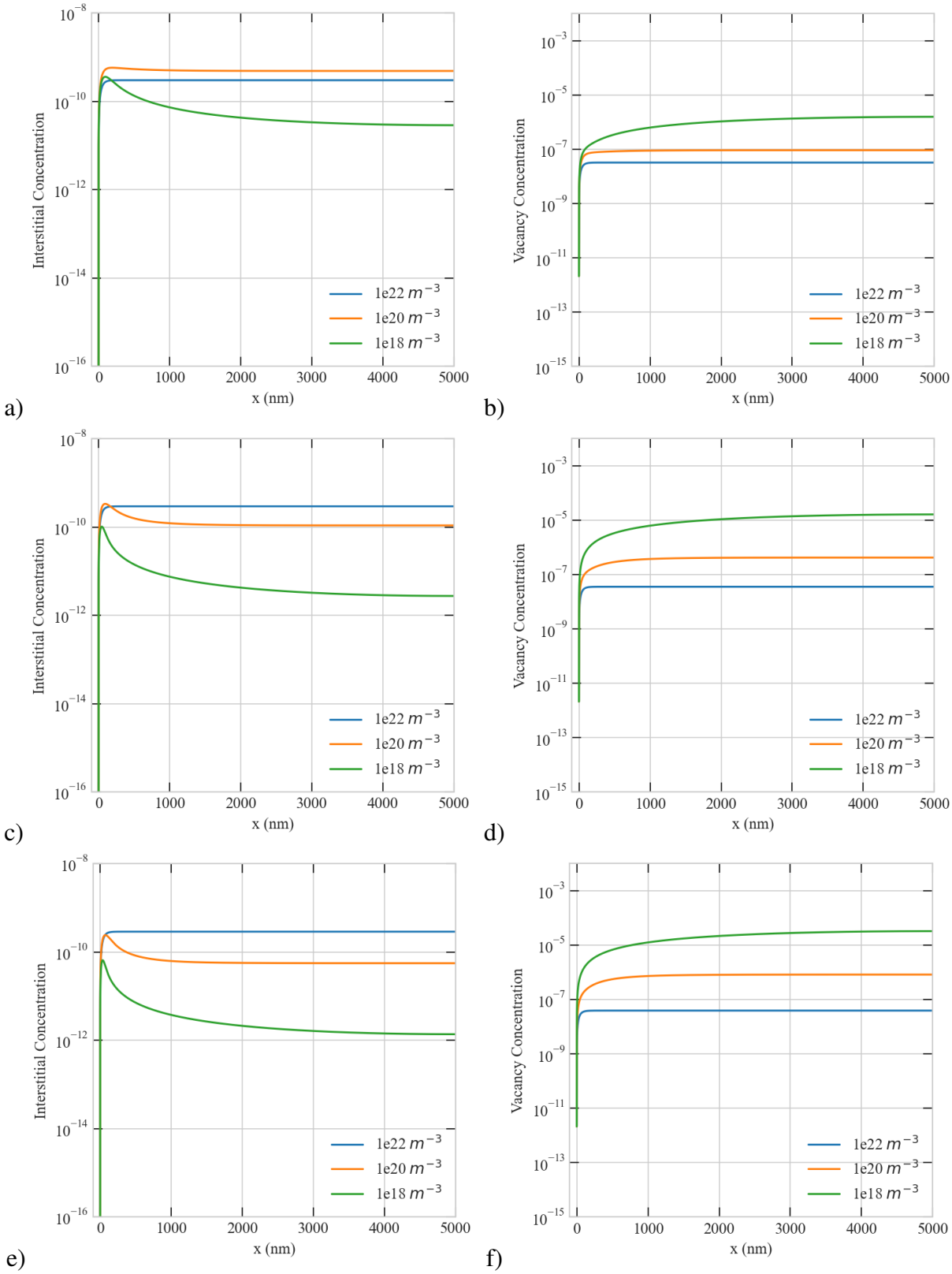

Figure 4.36: Effect of sink density on the steady-state concentration profiles of point defects in a 5000 nm at 1e-4 dpa/s a) 1% bias, interstitial b) 1% bias, vacancy c) 10% bias, interstitial d) 10% bias, vacancy e) 20% bias, interstitial and f) 20% bias, vacancy concentrations.

When we examined the Fig.4.38, we noticed that while vacancy concentration continues to increase with bias, its interstitial counterpart starts to decrease with bias. However, for 1e18 m^{-3} sink density, the width of Cr depletion layer stays similar in 5000 nm (see Fig. 4.37.

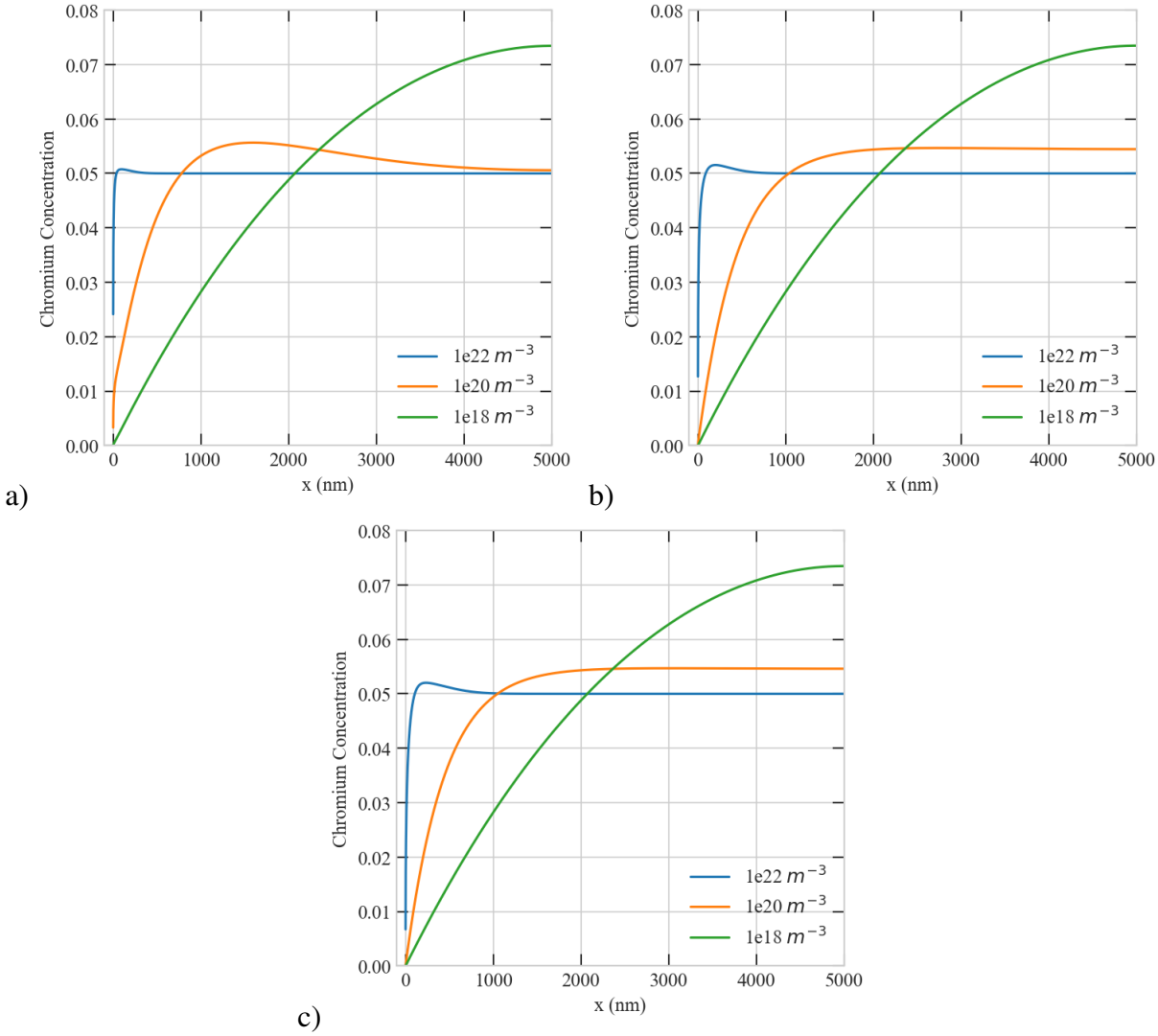

Figure 4.37: Effect of sink density on the steady-state concentration profiles of Chromium in a 5000 nm at 1e-2 dpa/s a) 1% bias, Cr concentration b) 10% bias, Cr concentration c) 20% bias, Cr concentration.

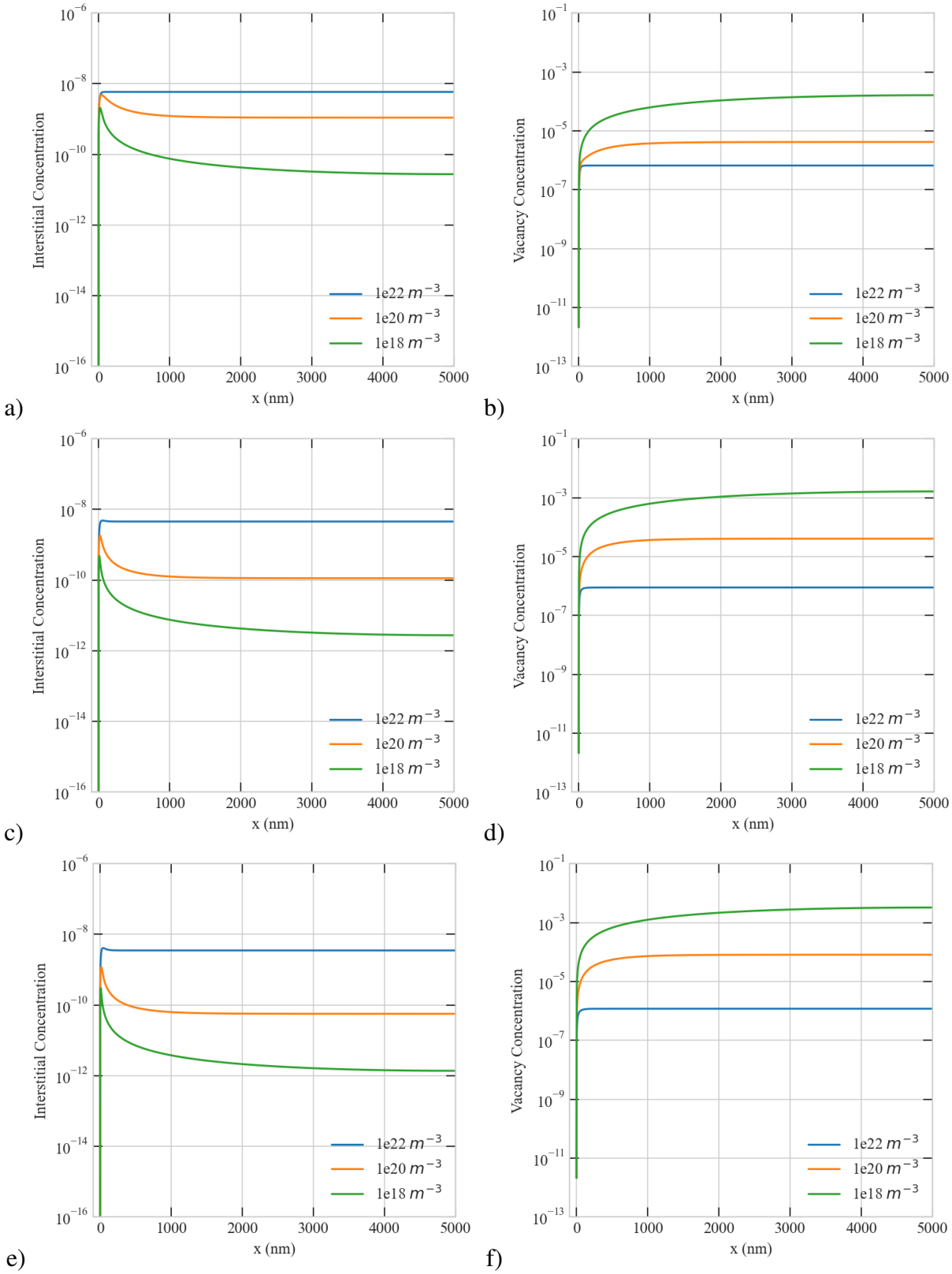

Figure 4.38: Effect of sink density on the steady-state concentration profiles of point defects in a 5000 nm at 1e-2 dpa/s a) 1% bias, interstitial b) 1% bias, vacancy c) 10% bias, interstitial d) 10% bias, vacancy e) 20% bias, interstitial and f) 20% bias, vacancy concentrations.

At the dose rate of 5.6e-6 dpa/s, we observed effective instability for 1e18 m^{-3} sink density in 7500 nm (see Fig. 4.40). Here also, while vacancy concentration continues to increase with bias, its interstitial counterpart starts to decrease with bias. However, for 1e20 m^{-3} sink density, this instability still not significant on defect concentrations. For 1e18 m^{-3} sink density, Cr depletion layer is widened with production bias (see Fig. 4.39).

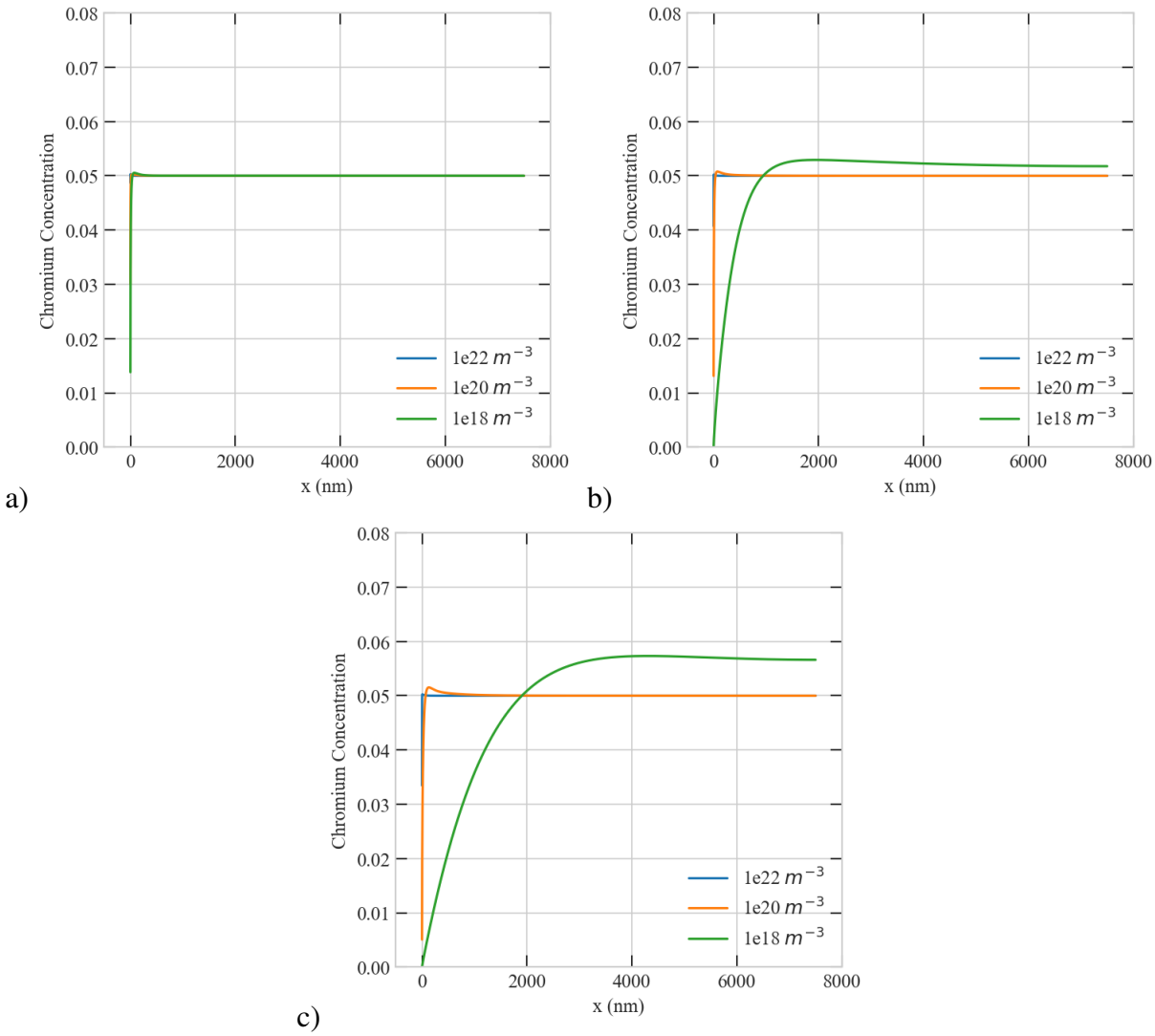

Figure 4.39: Effect of sink density on the steady-state concentration profiles of Chromium in a 7500 nm at 5.6e-6 dpa/s a) 1% bias, Cr concentration b) 10% bias, Cr concentration c) 20% bias, Cr concentration.

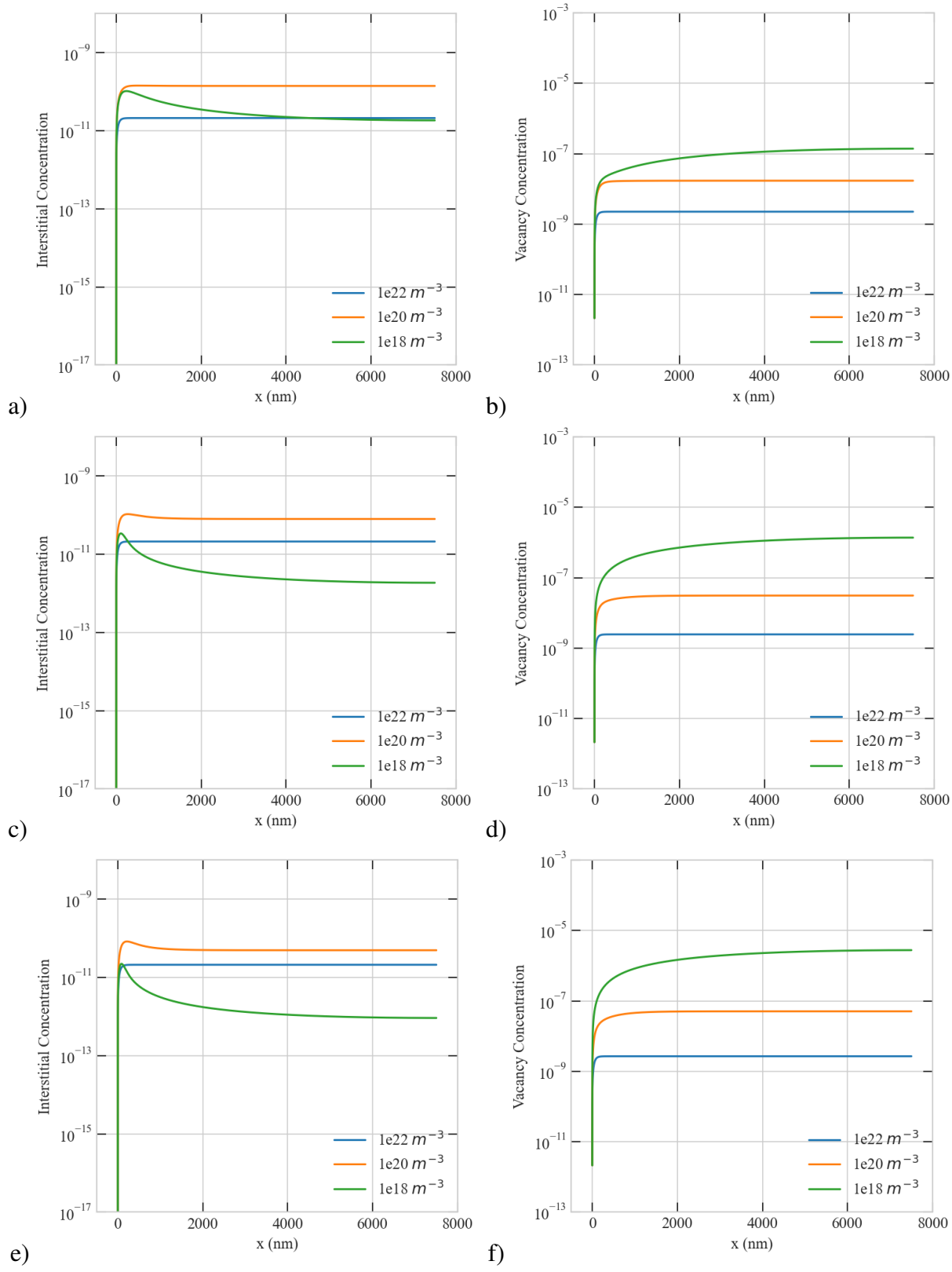

Figure 4.40: Effect of sink density on the steady-state concentration profiles of point defects in a 7500 nm at 5.6e-6 dpa/s a) 1% bias, interstitial b) 1% bias, vacancy c) 10% bias, interstitial d) 10% bias, vacancy e) 20% bias, interstitial and f) 20% bias, vacancy concentrations.

Here, at the dose rate of 1e-4 dpa/s, the anomaly in the dependence of interstitial accumulation (see Fig. 4.42) leads to increase in Cr depletion at the boundary. Besides, it becomes more evident with the increase in production bias in 7500 nm (see Fig. 4.41).

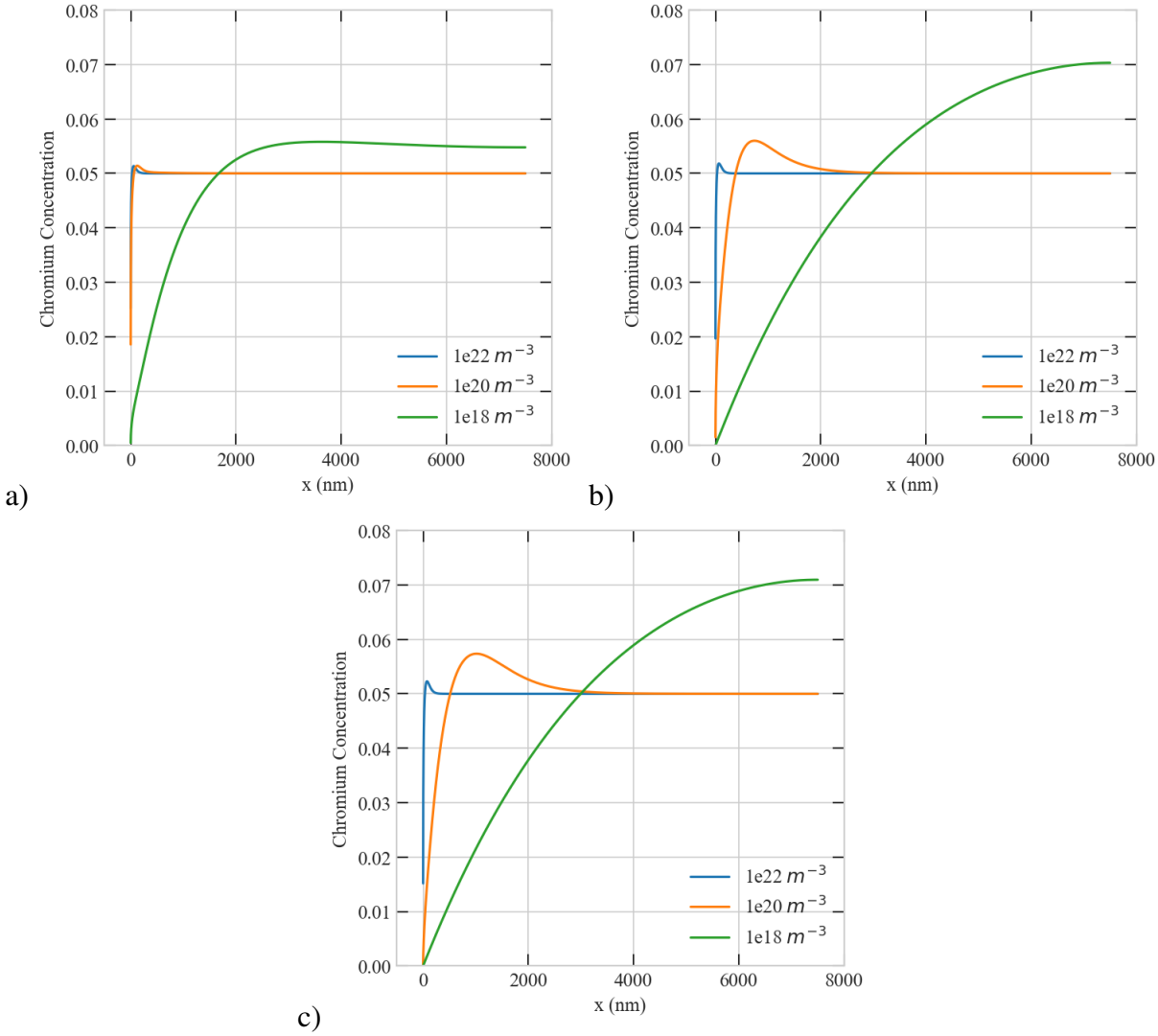

Figure 4.41: Effect of sink density on the steady-state concentration profiles of Chromium in a 7500 nm at 1e-4 dpa/s a) 1% bias, Cr concentration b) 10% bias, Cr concentration c) 20% bias, Cr concentration.

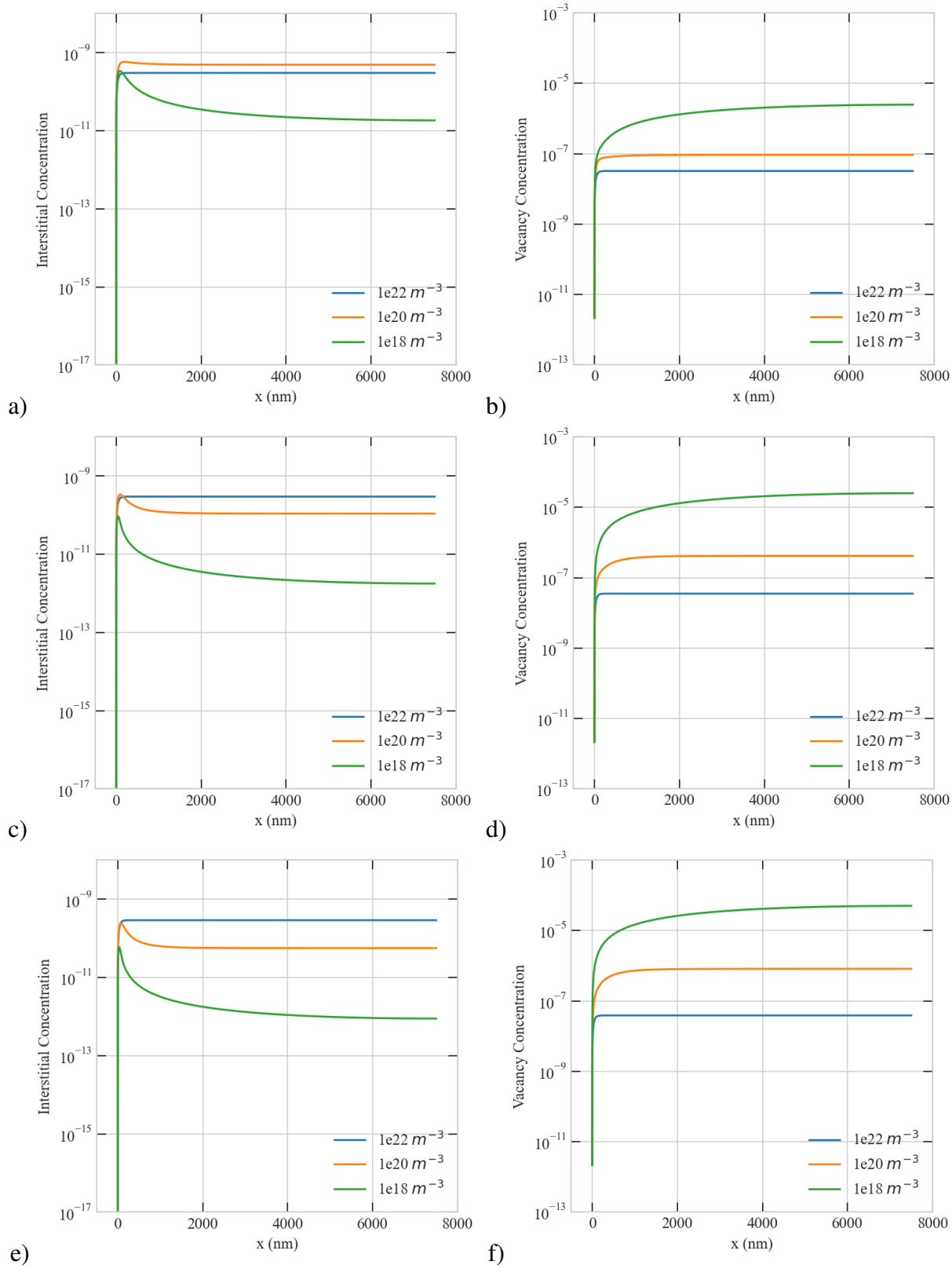

Figure 4.42: Effect of sink density on the steady-state concentration profiles of point defects in a 7500 nm at 1e-4 dpa/s a) 1% bias, interstitial b) 1% bias, vacancy c) 10% bias, interstitial d) 10% bias, vacancy e) 20% bias, interstitial and f) 20% bias, vacancy concentrations.

At the dose rate of 1e-2 dpa/s, vacancy concentration continues to increase with bias, and its interstitial counterpart decrease with bias (see Fig. 4.44). In Fig. 4.43, with the increase in dose rate (from 1e-4 to 1e-2 dpa/s), we observed that for 1e20 m^{-3} sink density, effect of sink density is more effective on Cr concentration at the near boundary in 7500 nm.

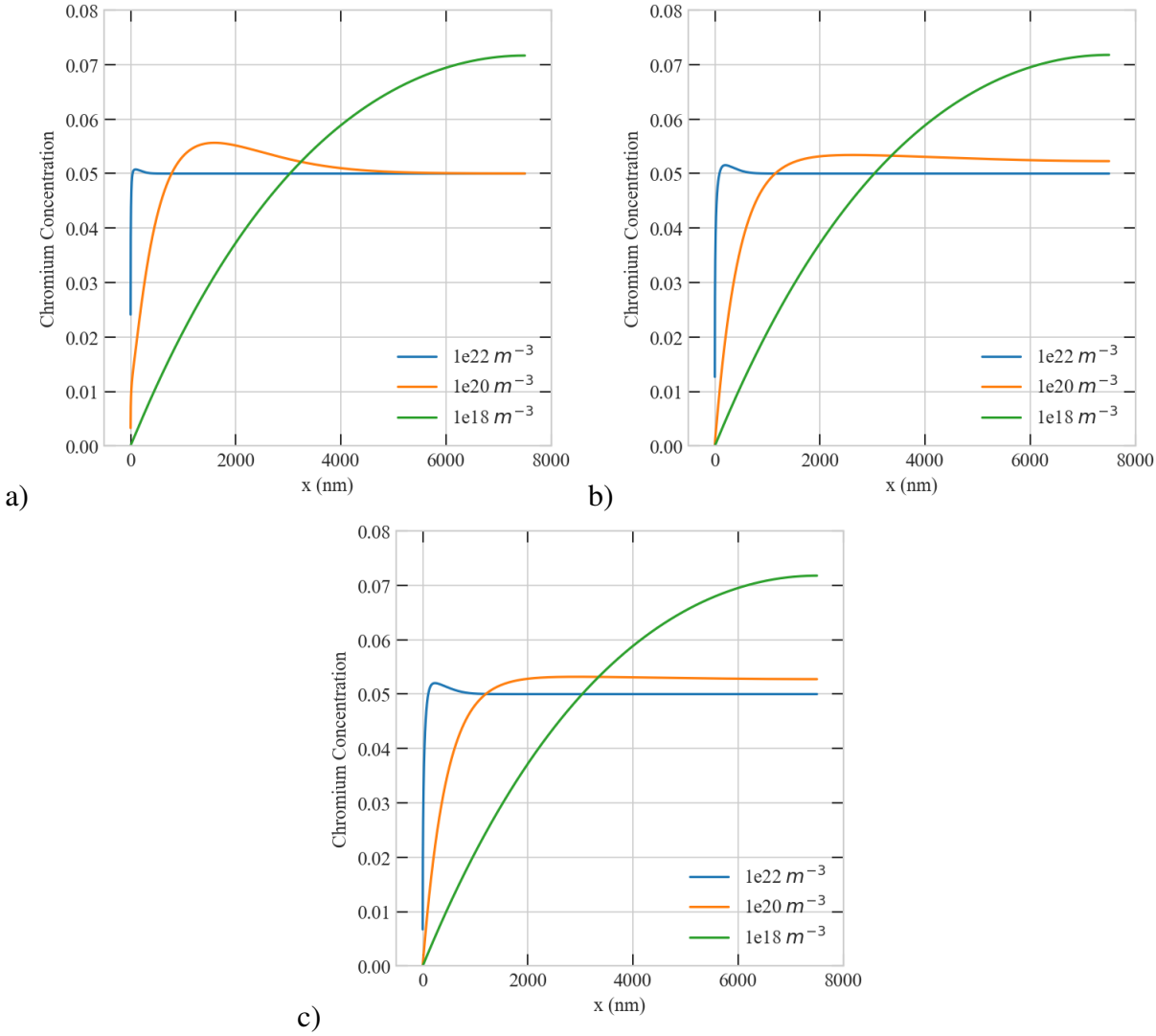

Figure 4.43: Effect of sink density on the steady-state concentration profiles of Chromium in a 7500 nm at 1e-2 dpa/s a) 1% bias, Cr concentration b) 10% bias, Cr concentration c) 20% bias, Cr concentration.

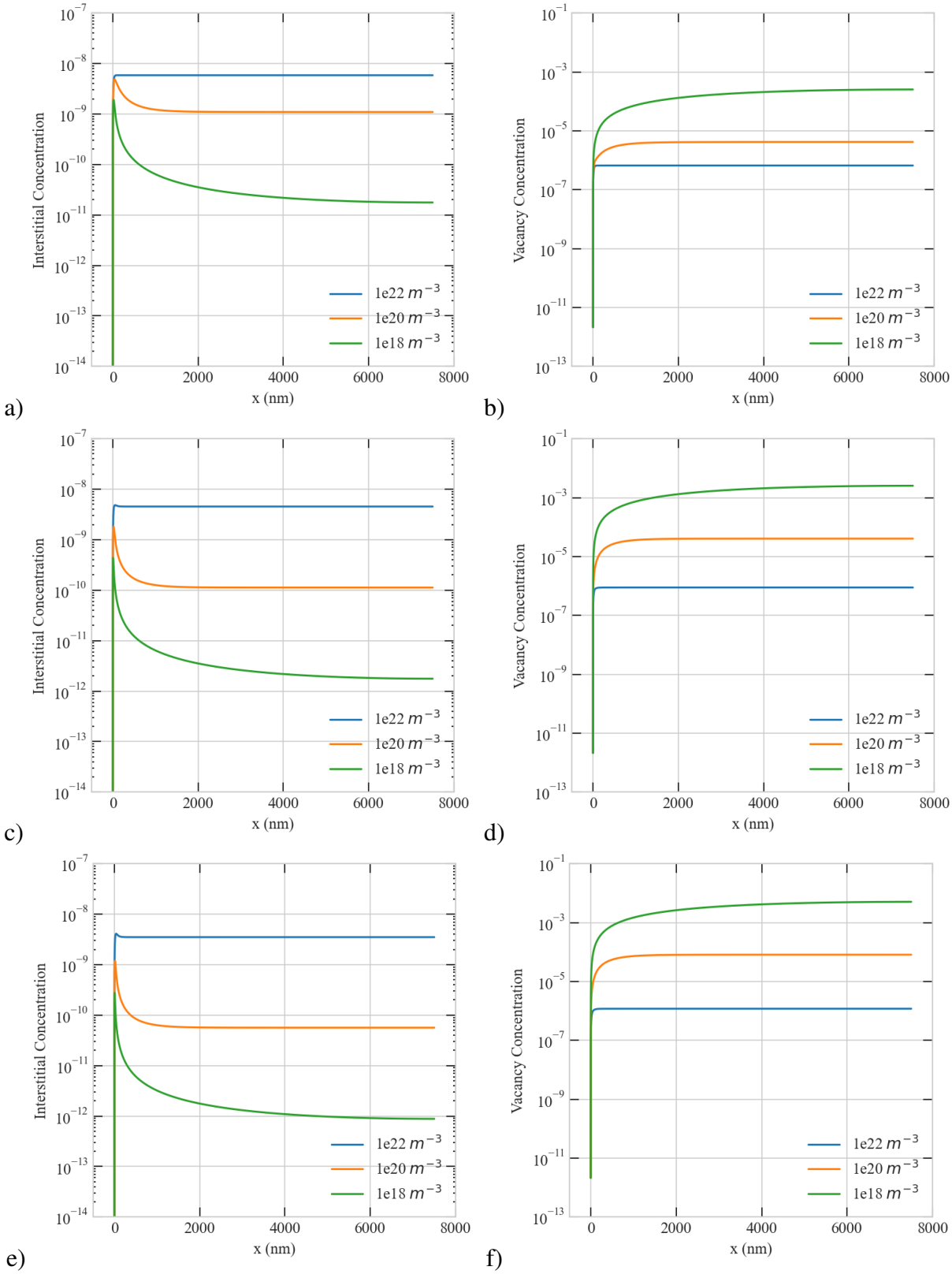

Figure 4.44: Effect of sink density on the steady-state concentration profiles of point defects in a 7500 nm at 1e-2 dpa/s a) 1% bias, interstitial b) 1% bias, vacancy c) 10% bias, interstitial d) 10% bias, vacancy e) 20% bias, interstitial and f) 20% bias, vacancy concentrations.

4.5.2 The Combined Effects of Microstructure and Irradiation Parameters at 573K

As shown in the Fig. 4.45, at 573 K, instability on point defects is not observed at the dose rate of 5.6e-6 dpa/s in 100 nm as in at 773 K. The difference between 1e18 and 1e20 m^{-3} sink densities has not yet become observable on the Cr concentration profile with the bias factor. As we discussed at 773 K.

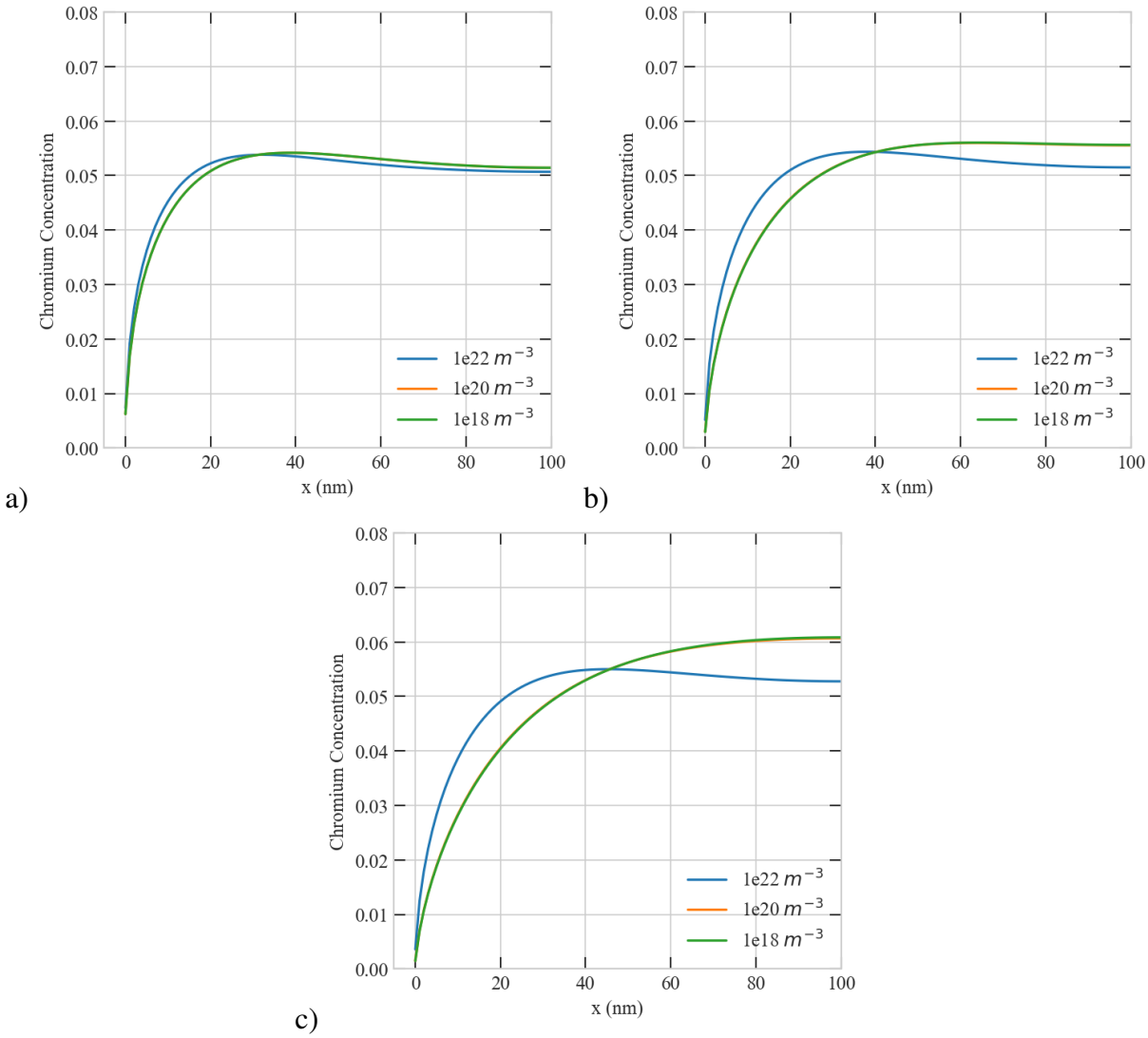

Figure 4.45: Effect of sink density on the steady-state concentration profiles of Chromium in a 100 nm at 5.6e-6 dpa/s a) 1% bias, Cr concentration b) 10% bias, Cr concentration c) 20% bias, Cr concentration.

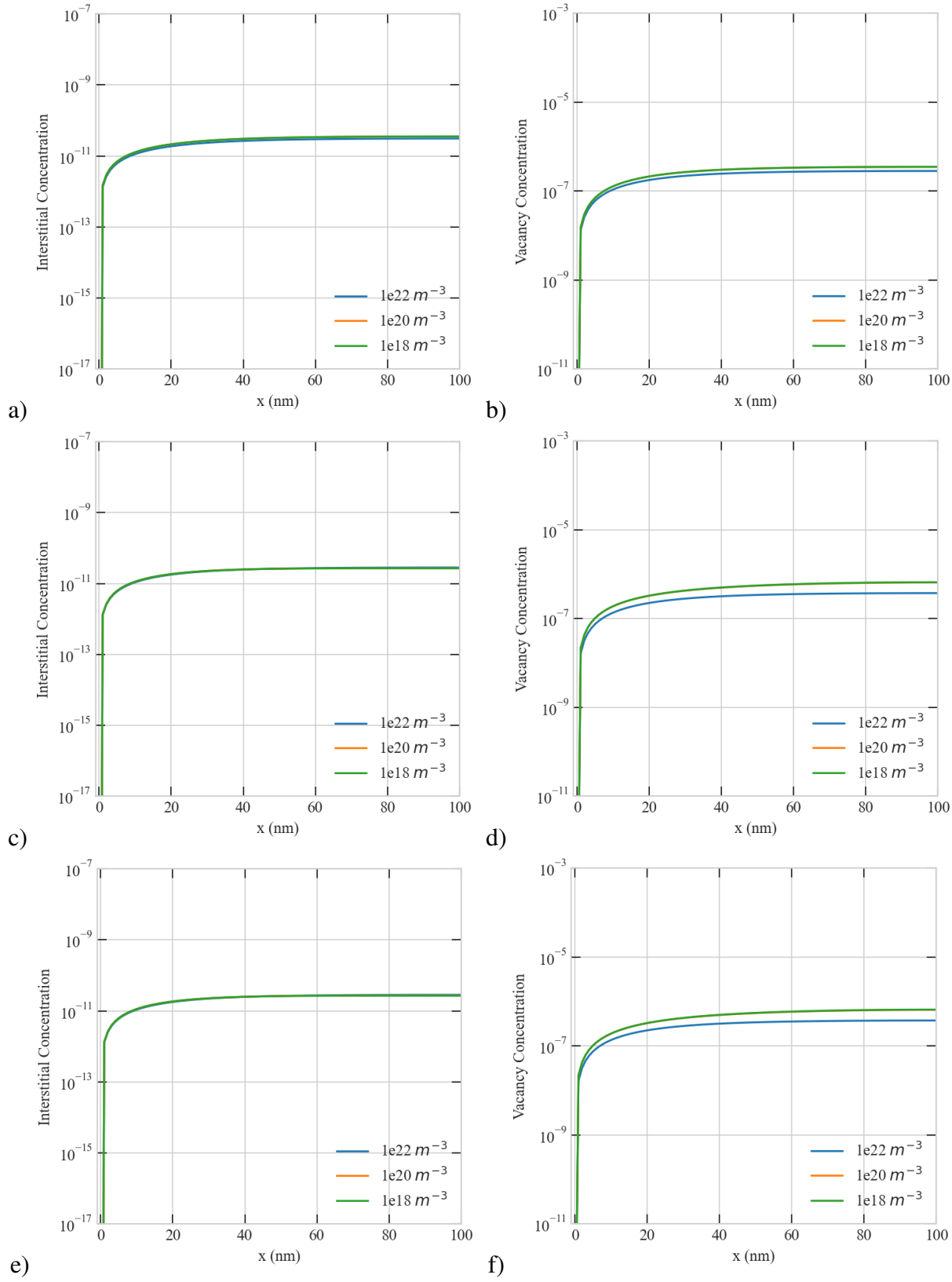

Figure 4.46: Effect of sink density on the steady-state concentration profiles of point defects in a 100 nm at 5.6e-6 dpa/s a) 1% bias, interstitial b) 1% bias, vacancy c) 10% bias, interstitial d) 10% bias, vacancy e) 20% bias, interstitial and f) 20% bias, vacancy concentrations.

At the dose rate of 1e-4 dpa/s and 10% bias, instability begins to be observed in 100 nm for 1e18 and 1e20 m^{-3} sink densities (see Fig. 4.48). As evident from the Fig. 4.47, the width of the Cr depletion layer increases with this instability.

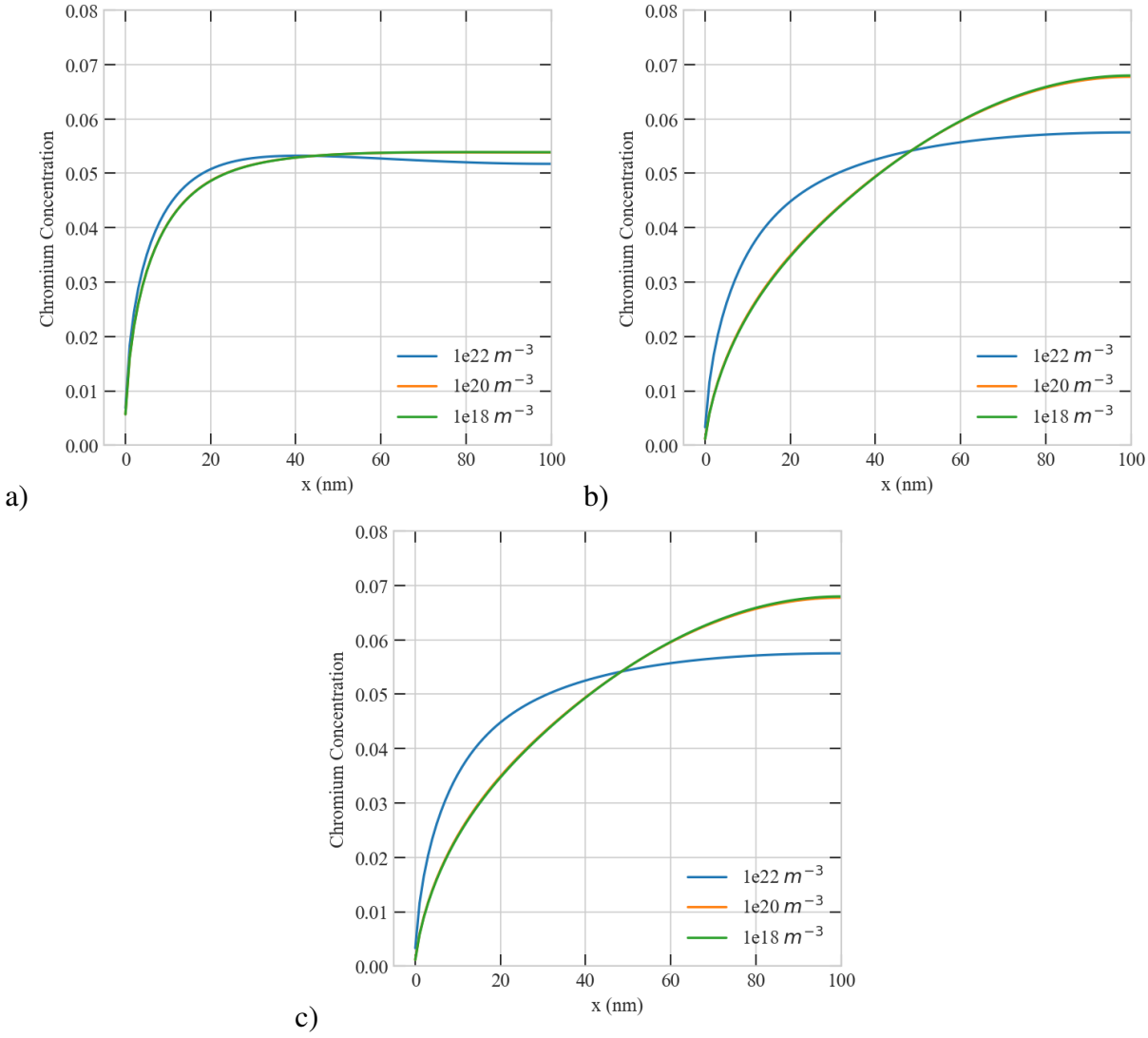

Figure 4.47: Effect of sink density on the steady-state concentration profiles of Chromium in a 100 nm at 1e-4 dpa/s a) 1% bias, Cr concentration b) 10% bias, Cr concentration c) 20% bias, Cr concentration.

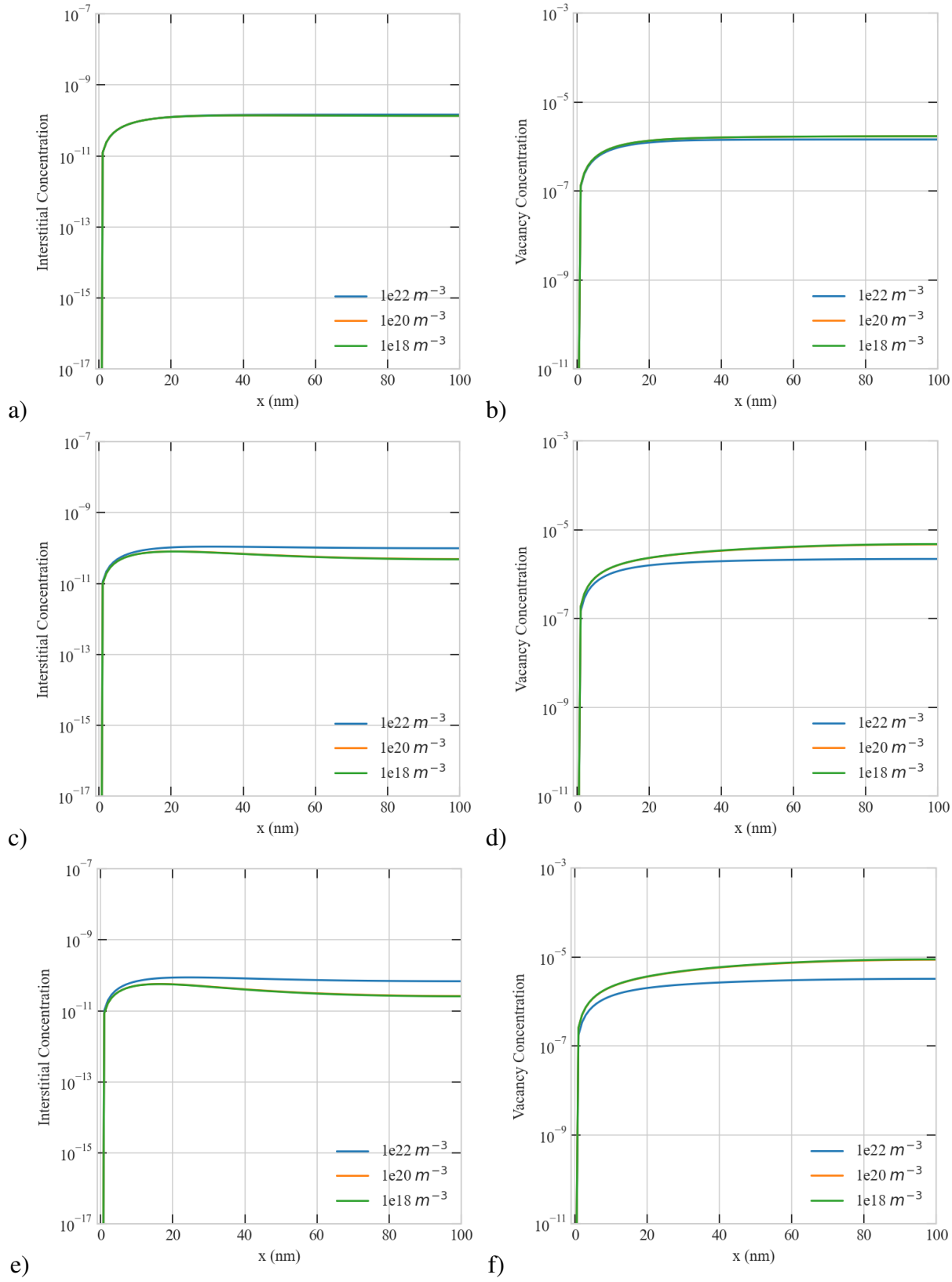

Figure 4.48: Effect of sink density on the steady-state concentration profiles of point defects in a 100 nm at 1e-4 dpa/s a) 1% bias, interstitial b) 1% bias, vacancy c) 10% bias, interstitial d) 10% bias, vacancy e) 20% bias, interstitial and f) 20% bias, vacancy concentrations.

In Fig. 4.51, instability appears effectively with increasing dose rate. Moreover, this instability rendered irradiation damage more pronounced at the dose rate of 1e-2 dpa/s even with 1% bias in 100 nm for three sink densities (see Fig. 4.49).

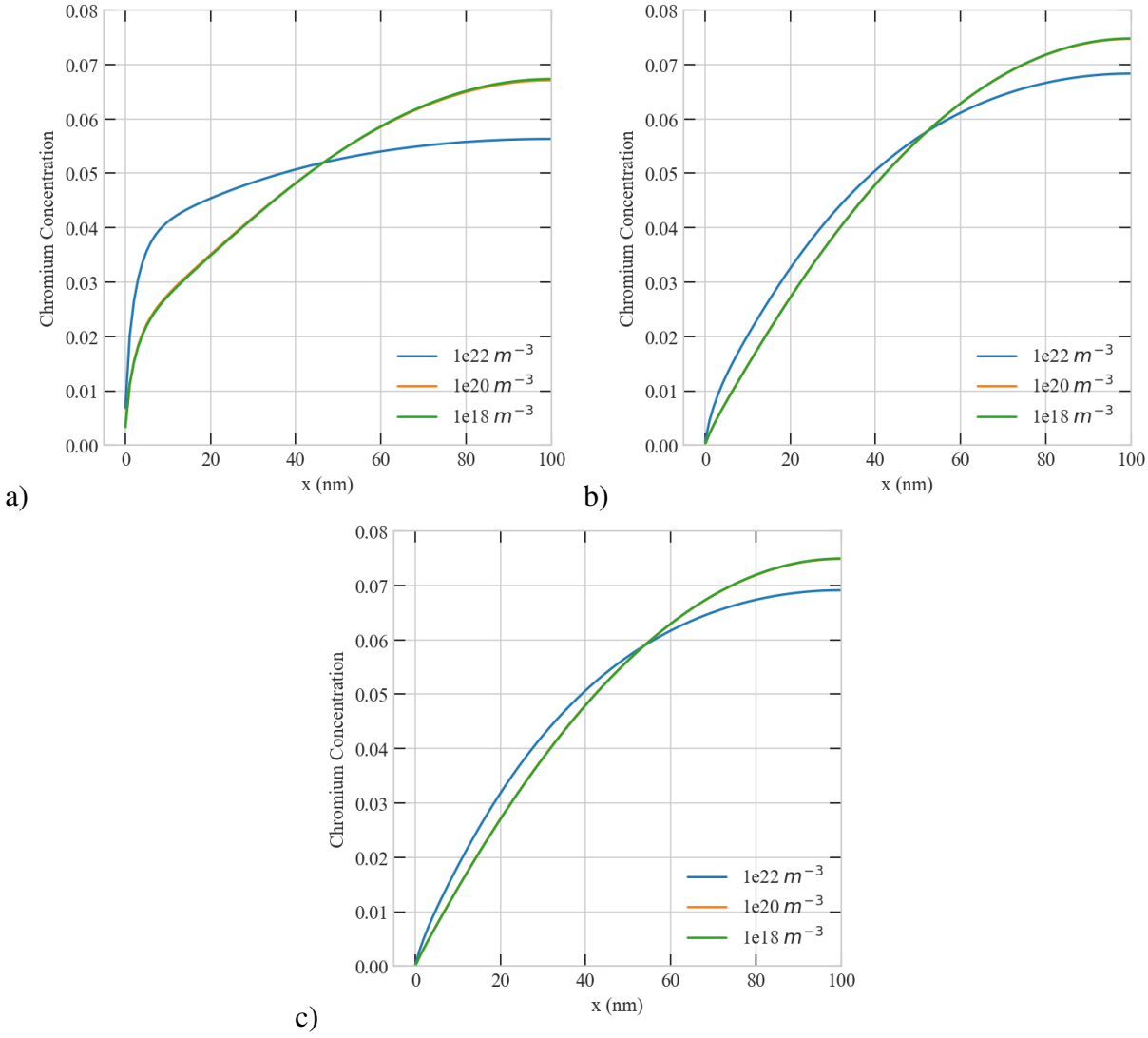

Figure 4.49: Effect of sink density on the steady-state concentration profiles of Chromium in a 100 nm at 1e-2 dpa/s a) 1% bias, Cr concentration b) 10% bias, Cr concentration c) 20% bias, Cr concentration.

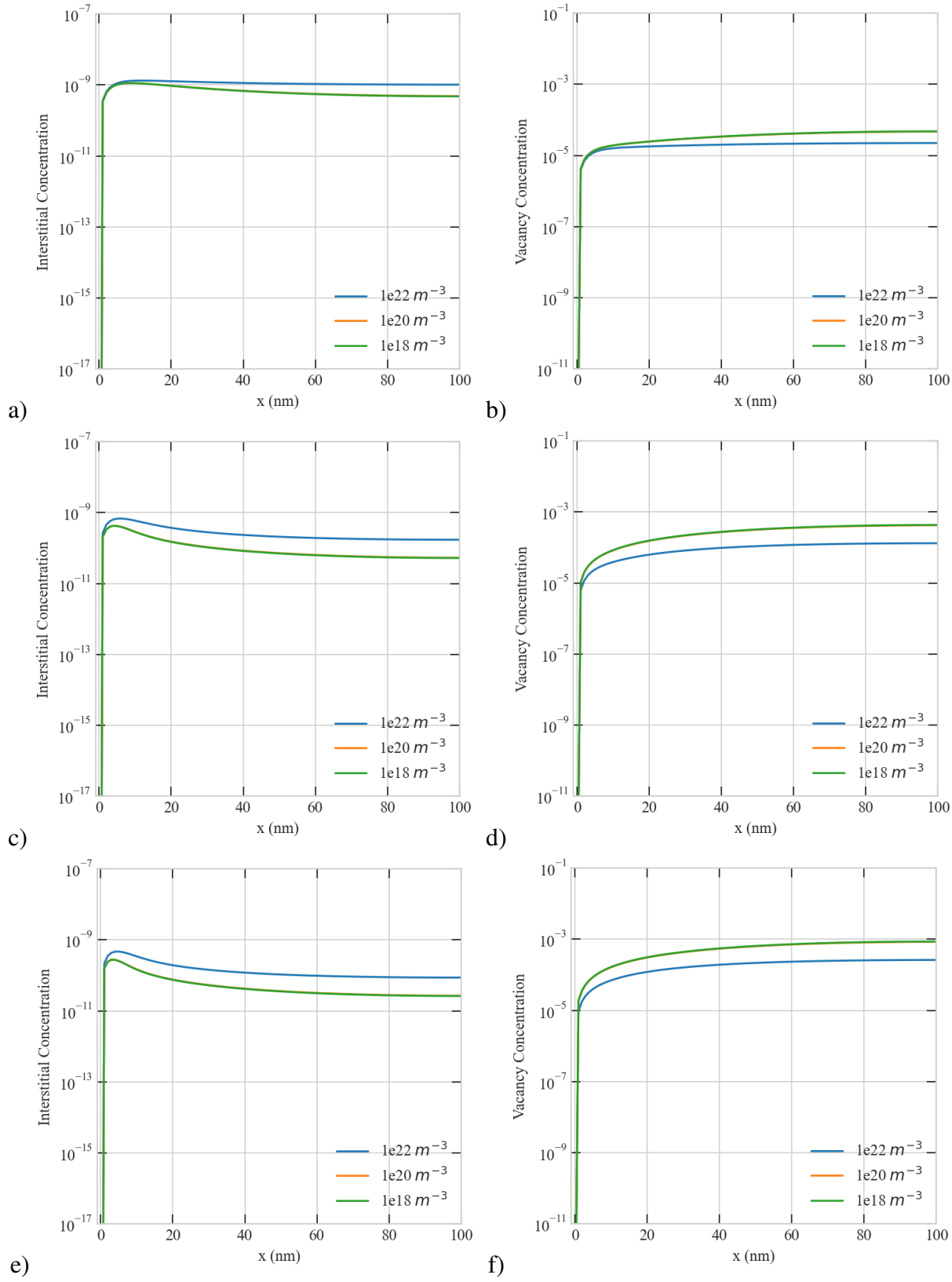

Figure 4.50: Effect of sink density on the steady-state concentration profiles of point defects in a 100 nm at 1e-2 dpa/s a) 1% bias, interstitial b) 1% bias, vacancy c) 10% bias, interstitial d) 10% bias, vacancy e) 20% bias, interstitial and f) 20% bias, vacancy concentrations.

In Fig. 4.51, instability is only observed with 10% bias in 300 nm. As shown in Fig. 4.49, for 1e18 and 1e20 m^{-3} sink densities, the magnitude of depletion of Cr at the boundary increases with bias in 300 nm. Nevertheless, Cr depletion profile for 1e22 m^{-3} sink density with 10% and 20% biases remains similar at the dose rate of 5.6e-6 dpa/s.

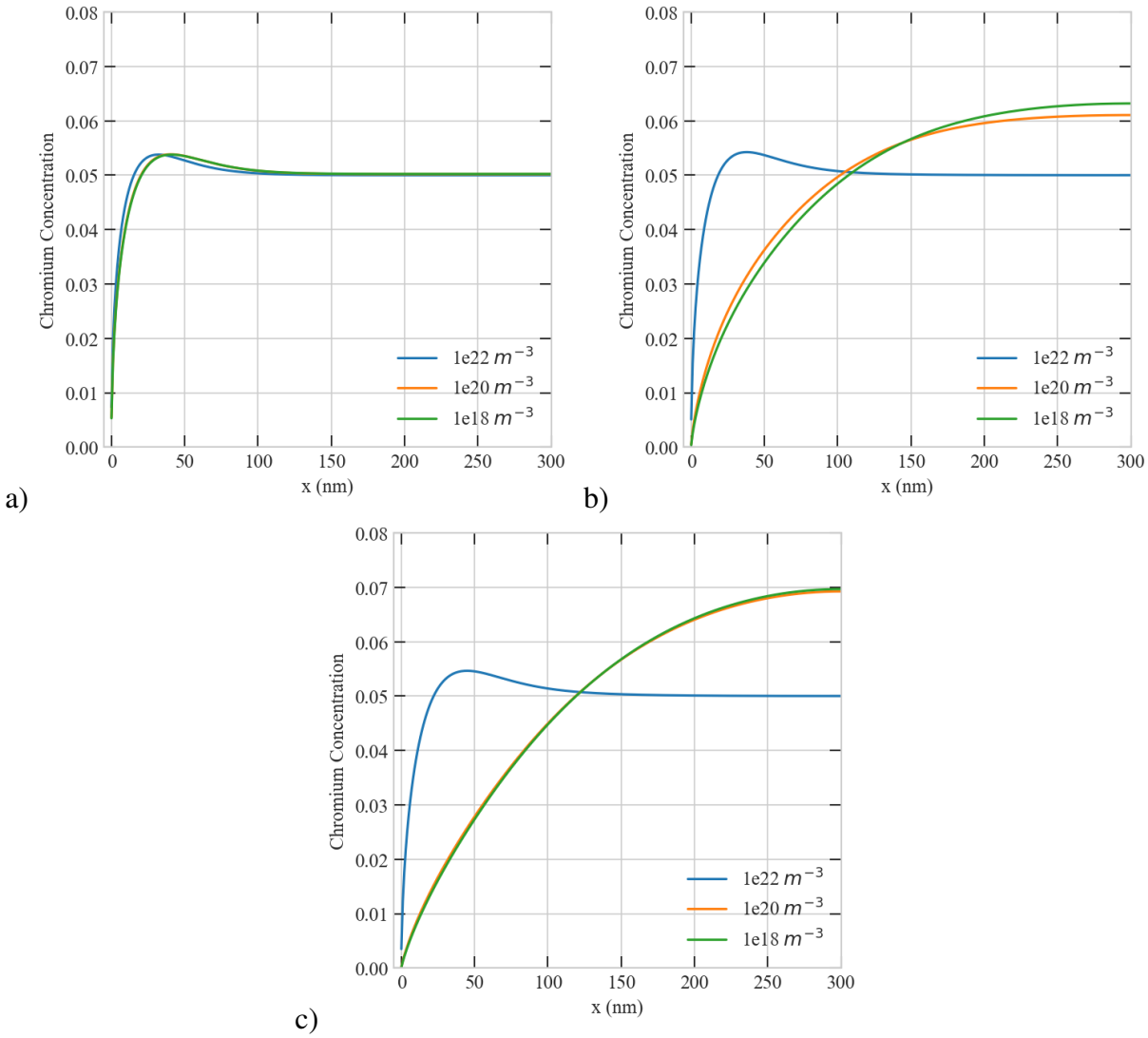

Figure 4.51: Effect of sink density on the steady-state concentration profiles of Chromium in a 300 nm at 5.6e-6 dpa/s a) 1% bias, Cr concentration b) 10% bias, Cr concentration c) 20% bias, Cr concentration.

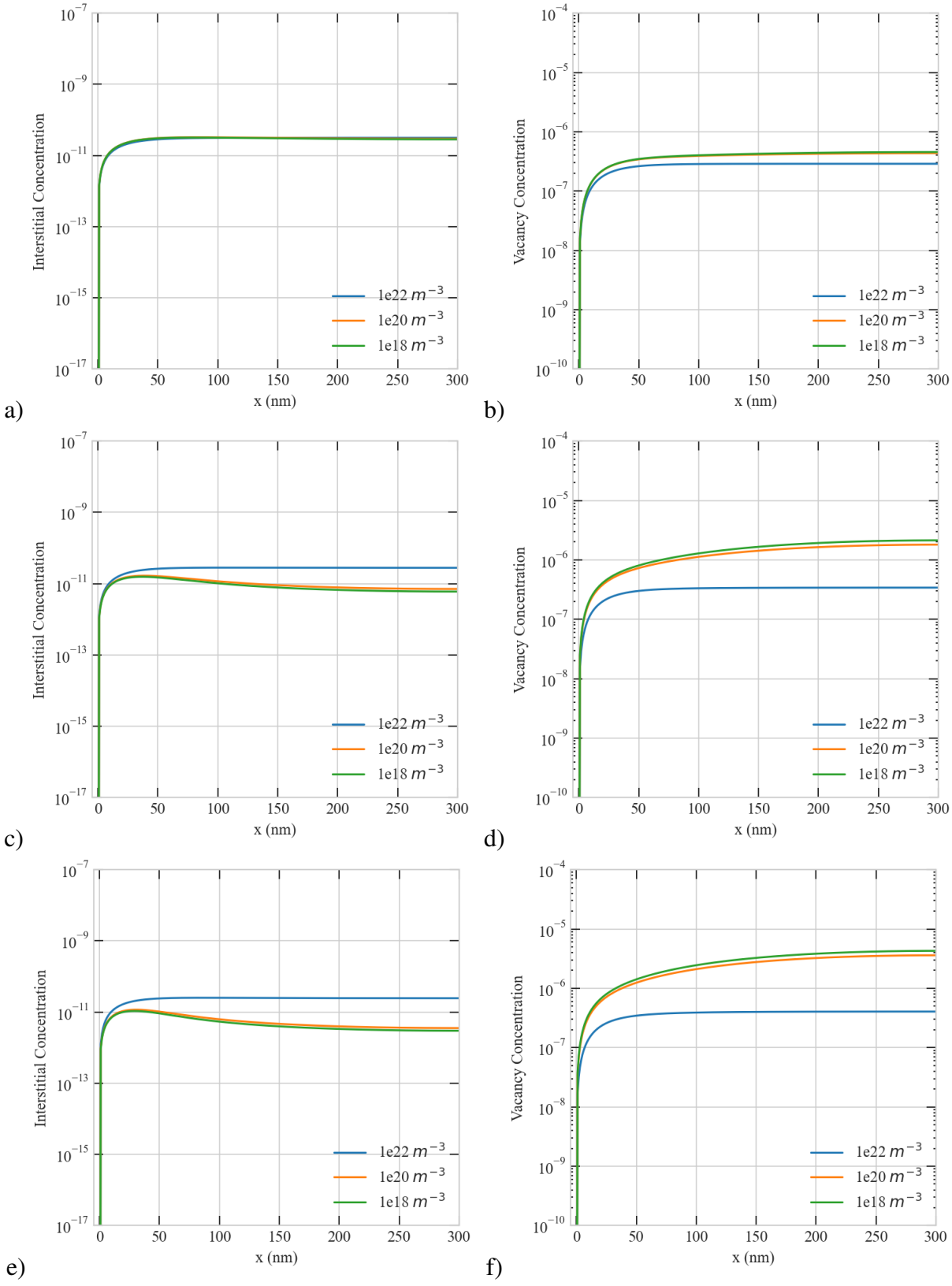

Figure 4.52: Effect of sink density on the steady-state concentration profiles of point defects in a 300 nm at 5.6e-6 dpa/s a) 1% bias, interstitial b) 1% bias, vacancy c) 10% bias, interstitial d) 10% bias, vacancy e) 20% bias, interstitial and f) 20% bias, vacancy concentrations.

Here, Fig. 4.54 shows that at the dose rate of 1e-4 dpa/s, for 1e18 and 1e20 m^{-3} sink densities instability is observed with 1% bias in 300 nm. Consequently, Cr concentration profile was also affected by this anomaly (see Fig. 4.53)

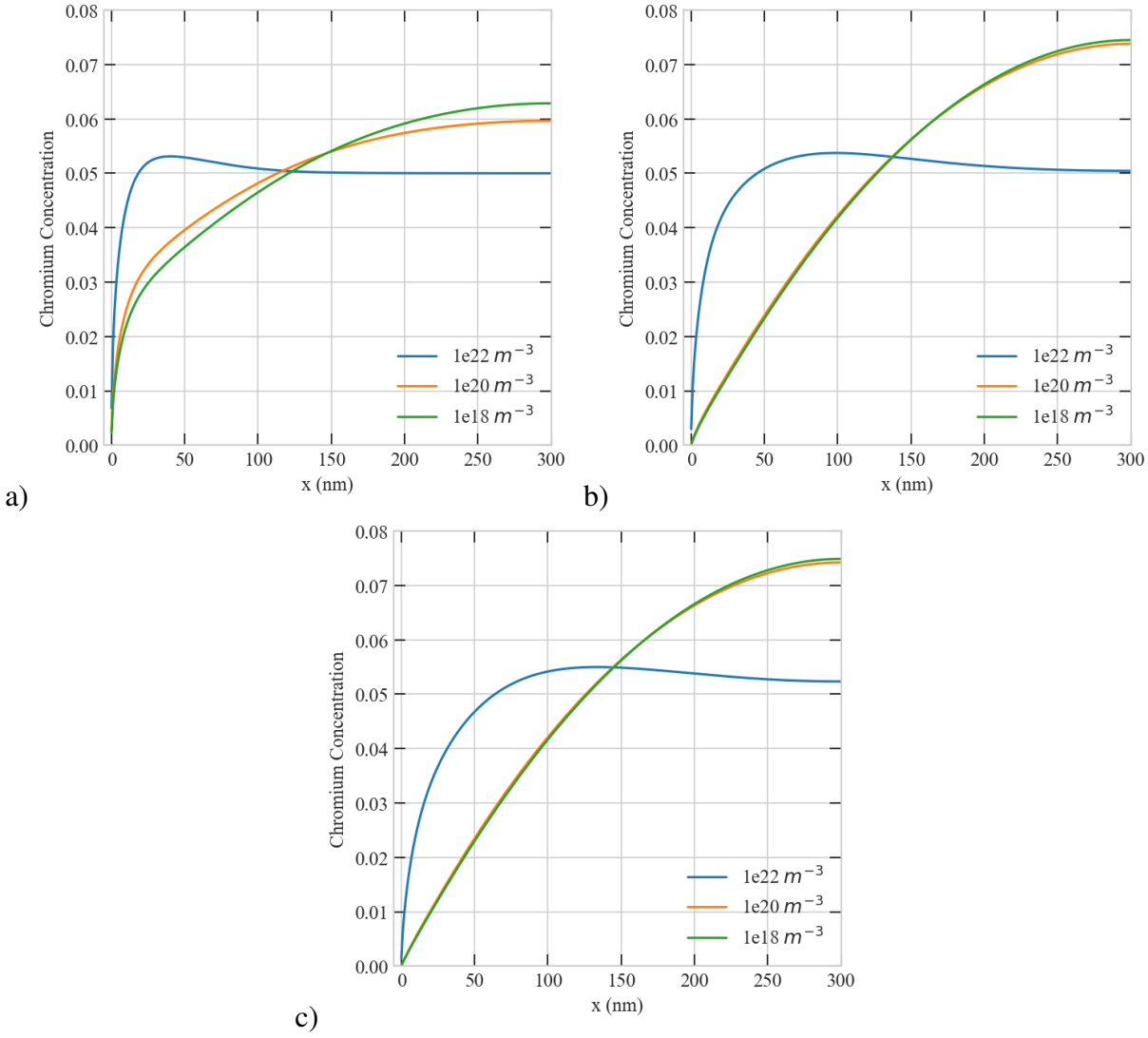

Figure 4.53: Effect of sink density on the steady-state concentration profiles of Chromium in a 300 nm at 1e-4 dpa/s a) 1% bias, Cr concentration b) 10% bias, Cr concentration c) 20% bias, Cr concentration.

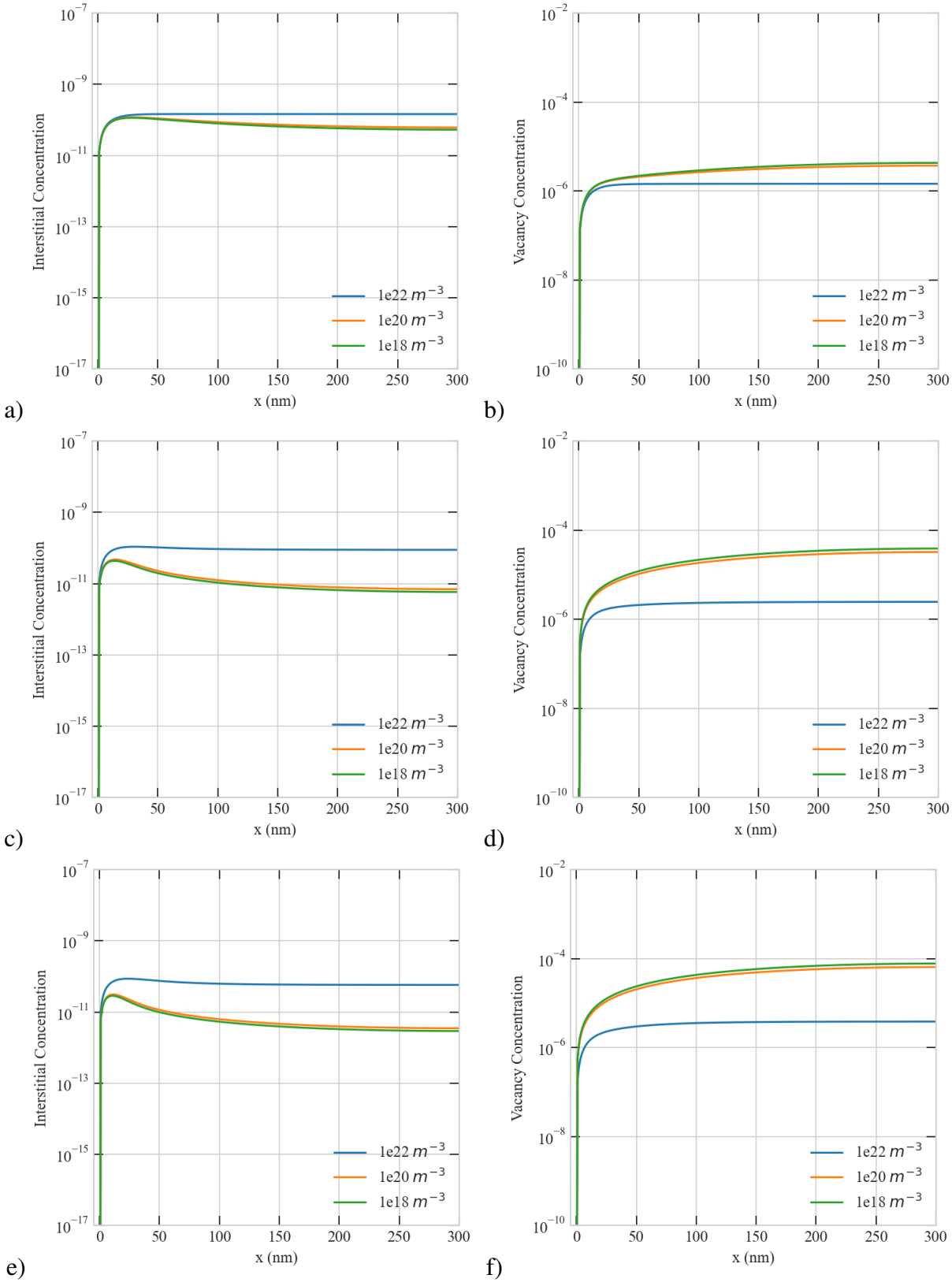

Figure 4.54: Effect of sink density on the steady-state concentration profiles of point defects in a 300 nm at 1e-4 dpa/s a) 1% bias, interstitial b) 1% bias, vacancy c) 10% bias, interstitial d) 10% bias, vacancy e) 20% bias, interstitial and f) 20% bias, vacancy concentrations.

In Fig. 4.56, changing sink density is beginning to effective on concentration of point defects at the dose rate of 5.6e-6 dpa/s in 300 nm, and effect of sink density becomes more visible with 20% bias in 300 nm. Here, the width of the depletion layer increases with bias for 1e22 m^{-3}. However, the change in the the width of the depletion layer is not significant for 1e18 and 1e20 m^{-3} sink densities in 300 nm (see Fig. 4.55).

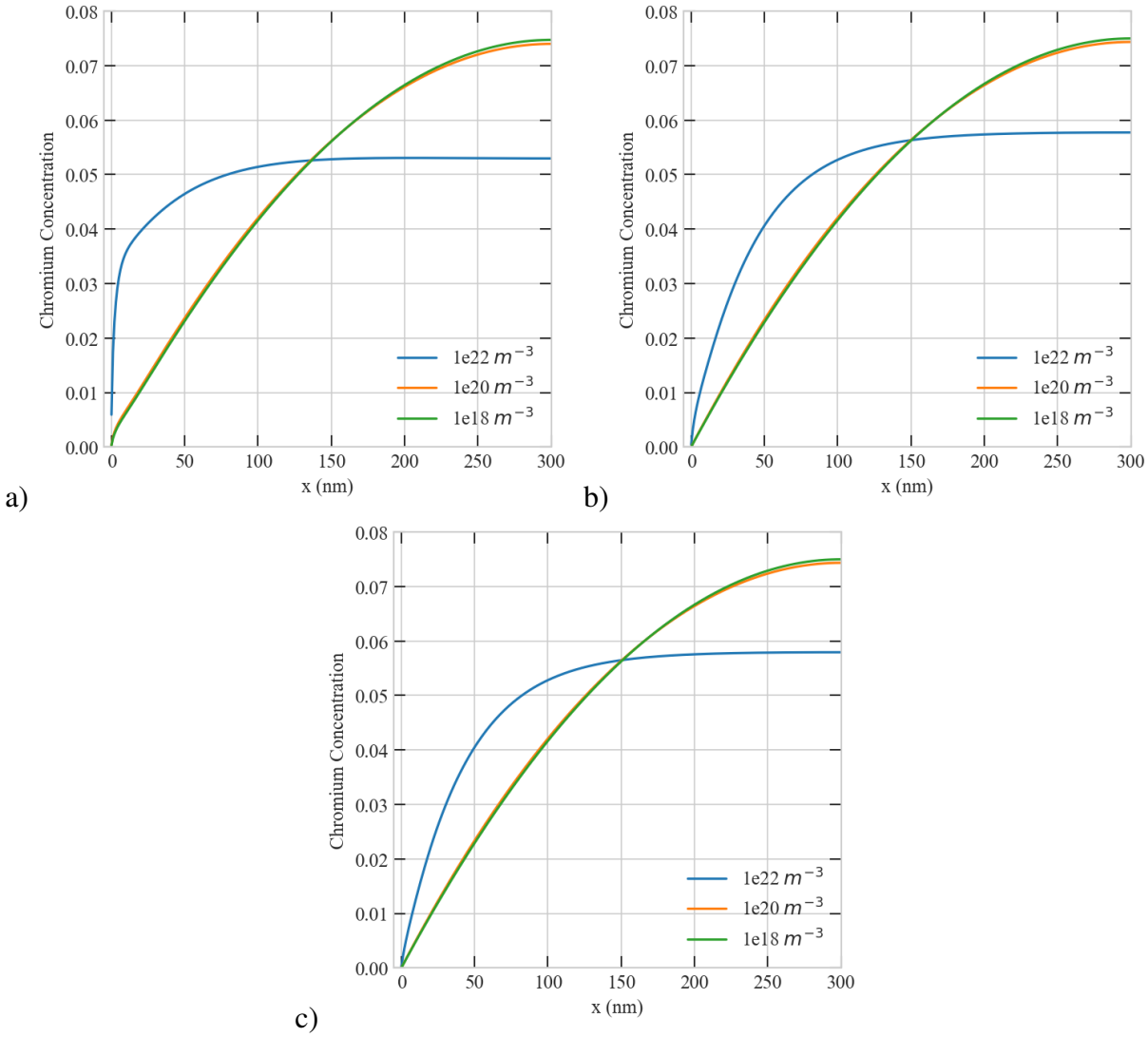

Figure 4.55: Effect of sink density on the steady-state concentration profiles of Chromium in a 300 nm at 1e-2 dpa/s a) 1% bias, Cr concentration b) 10% bias, Cr concentration c) 20% bias, Cr concentration.

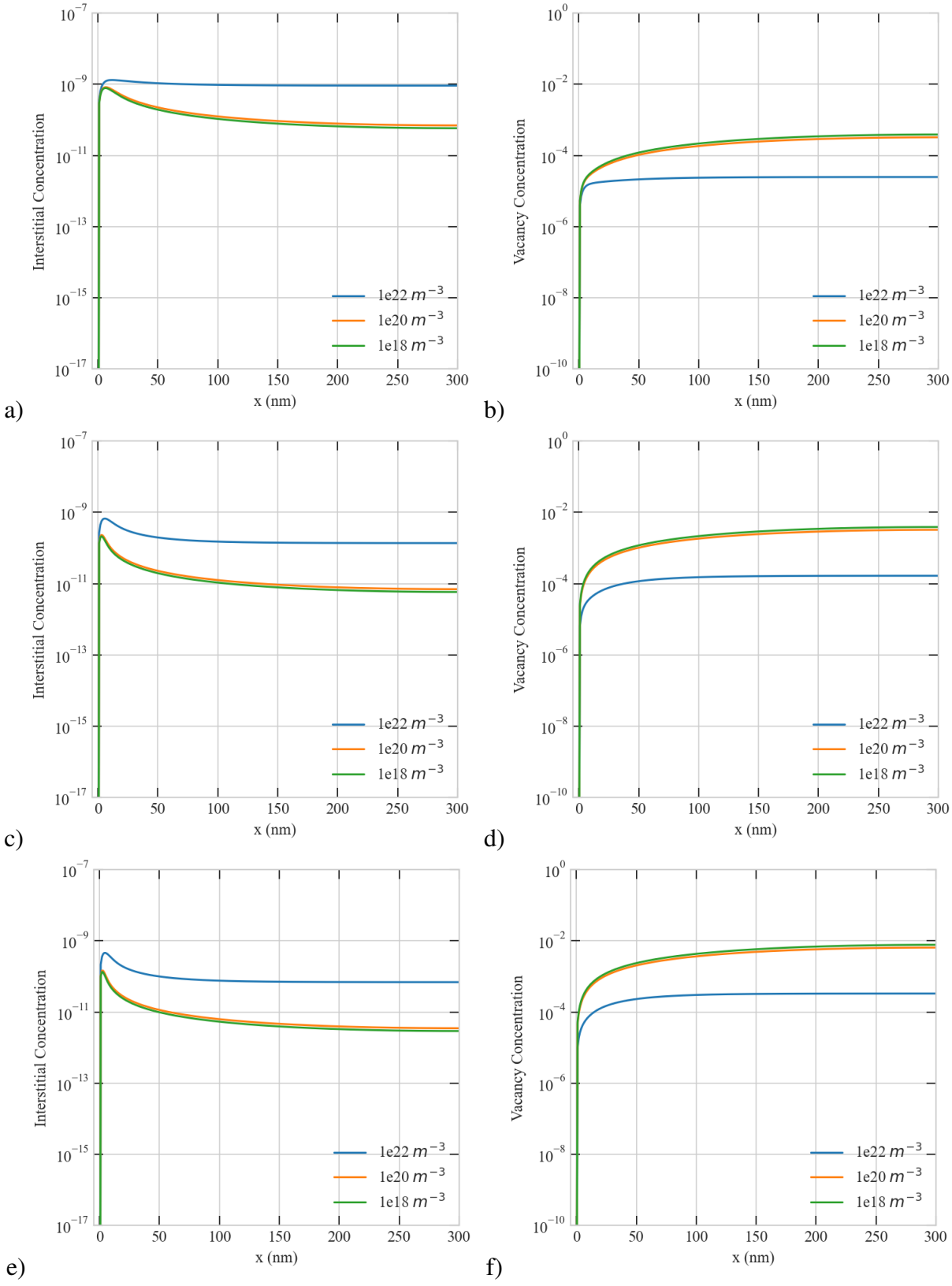

Figure 4.56: Effect of sink density on the steady-state concentration profiles of point defects in a 300 nm at 1e-2 dpa/s a) 1% bias, interstitial b) 1% bias, vacancy c) 10% bias, interstitial d) 10% bias, vacancy e) 20% bias, interstitial and f) 20% bias, vacancy concentrations.

Fig. 4.57 presents that in 500 nm, at the dose rate of 5.6e-6 dpa/s and 10% bias, the effect of difference between 1e18 and 1e20 m^{-3} sink densities has become more apparent than in 300 nm. Interstitial concentration reduce with increasing grain size and bias (see Fig. 4.57).

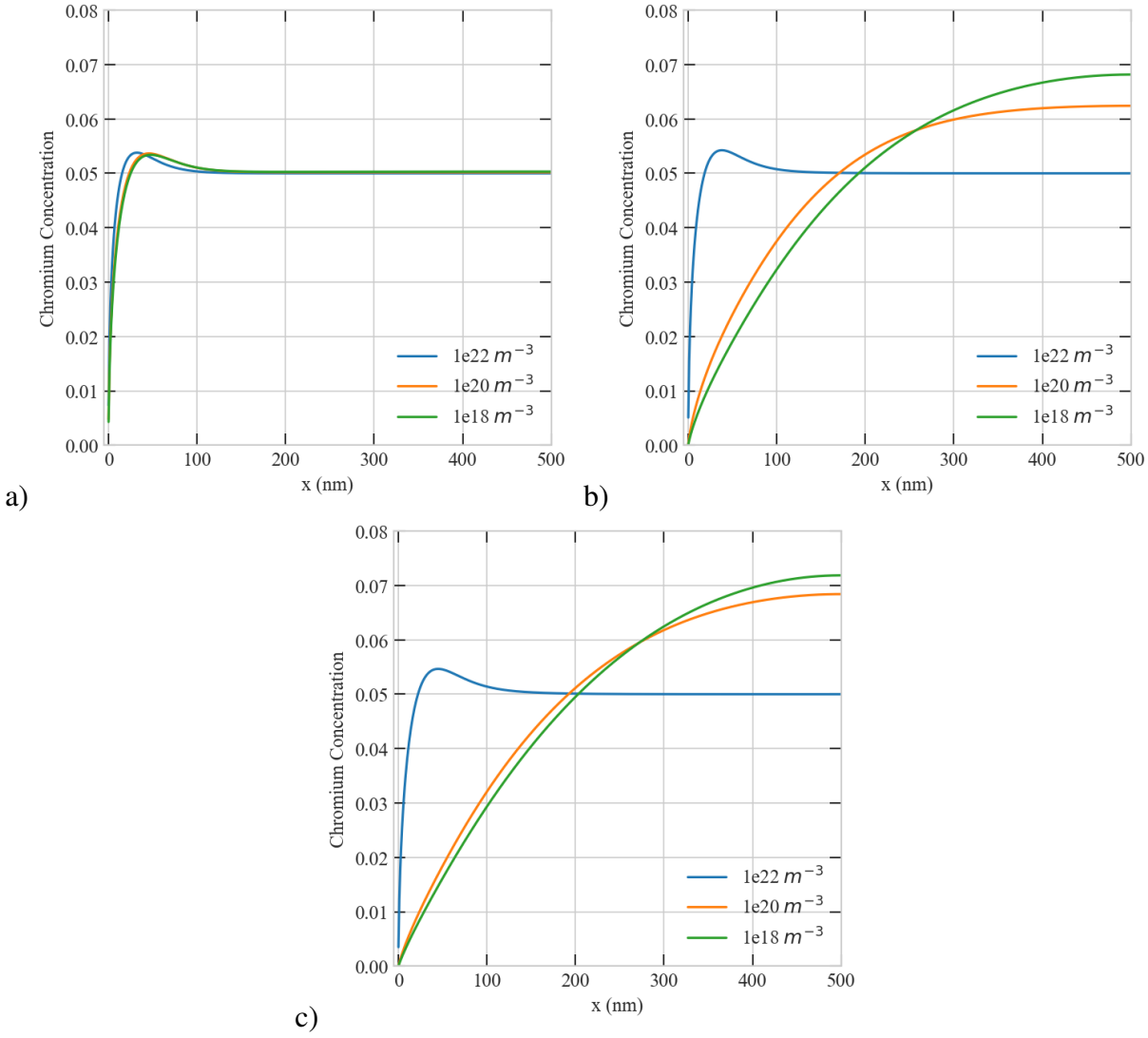

Figure 4.57: Effect of sink density on the steady-state concentration profiles of Chromium in a 500 nm at 5.6e-6 dpa/s a) 1% bias, Cr concentration b) 10% bias, Cr concentration c) 20% bias, Cr concentration.

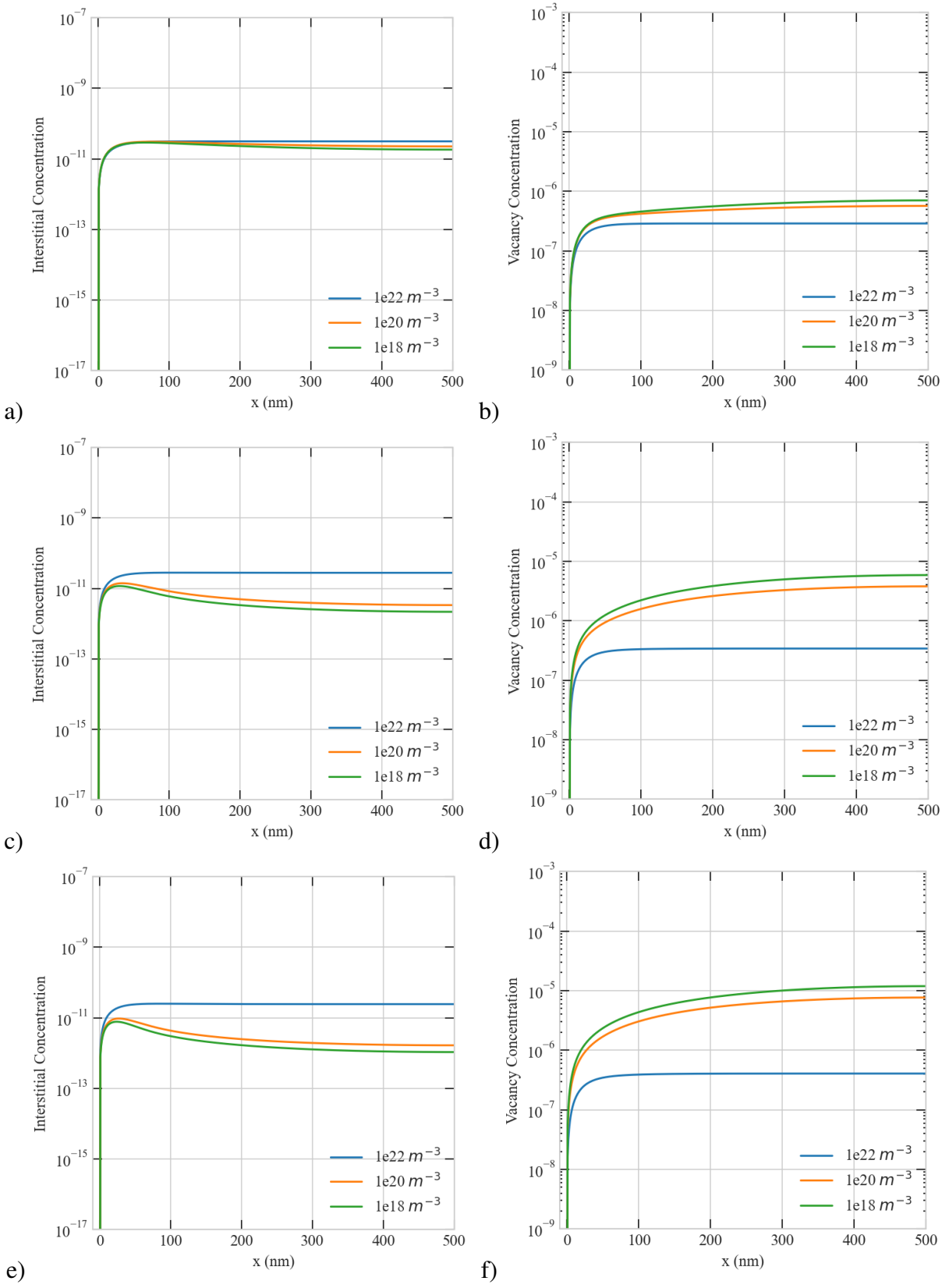

Figure 4.58: Effect of sink density on the steady-state concentration profiles of point defects in a 500 nm at 5.6e-6 dpa/s a) 1% bias, interstitial b) 1% bias, vacancy c) 10% bias, interstitial d) 10% bias, vacancy e) 20% bias, interstitial and f) 20% bias, vacancy concentrations.

Fig. 4.60 displays that the vacancy concentration gradients in the vicinity of the boundary increases with bias. At the dose rate of 1e-4 dpa/s, the effect of bias on Cr concentration profile does not vary significantly for 1e18 and 1e20 m^{-3} sink densities. However, for 1e22 m^{-3}, Cr concentration in the vicinity of the boundary decreases with increased production bias (see Fig. 4.59).

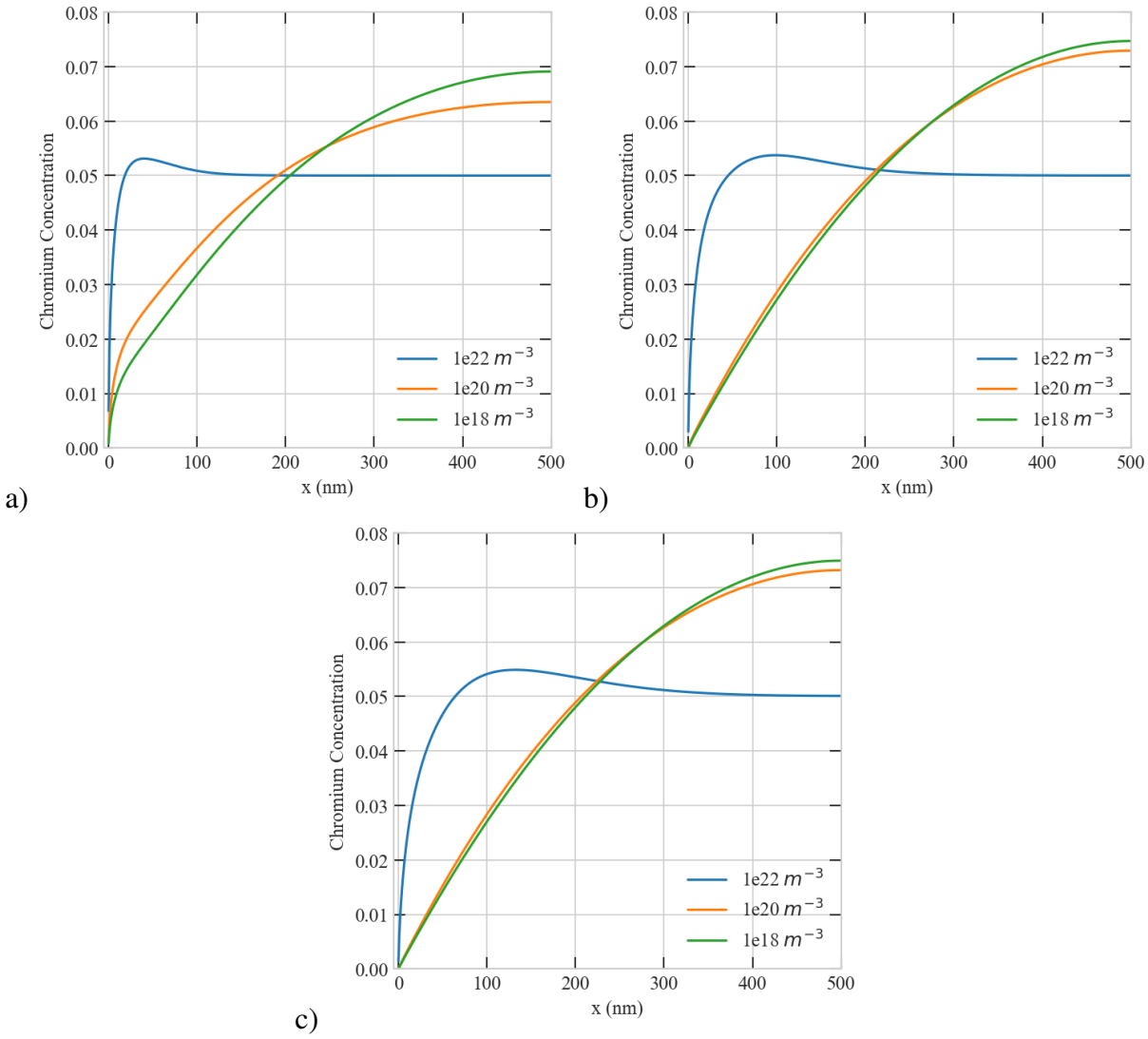

Figure 4.59: Effect of sink density on the steady-state concentration profiles of Chromium in a 500 nm at 1e-4 dpa/s a) 1% bias, Cr concentration b) 10% bias, Cr concentration c) 20% bias, Cr concentration.

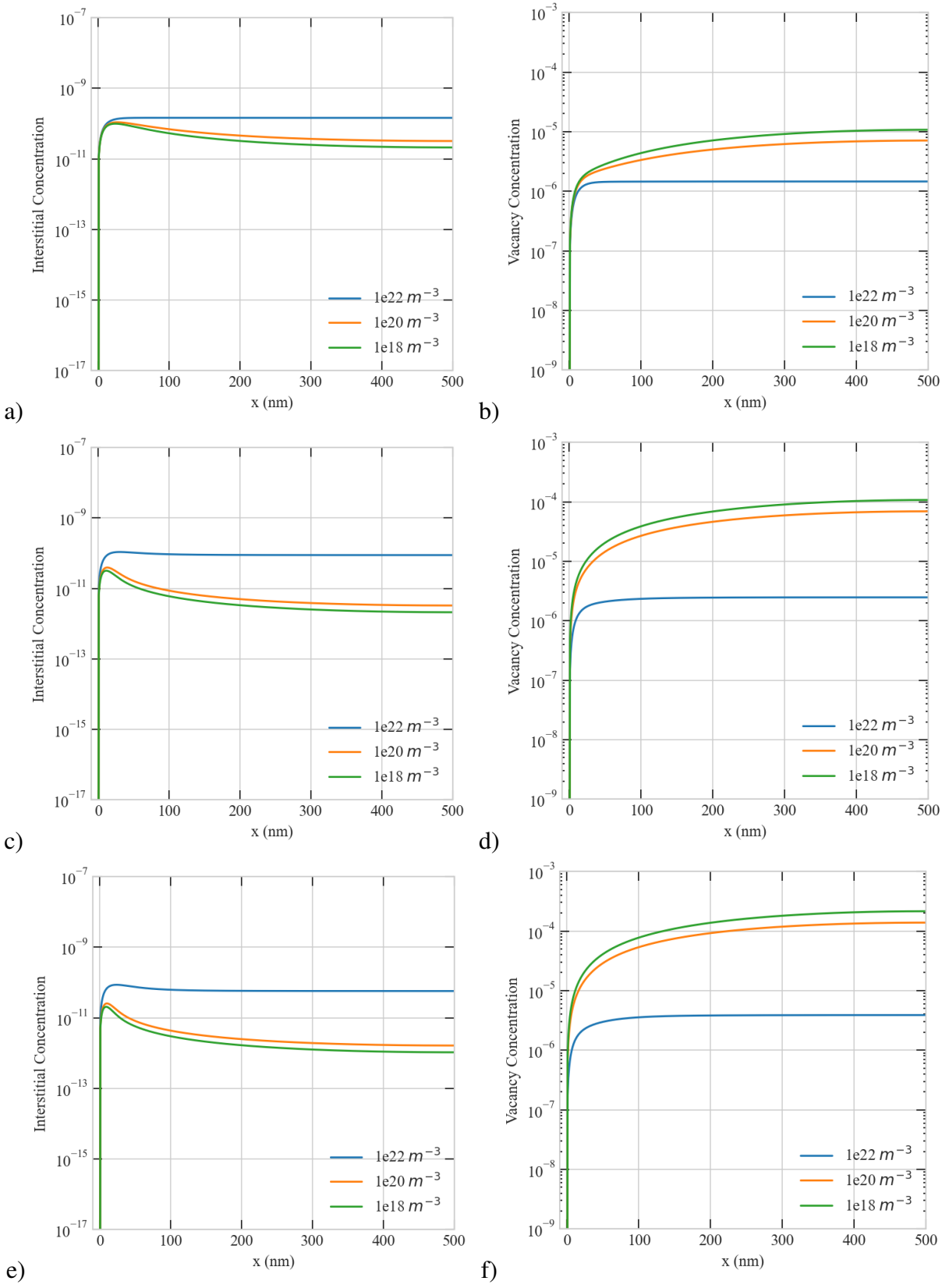

Figure 4.60: Effect of sink density on the steady-state concentration profiles of point defects in a 500 nm at 1e-4 dpa/s a) 1% bias, interstitial b) 1% bias, vacancy c) 10% bias, interstitial d) 10% bias, vacancy e) 20% bias, interstitial and f) 20% bias, vacancy concentrations.

In Fig. 4.62, for three sink densities, vacancy and interstitial concentrations follow similar trend with 10% and 20% biases in 500 nm. Therefore, at the highest dose rate of 1e-2 dpa/s, Cr concentration profile remains similar for 1e18 and 1e20 m^{-3} sink densities (see Fig. 4.61).

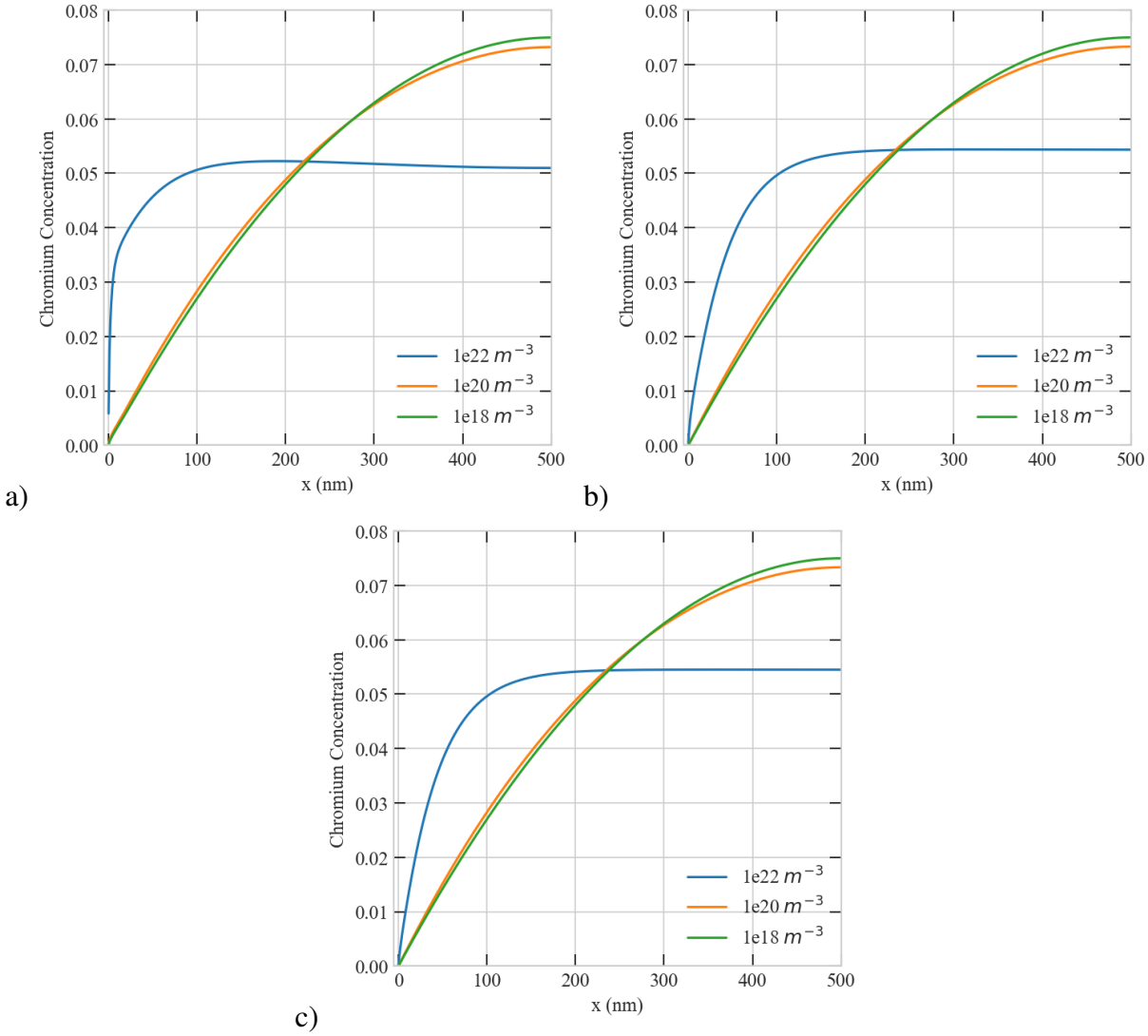

Figure 4.61: Effect of sink density on the steady-state concentration profiles of Chromium in a 500 nm at 1e-2 dpa/s a) 1% bias, Cr concentration b) 10% bias, Cr concentration c) 20% bias, Cr concentration.

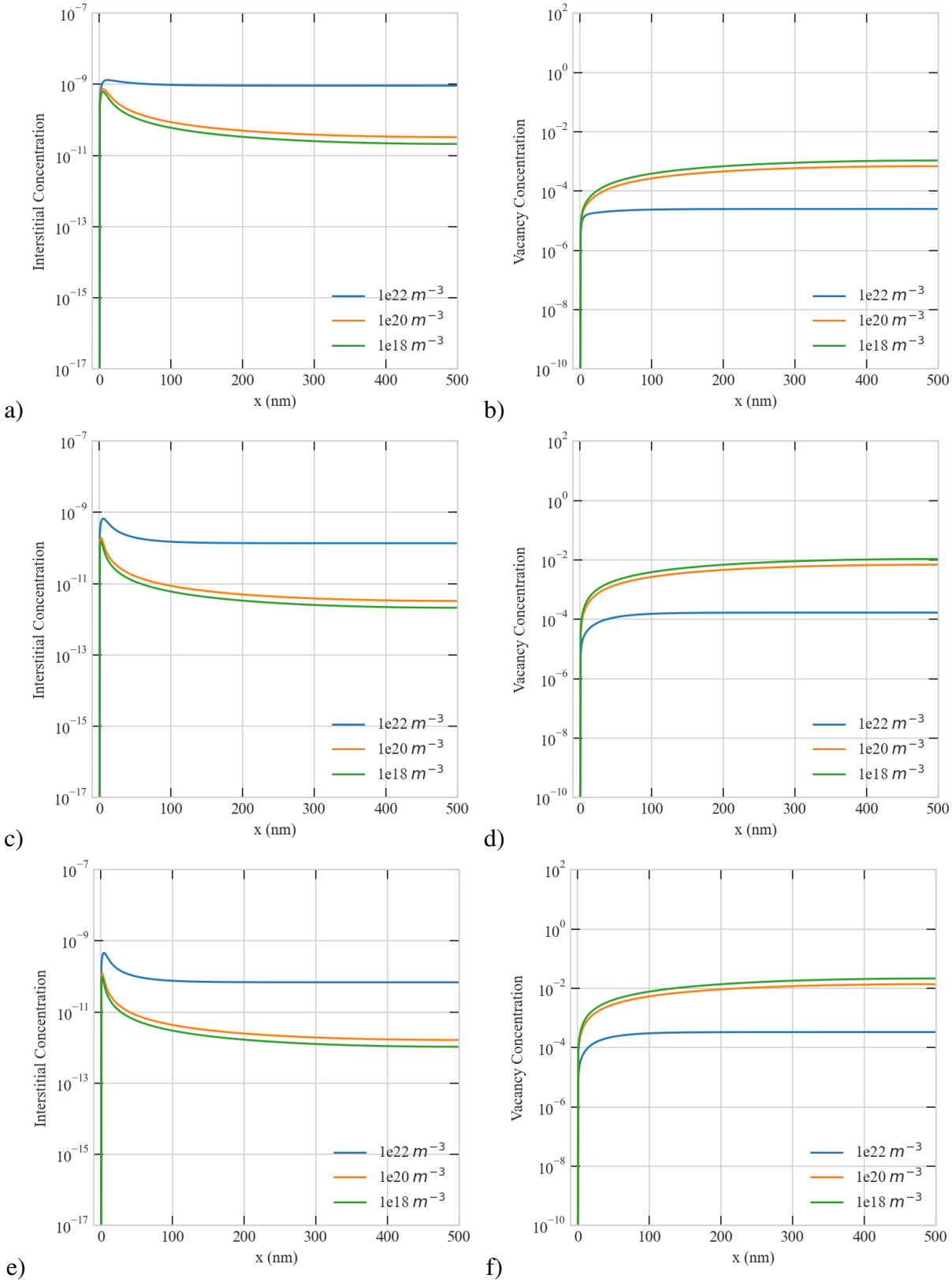

Figure 4.62: Effect of sink density on the steady-state concentration profiles of point defects in a 500 nm at 1e-2 dpa/s a) 1% bias, interstitial b) 1% bias, vacancy c) 10% bias, interstitial d) 10% bias, vacancy e) 20% bias, interstitial and f) 20% bias, vacancy concentrations.

In Fig. 4.61, while the sink density effect is still in-explicit in 500 nm at the dose rate of 1e-2 dpa/s, the effect of sink density on the concentration of point defects becomes apparent in 5000 nm at the dose rate of 5.6e-6 dpa/s (see Fig. 4.63). This effect becomes more obvious when we examine 5000 nm size at the dose rate of 1e-4 dpa/s with 10% and 20% bias (see Fig. 4.65).

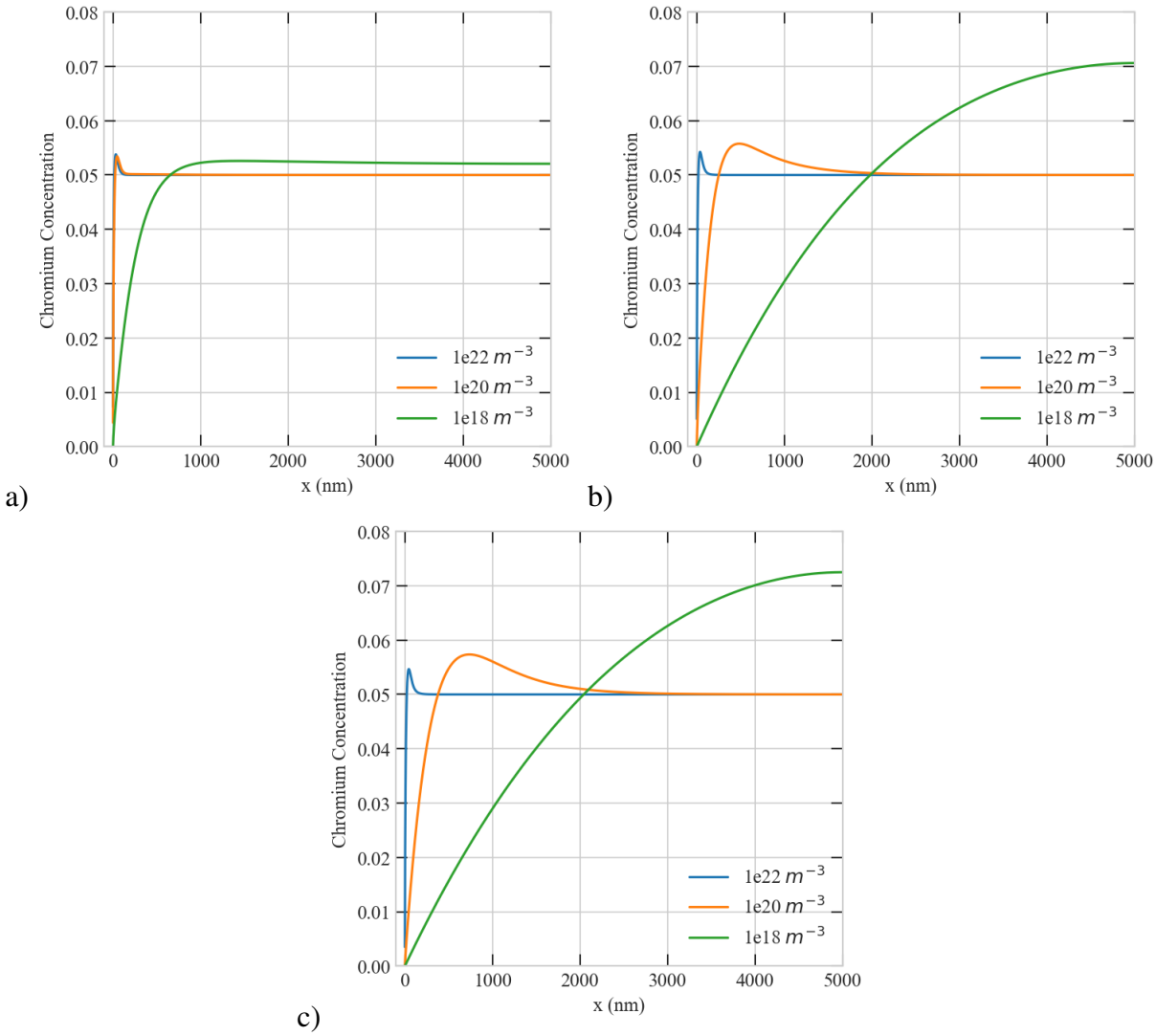

Figure 4.63: Effect of sink density on the steady-state concentration profiles of Chromium in a 5000 nm at 5.6e-6 dpa/s a) 1% bias, Cr concentration b) 10% bias, Cr concentration c) 20% bias, Cr concentration.

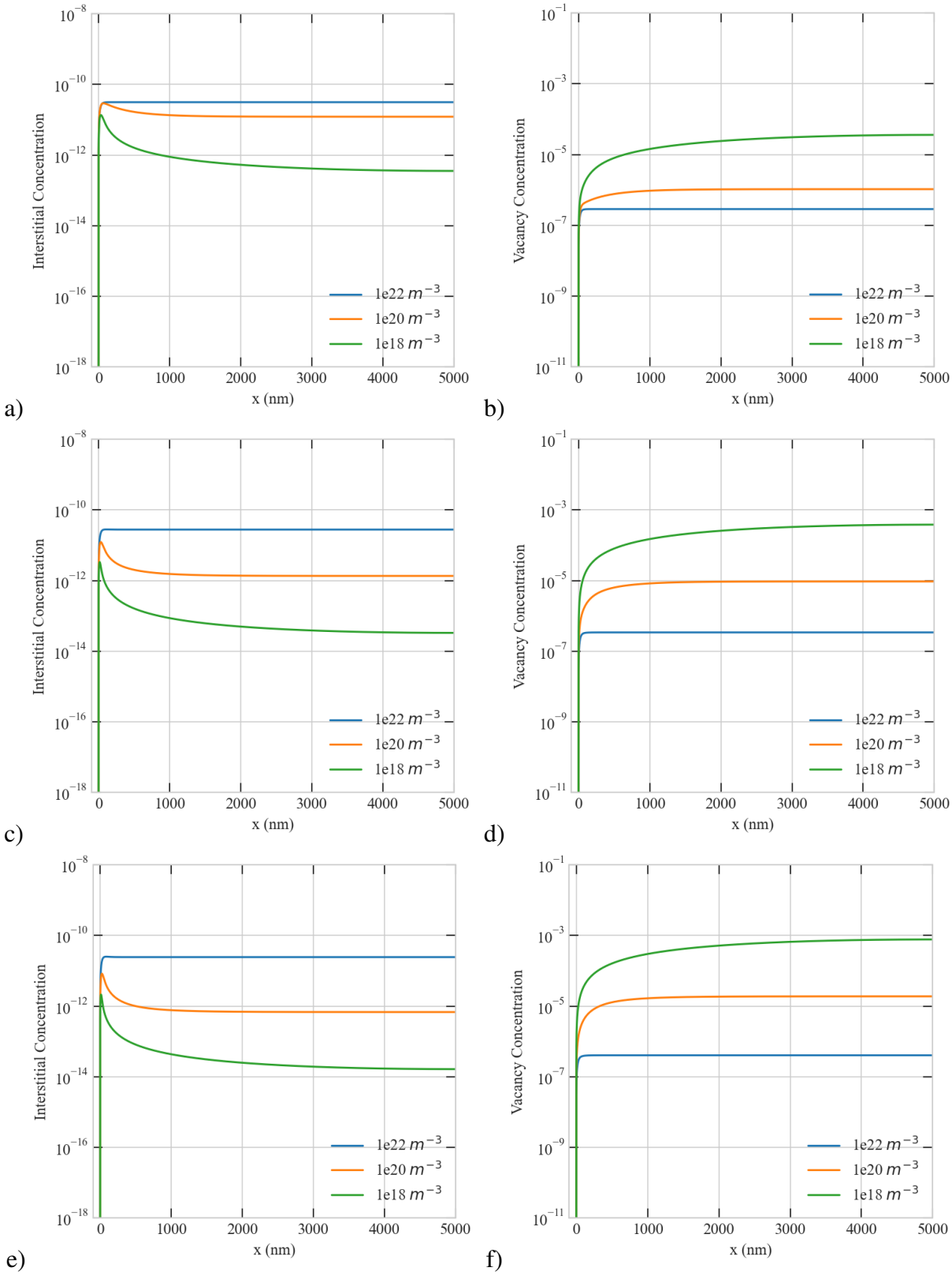

Figure 4.64: Effect of sink density on the steady-state concentration profiles of point defects in a 5000 nm at 5.6e-6 dpa/s a) 1% bias, interstitial b) 1% bias, vacancy c) 10% bias, interstitial d) 10% bias, vacancy e) 20% bias, interstitial and f) 20% bias, vacancy concentrations.

For 1e22 m^{-3} sink density, interstitial concentration does not significantly decrease near the boundary in 5000 nm with increased production bias (see Fig. 4.66). Therefore, accumulation in Cr concentration in the vicinity of the boundary becomes more apparent, as seen in at 773 K. On the other hand, for 1e18 m^{-3} sink density, Cr concentration profile was not distinctly affected by the rise in production bias (see Fig. 4.65).

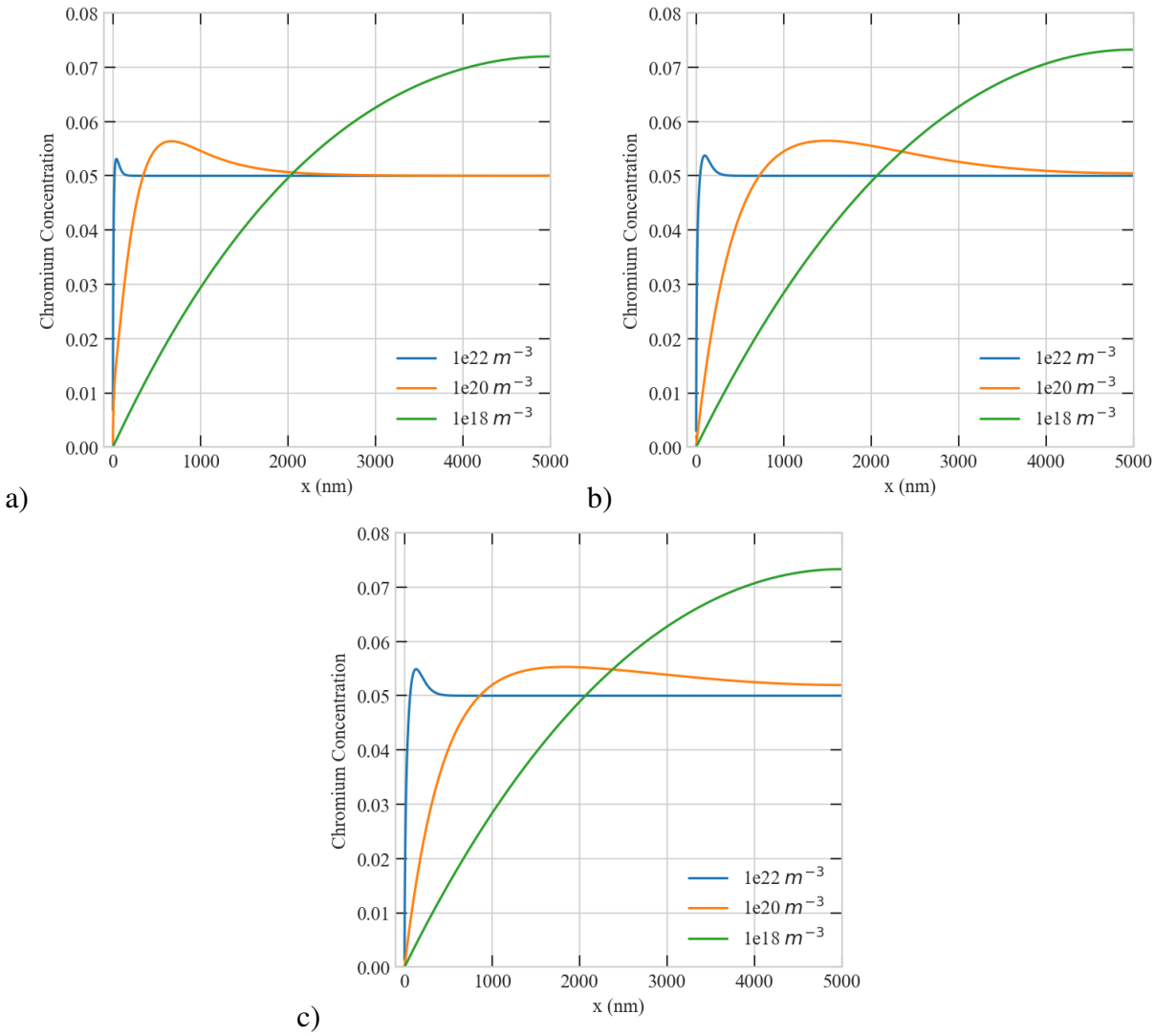

Figure 4.65: Effect of sink density on the steady-state concentration profiles of Chromium in a 5000 nm at 1e-4 dpa/s a) 1% bias, Cr concentration b) 10% bias, Cr concentration c) 20% bias, Cr concentration.

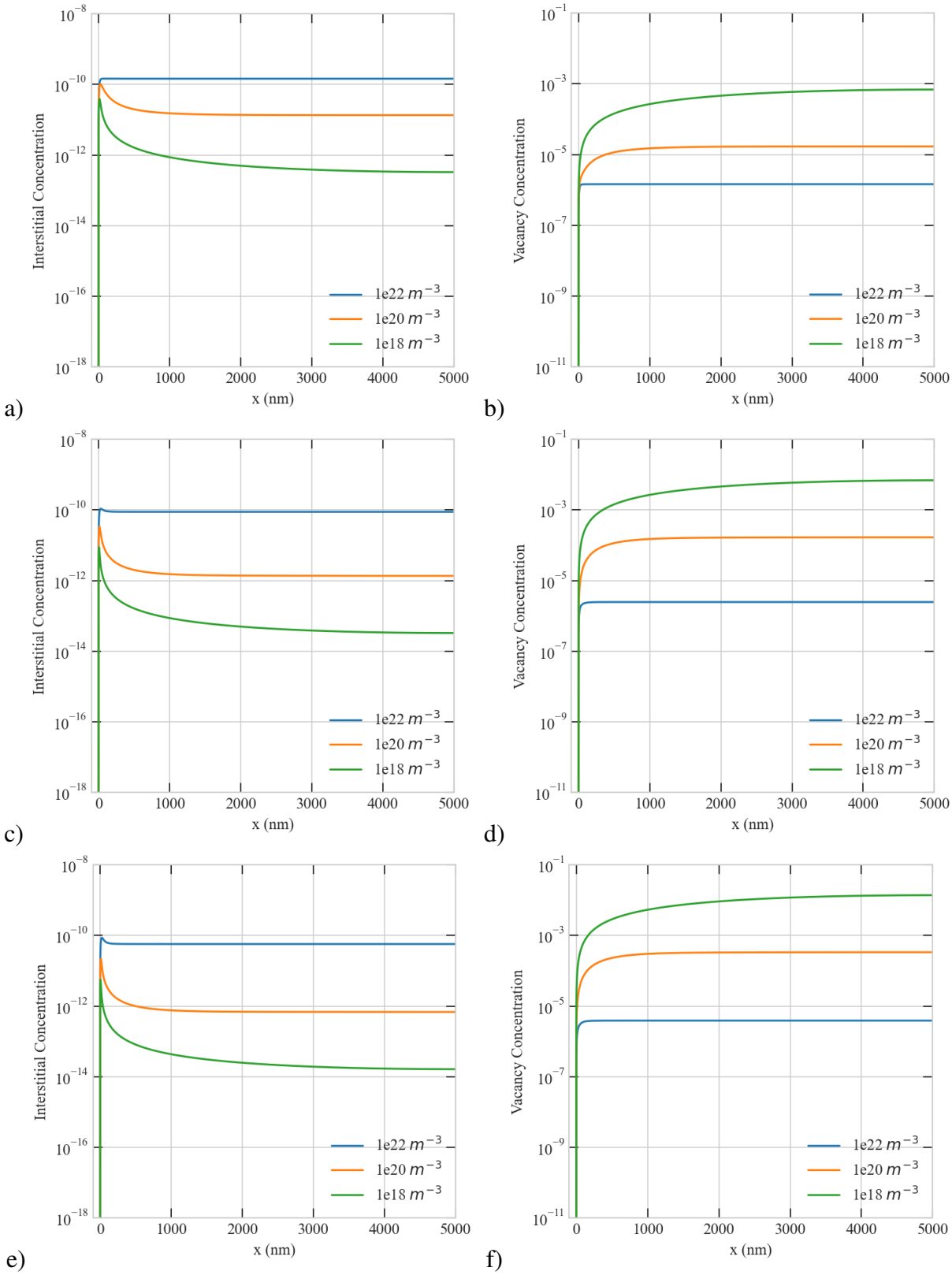

Figure 4.66: Effect of sink density on the steady-state concentration profiles of point defects in a 5000 nm at 1e-4 dpa/s a) 1% bias, interstitial b) 1% bias, vacancy c) 10% bias, interstitial d) 10% bias, vacancy e) 20% bias, interstitial and f) 20% bias, vacancy concentrations.

For 1e22 m^{-3} sink density, we did not observe accumulation in interstitial concentration near the boundary at the dose rate of 5.6e-6 dpa/s in 7500 nm (see Fig. 4.68). However, accumulation in interstitial concentration can be seen with the increase in bias for 1e20 m^{-3} sink density. Thus, Cr depletion layer is widened (see Fig. 4.67).The anomaly in the dependence of interstitial accumulation results in Cr depletion at the boundary. Besides, it becomes more evident with the increase in production bias in 7500 nm.

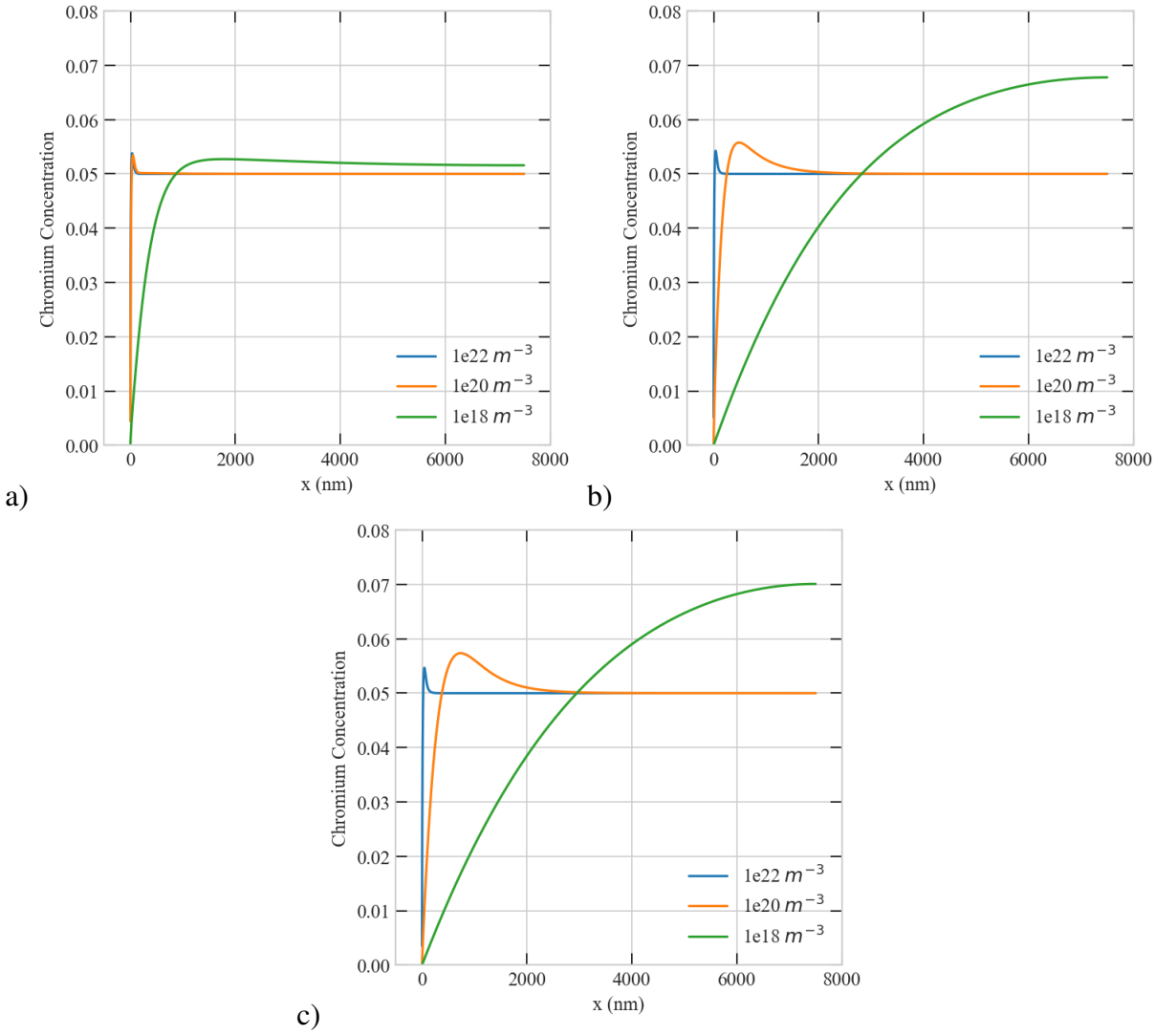

Figure 4.67: Effect of sink density on the steady-state concentration profiles of Chromium in a 7500 nm at 5.6e-6 dpa/s a) 1% bias, Cr concentration b) 10% bias, Cr concentration c) 20% bias, Cr concentration.

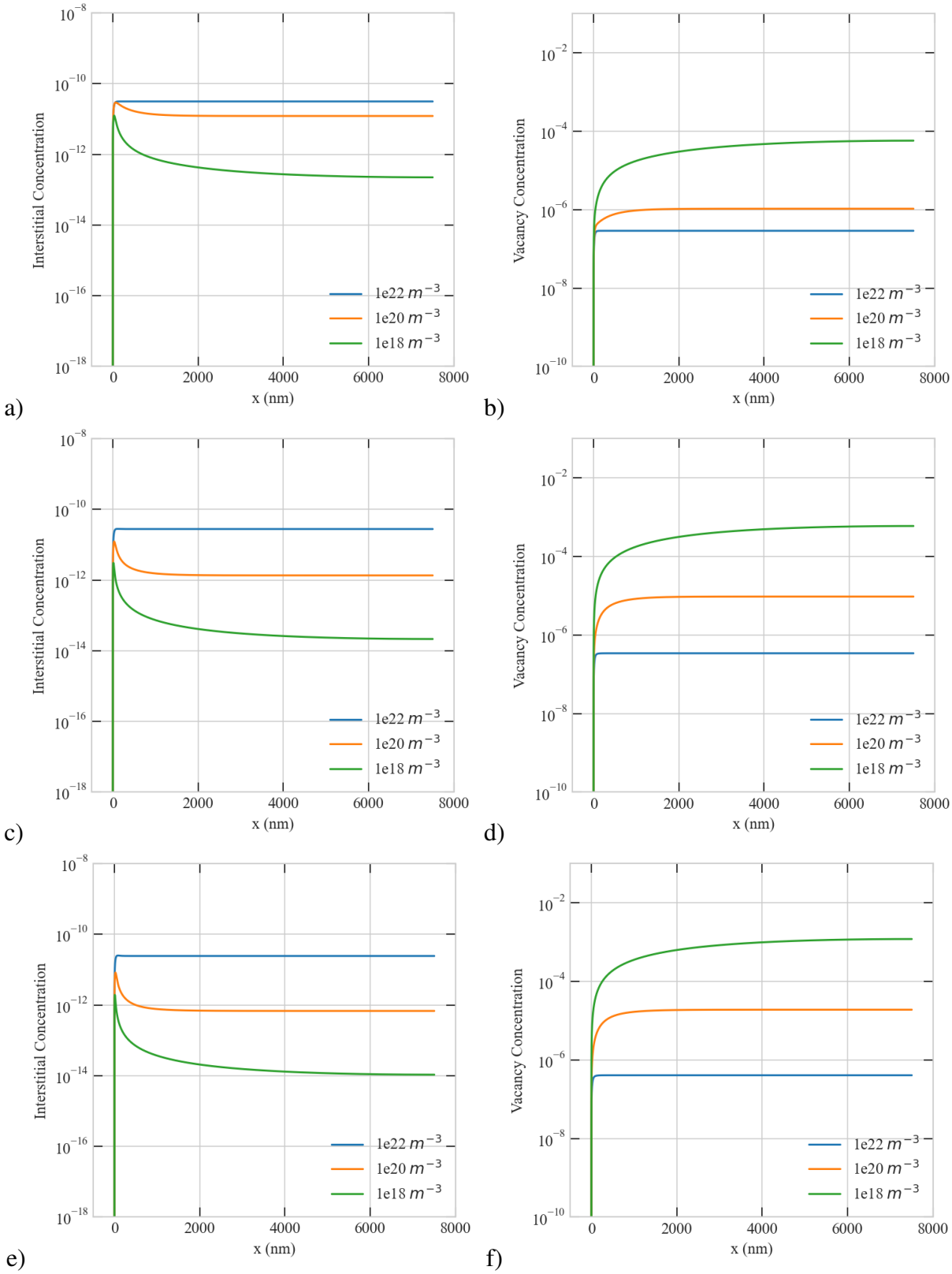

Figure 4.68: Effect of sink density on the steady-state concentration profiles of point defects in a 7500 nm at 5.6e-6 dpa/s a) 1% bias, interstitial b) 1% bias, vacancy c) 10% bias, interstitial d) 10% bias, vacancy e) 20% bias, interstitial and f) 20% bias, vacancy concentrations.

Increase in dose rate and bias, for 1e22 m^{-3} sink density, cause small accumulation in interstitial concentration near the boundary. This small accumulation have a slight effect on the Cr concentration profile at the dose rate of 1e-4 dpa/s in 7500 nm (see Fig. 4.69 and Fig. 4.70).

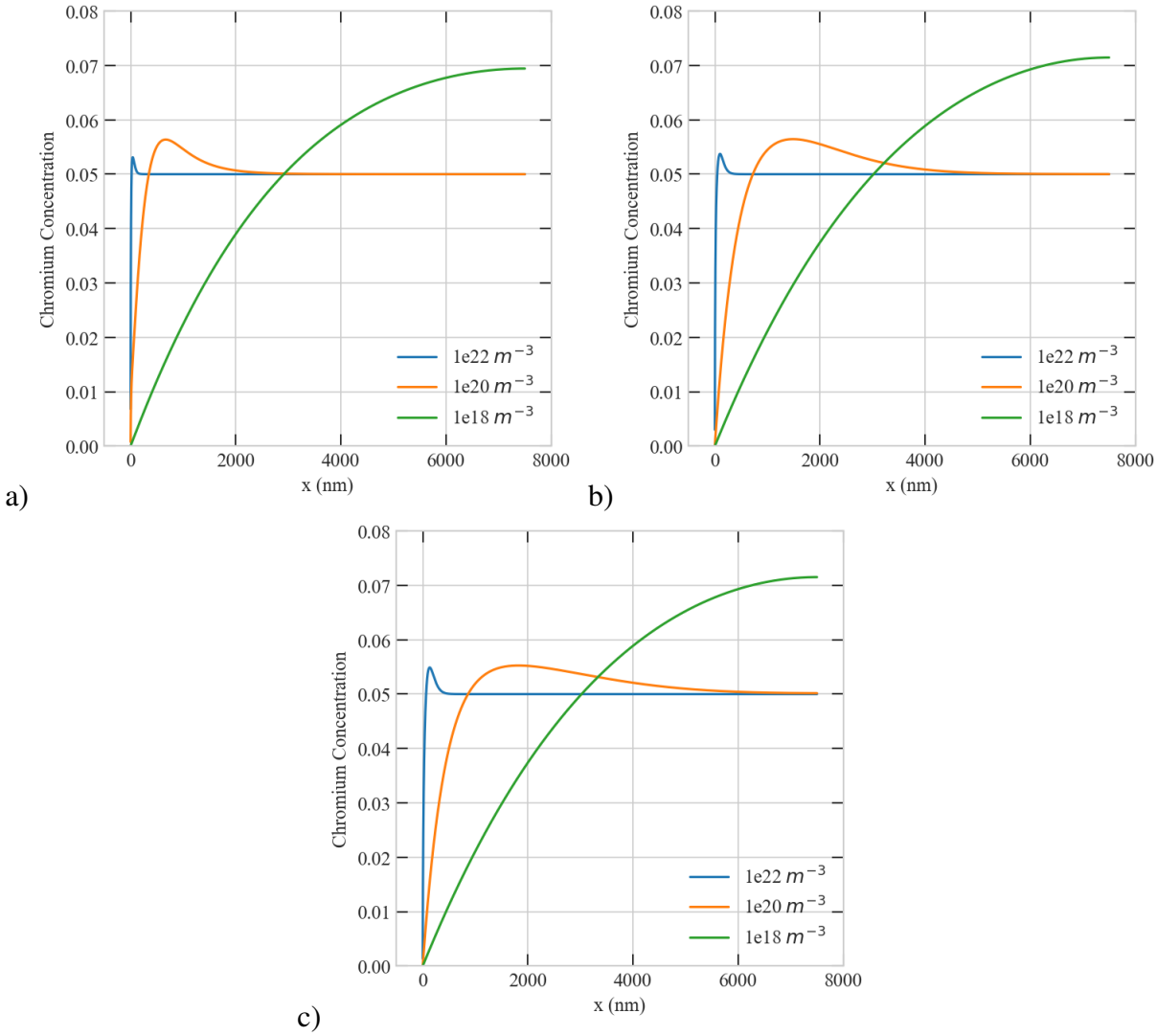

Figure 4.69: Effect of sink density on the steady-state concentration profiles of Chromium in a 7500 nm at 1e-4 dpa/s a) 1% bias, Cr concentration b) 10% bias, Cr concentration c) 20% bias, Cr concentration.

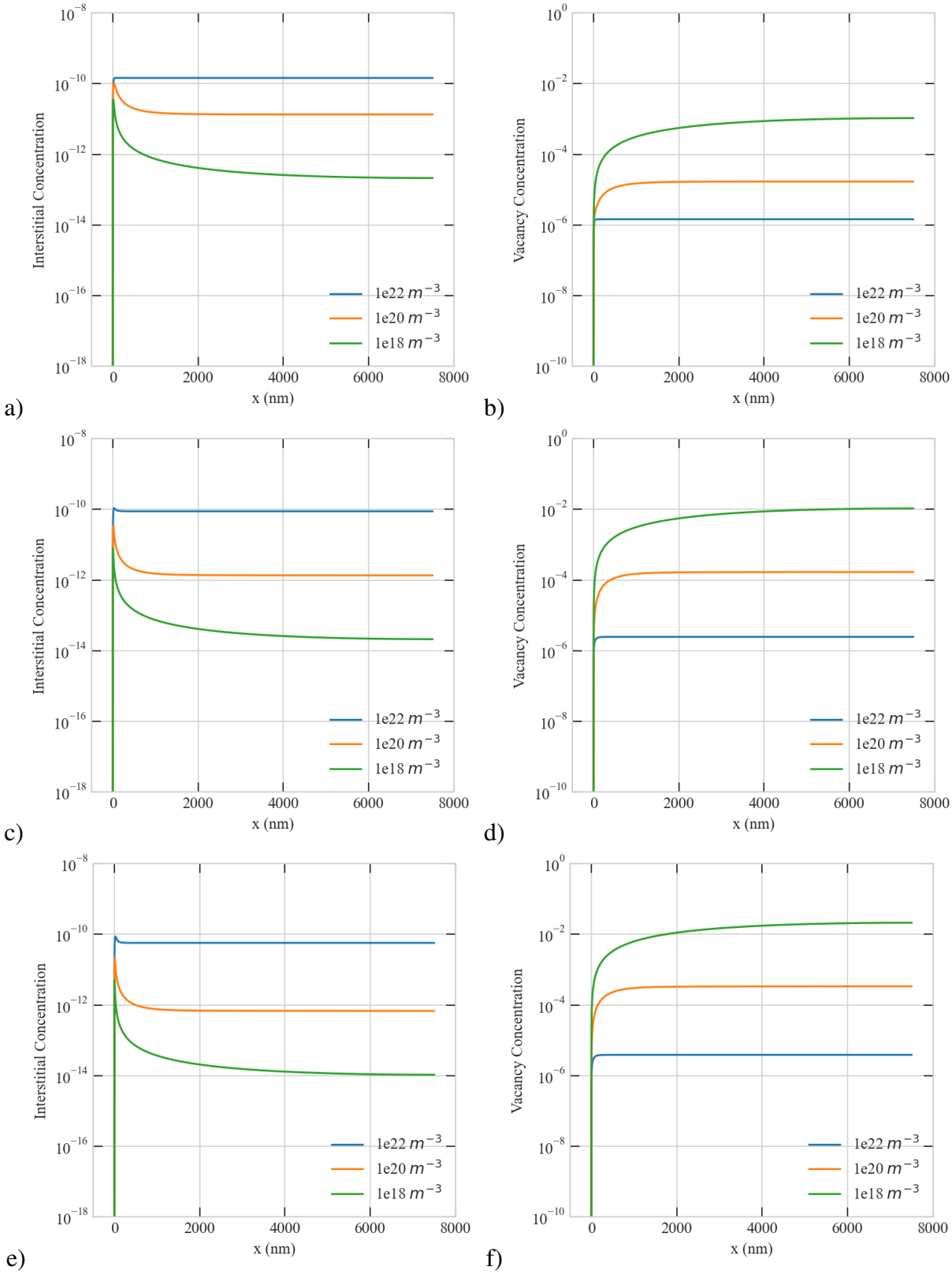

Figure 4.70: Effect of sink density on the steady-state concentration profiles of point defects in a 7500 nm at 1e-4 dpa/s a) 1% bias, interstitial b) 1% bias, vacancy c) 10% bias, interstitial d) 10% bias, vacancy e) 20% bias, interstitial and f) 20% bias, vacancy concentrations.

4.5.3 The Combined Effects of Microstructure and Irradiation Parameters at 473K

In Fig. 4.71 shows that Cr depletion has become more severe for all sink density cases even at the low dose rate of 5.6e-6 dpa/s and 473 K. The most likely explanation for that perfect sink assumption. In this study, we assumed that boundary/surface behaves as a perfect defect sink. In other words, defect sink sustains equilibrium defect concentrations near the boundary. Our assumption works reasonably well with experimental data at 773 K since the sink shows ideal sink behavior at higher temperatures [58]. However, for lower temperatures, 473 K and 573 K, RIS is suppressed concerning the perfect defect sink approach [47]. Thus, a perfect defect sink approach may play an important role on the Cr depletion.

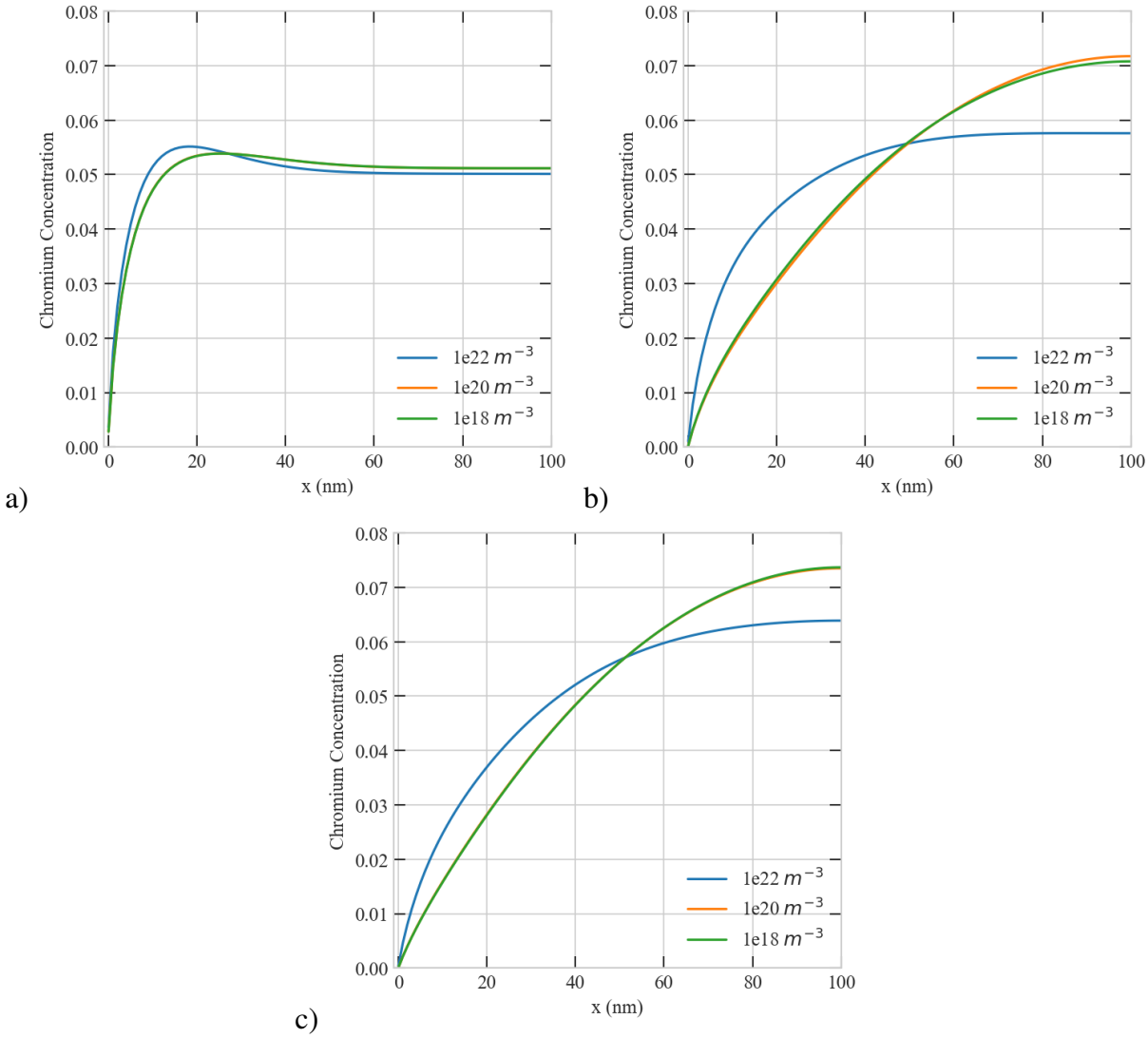

Figure 4.71: Effect of sink density on the steady-state concentration profiles of Chromium in a 100 nm at 5.6e-6 dpa/s a) 1% bias, Cr concentration b) 10% bias, Cr concentration c) 20% bias, Cr concentration.

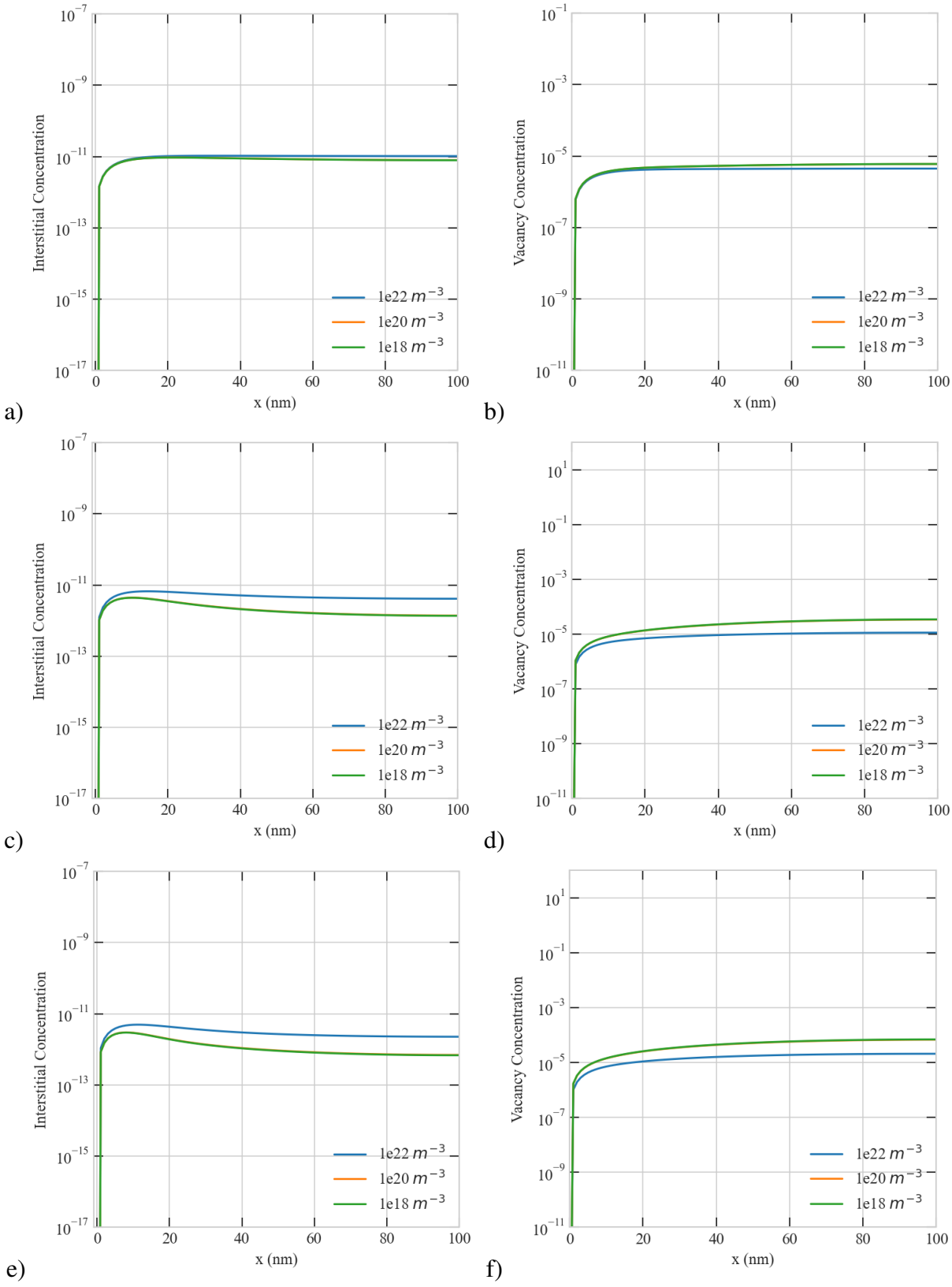

Figure 4.72: Effect of sink density on the steady-state concentration profiles of point defects in a 100 nm at 5.6e-6 dpa/s a) 1% bias, interstitial b) 1% bias, vacancy c) 10% bias, interstitial d) 10% bias, vacancy e) 20% bias, interstitial and f) 20% bias, vacancy concentrations.

Here, it is important to take account of the anomaly in the dependence of interstitial accumulation. While this instability on point defects is not observed at 573 K in 100 nm, it begins to be become more noticeable for 1e-4 dpa/s with 20% bias in 100 nm at 473 K (see Fig. 4.74). This strengthens the argument that instability renders irradiation damage more pronounced.

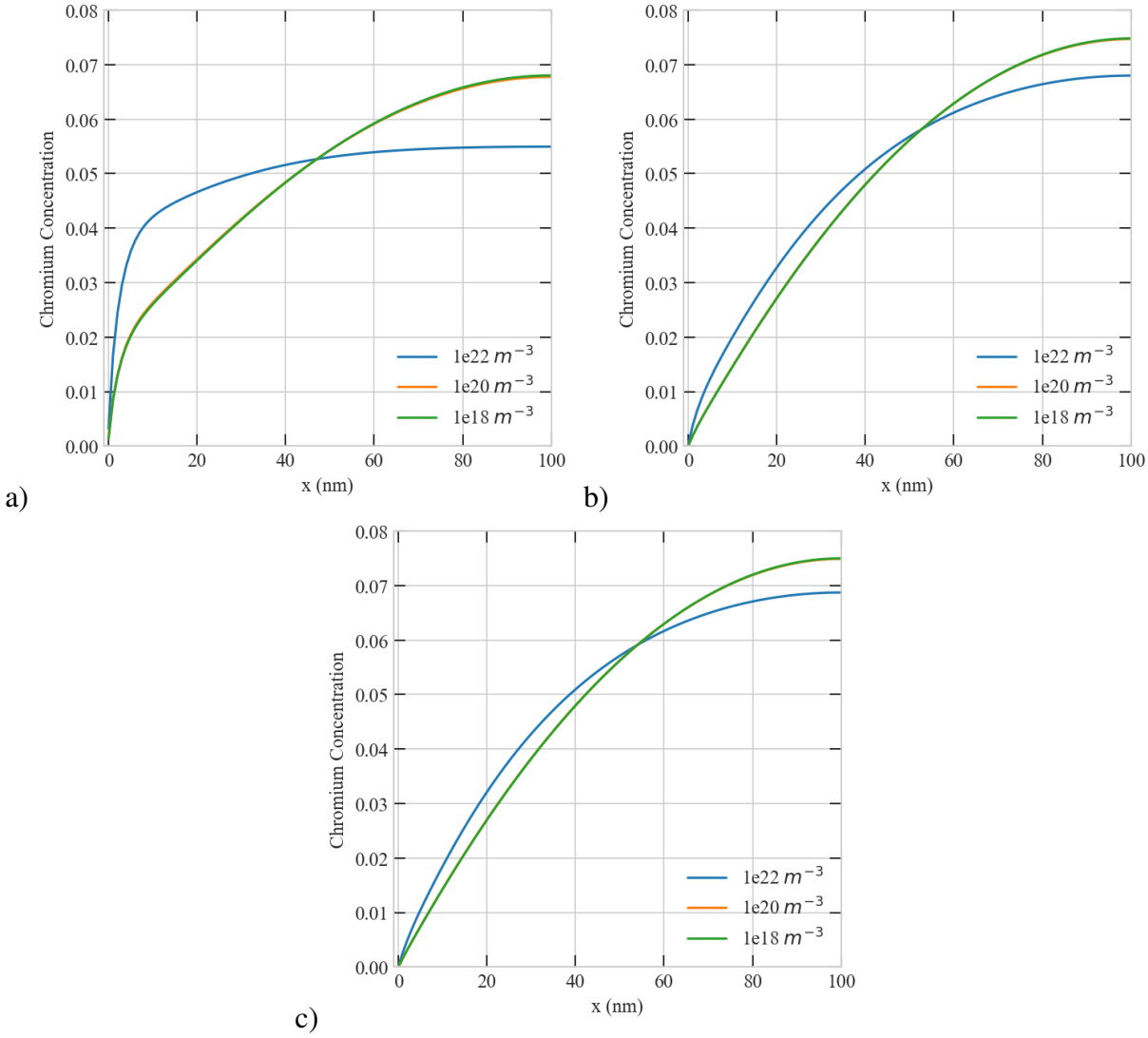

Figure 4.73: Effect of sink density on the steady-state concentration profiles of Chromium in a 100 nm at 1e-4 dpa/s a) 1% bias, Cr concentration b) 10% bias, Cr concentration c) 20% bias, Cr concentration.

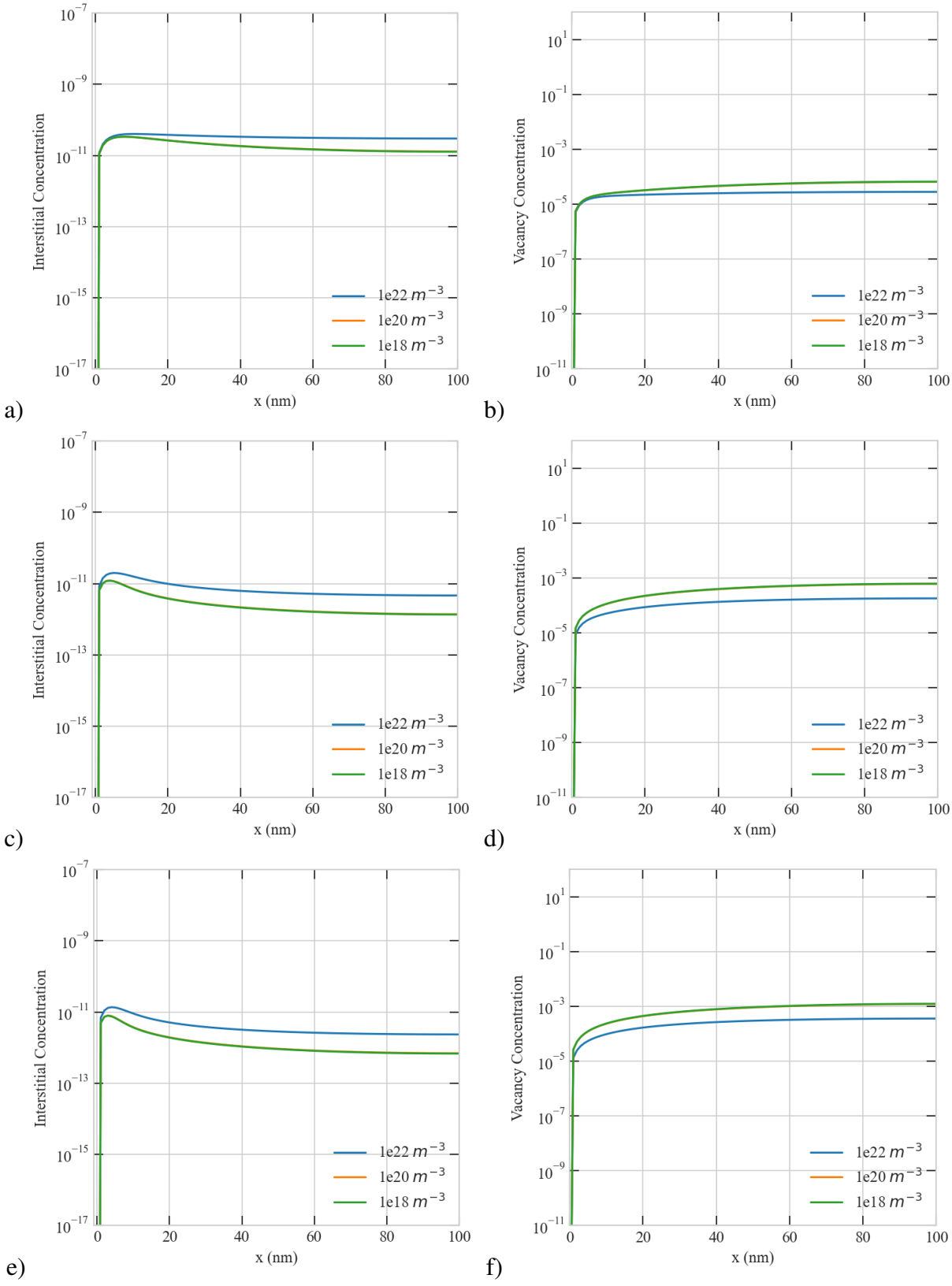

Figure 4.74: Effect of sink density on the steady-state concentration profiles of point defects in a 100 nm at 1e-4 dpa/s a) 1% bias, interstitial b) 1% bias, vacancy c) 10% bias, interstitial d) 10% bias, vacancy e) 20% bias, interstitial and f) 20% bias, vacancy concentrations.

At 473 K, instability on point defects has become prevailing for all sizes we have considered. As discussed, the instability was not observed at 773 K for 1e22 m^{-3} sink density in any sizes. However, this instability is seen at 473 K for 1e22 m^{-3} sink density at the dose rate of 1e-4 dpa/s with 10% bias in 100 nm (see Fig. 4.76).

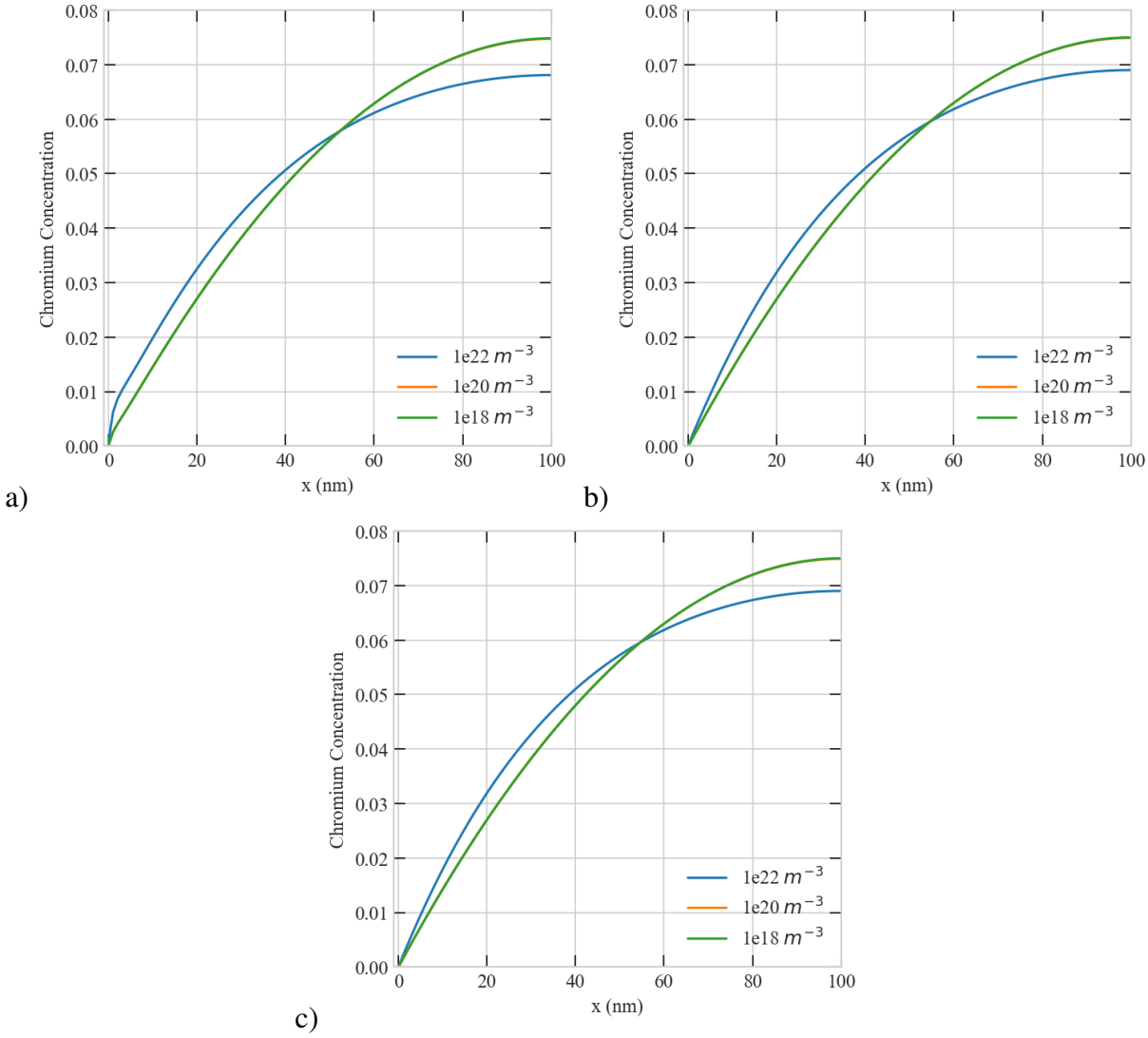

Figure 4.75: Effect of sink density on the steady-state concentration profiles of Chromium in a 100 nm at 1e-2 dpa/s a) 1% bias, Cr concentration b) 10% bias, Cr concentration c) 20% bias, Cr concentration.

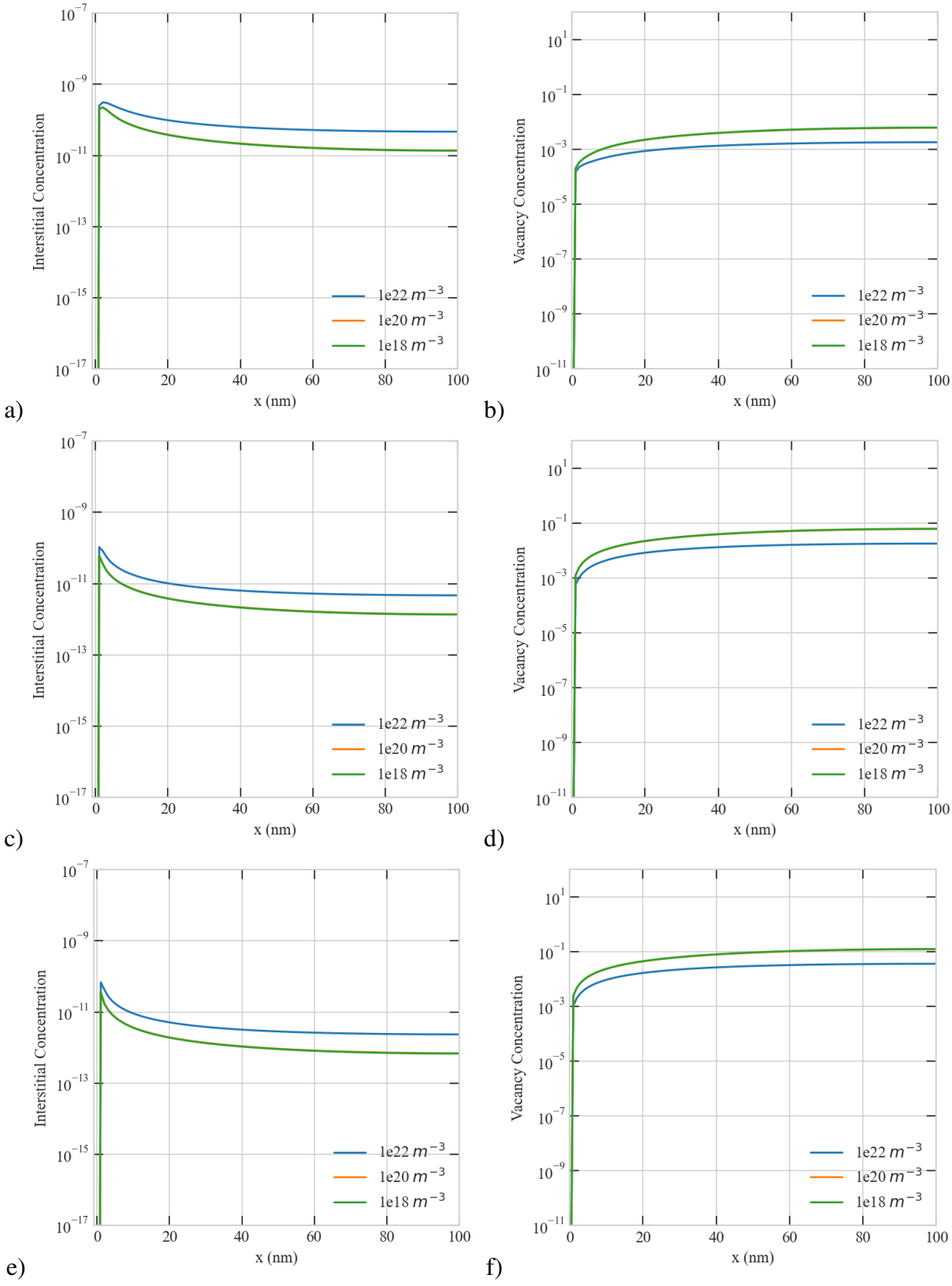

Figure 4.76: Effect of sink density on the steady-state concentration profiles of point defects in a 100 nm at 1e-2 dpa/s a) 1% bias, interstitial b) 1% bias, vacancy c) 10% bias, interstitial d) 10% bias, vacancy e) 20% bias, interstitial and f) 20% bias, vacancy concentrations.

As shown in Fig. 4.77, for 1e22 m^{-3} sink density, the magnitude of depletion of Cr at the boundary increases with bias in 300 nm. Cr depletion profile for 1e18 and 1e20 m^{-3} sink densities with 10% and 20% biases is similar at the dose rate of 5.6e-6 dpa/s. Besides, the vacancy concentration gradients in the vicinity of the boundary increases, while the interstitial counterpart decreases with bias.

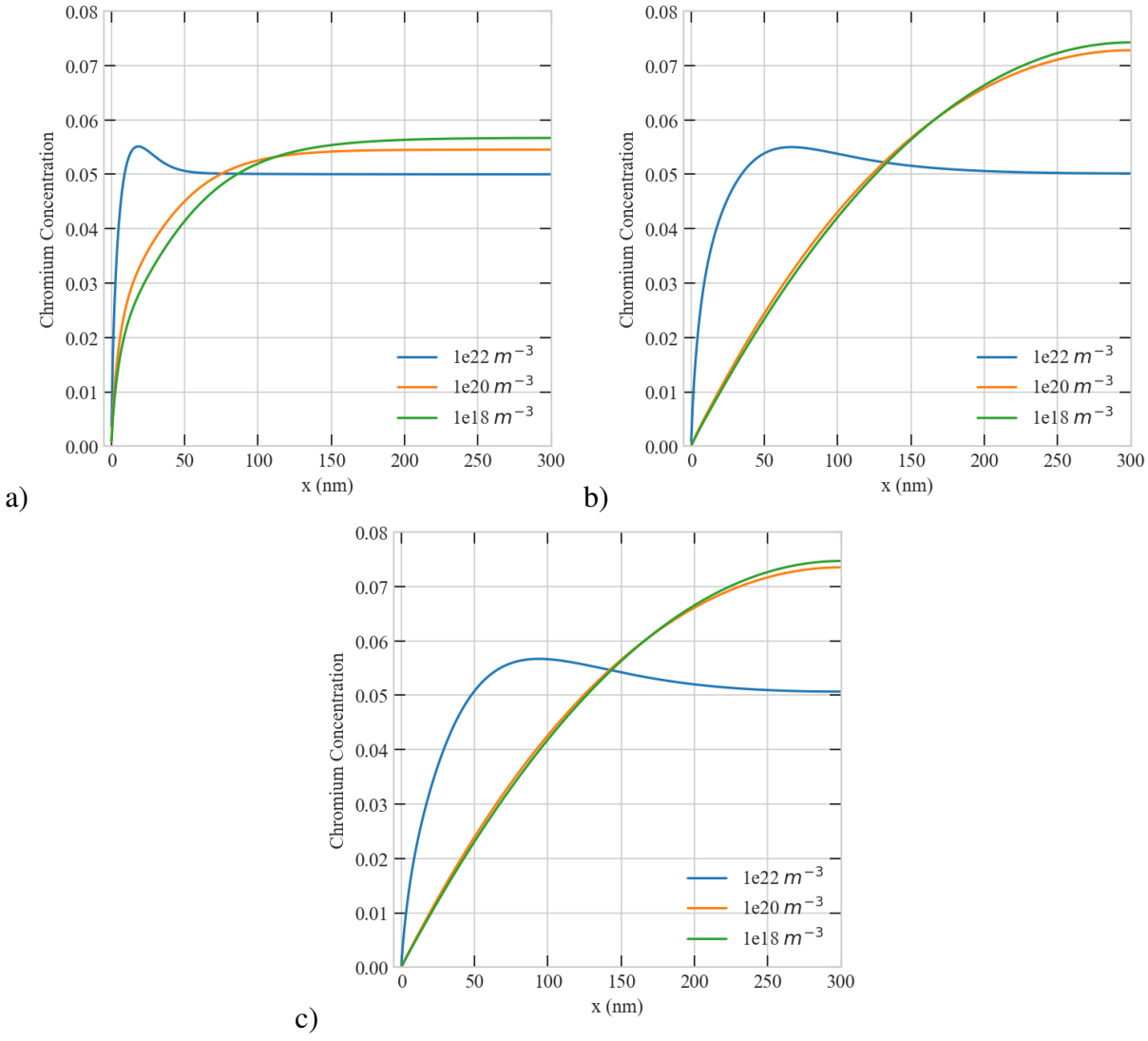

Figure 4.77: Effect of sink density on the steady-state concentration profiles of Chromium in a 300 nm at 5.6e-6 dpa/s a) 1% bias, Cr concentration b) 10% bias, Cr concentration c) 20% bias, Cr concentration.

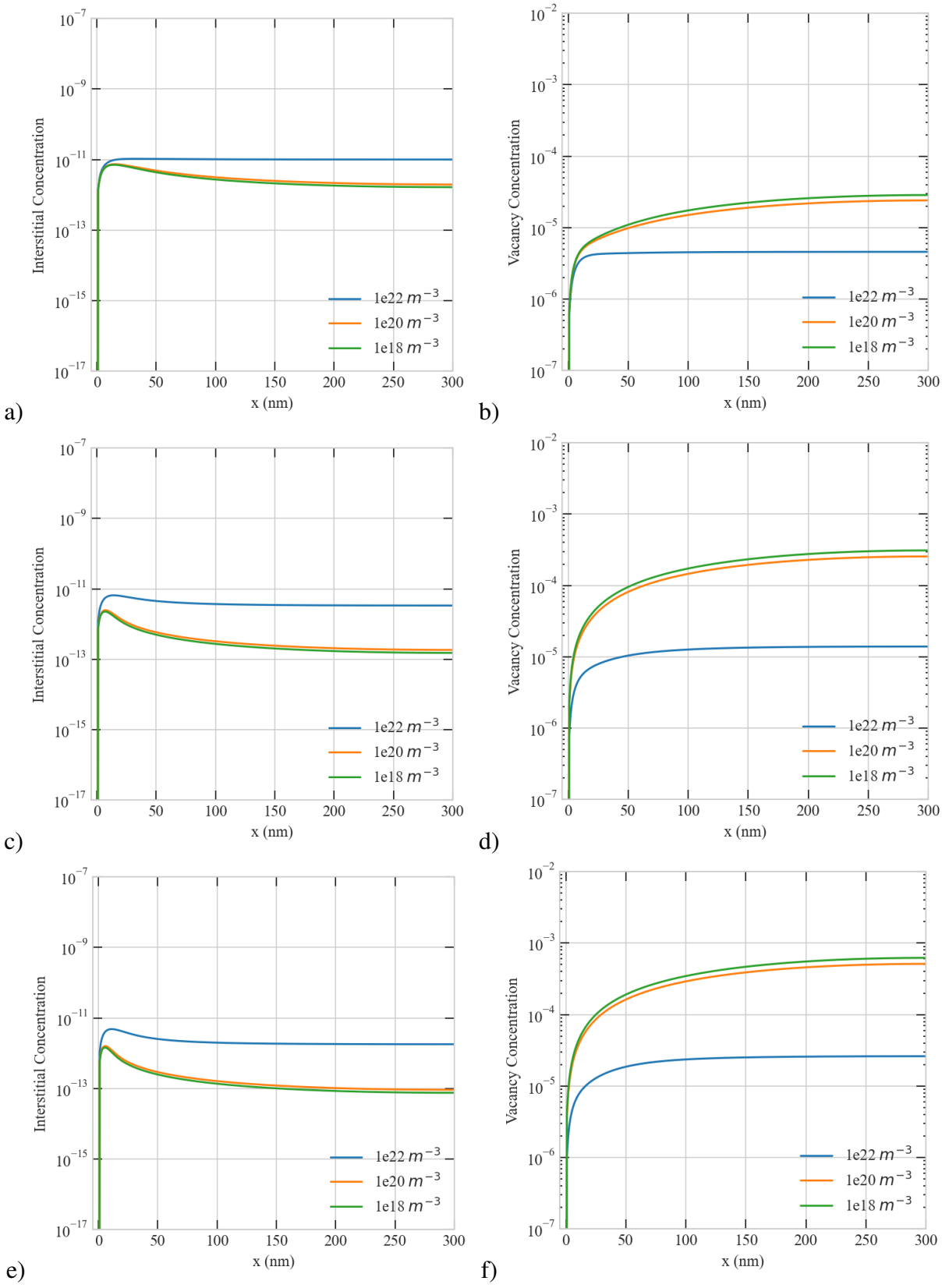

Figure 4.78: Effect of sink density on the steady-state concentration profiles of point defects in a 100 nm at 5.6e-6 dpa/s a) 1% bias, interstitial b) 1% bias, vacancy c) 10% bias, interstitial d) 10% bias, vacancy e) 20% bias, interstitial and f) 20% bias, vacancy concentrations.

In Fig. 4.80, at the dose rate of 1e-4 dpa/s, vacancy and interstitial concentrations shows opposite trends, as we have seen earlier at 573 K. The anomaly in the dependence of interstitial accumulation leads to increase in Cr depletion at the boundary. Additionally, it has become more apparent with bias (see Fig. 4.79).

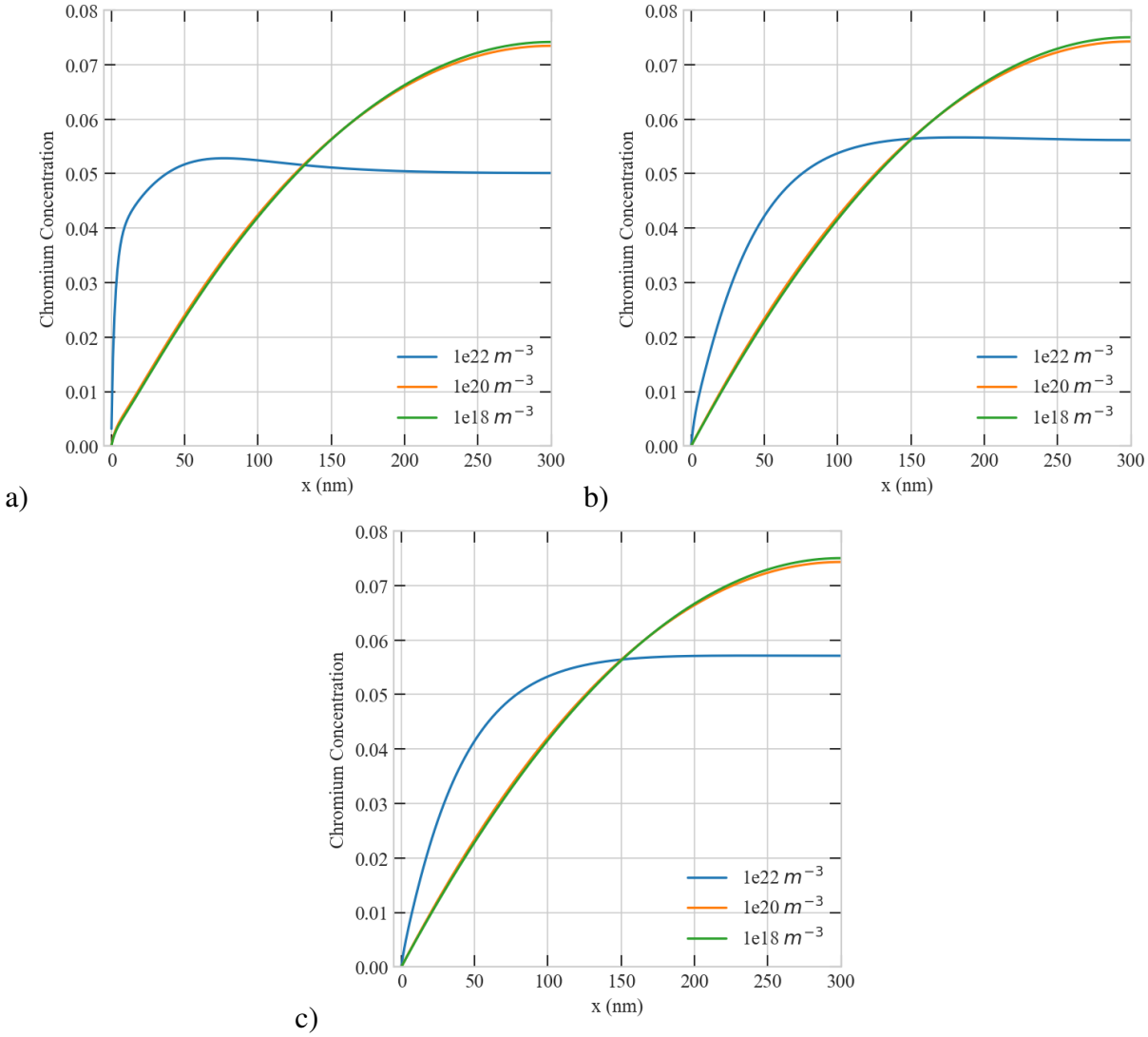

Figure 4.79: Effect of sink density on the steady-state concentration profiles of Chromium in a 300 nm at 1e-4 dpa/s a) 1% bias, Cr concentration b) 10% bias, Cr concentration c) 20% bias, Cr concentration.

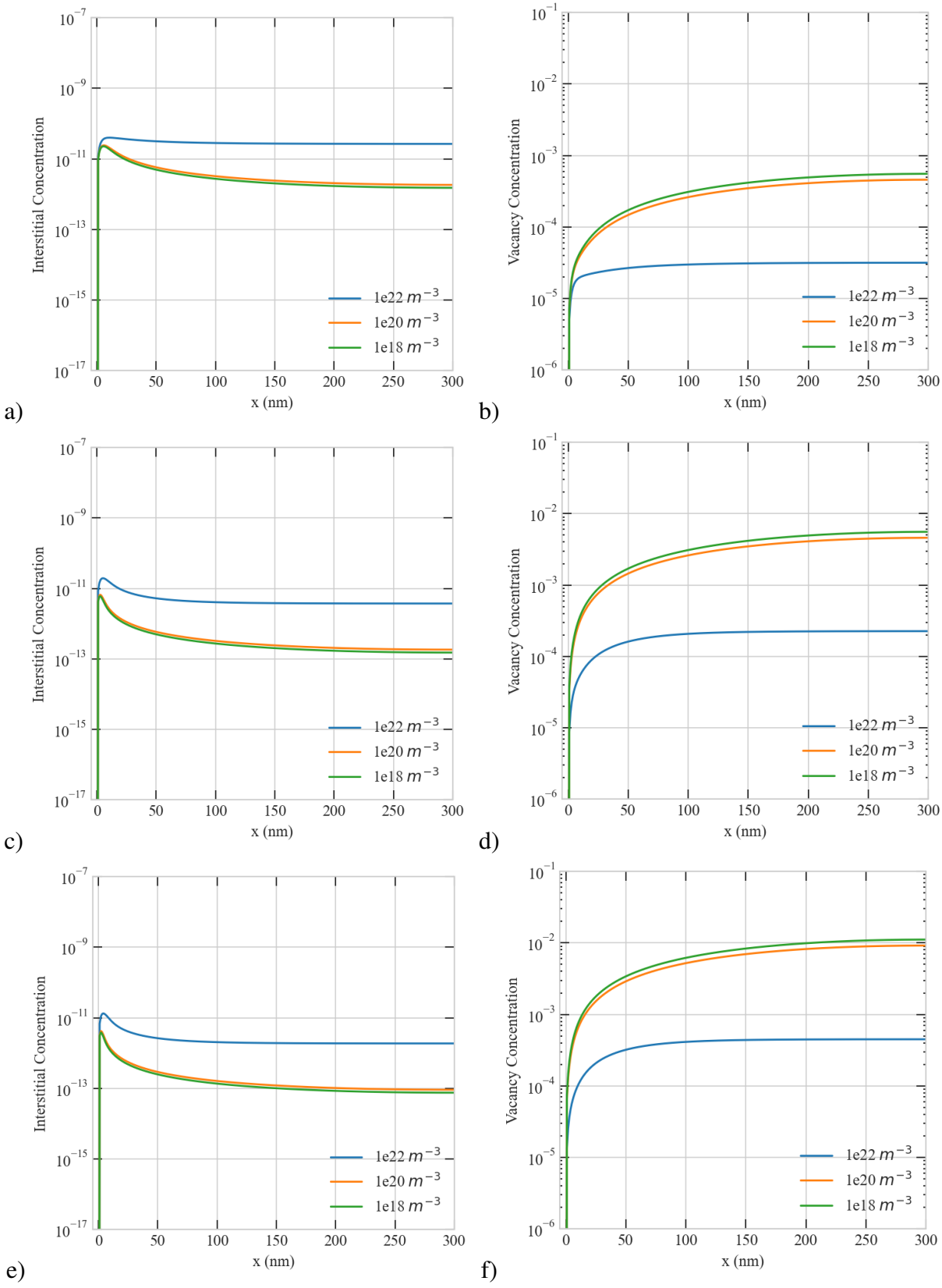

Figure 4.80: Effect of sink density on the steady-state concentration profiles of point defects in a 300 nm at 1e-4 dpa/s a) 1% bias, interstitial b) 1% bias, vacancy c) 10% bias, interstitial d) 10% bias, vacancy e) 20% bias, interstitial and f) 20% bias, vacancy concentrations.

In Fig. 4.77, we observed that for 1e22 m^{-3} sink density, there is an accumulation in Cr concentration in the vicinity of the boundary. It could be attributed to the anomaly on the point defects at the dose rate of 5.6e-6 dpa/s in 500 nm. In Fig. 4.78, for 1e18 and 1e20 m^{-3} sink densities, the vacancy concentration increases, while the interstitial counterpart decreases with bias.

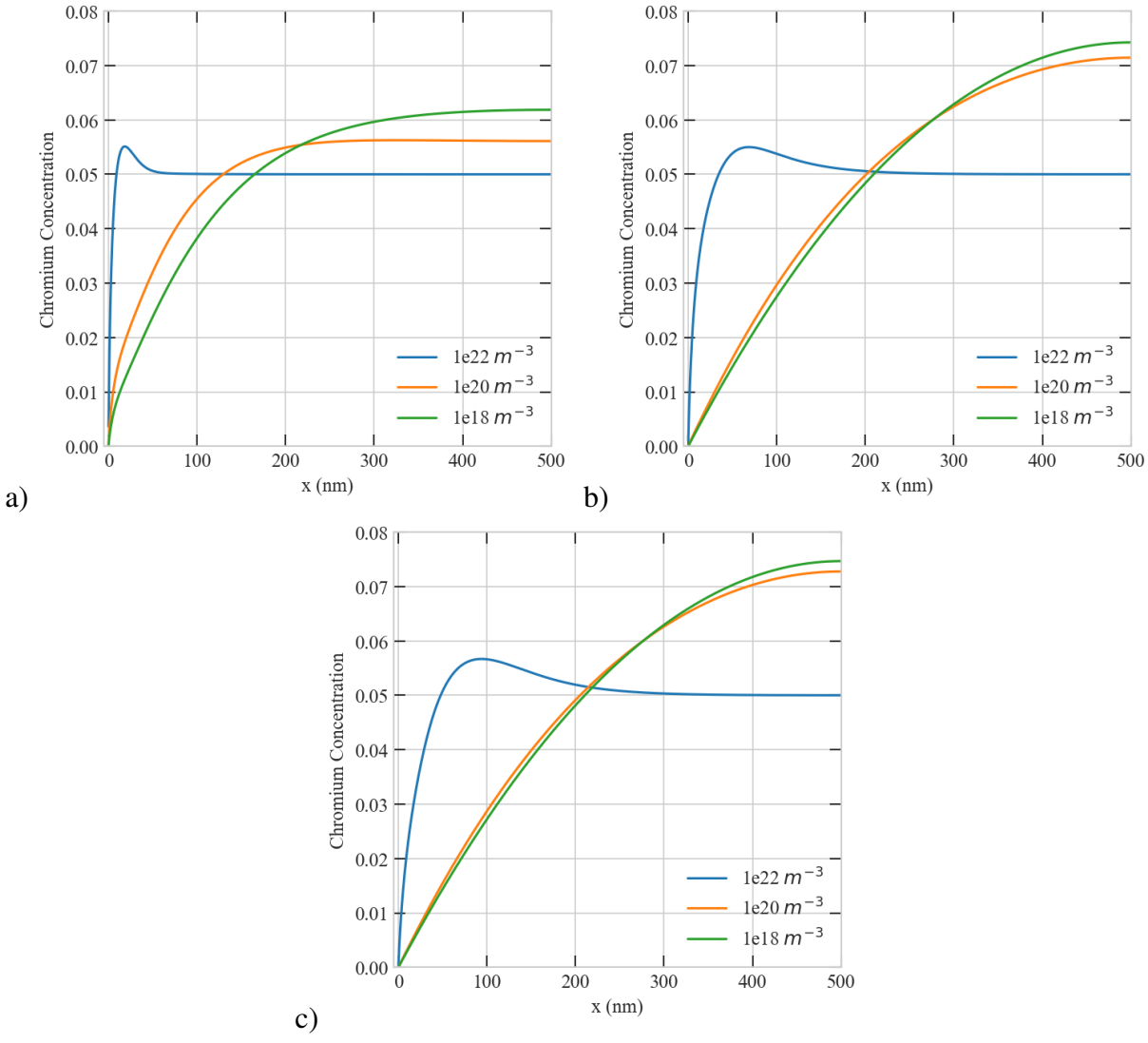

Figure 4.81: Effect of sink density on the steady-state concentration profiles of Chromium in a 500 nm at 5.6e-6 dpa/s a) 1% bias, Cr concentration b) 10% bias, Cr concentration c) 20% bias, Cr concentration.

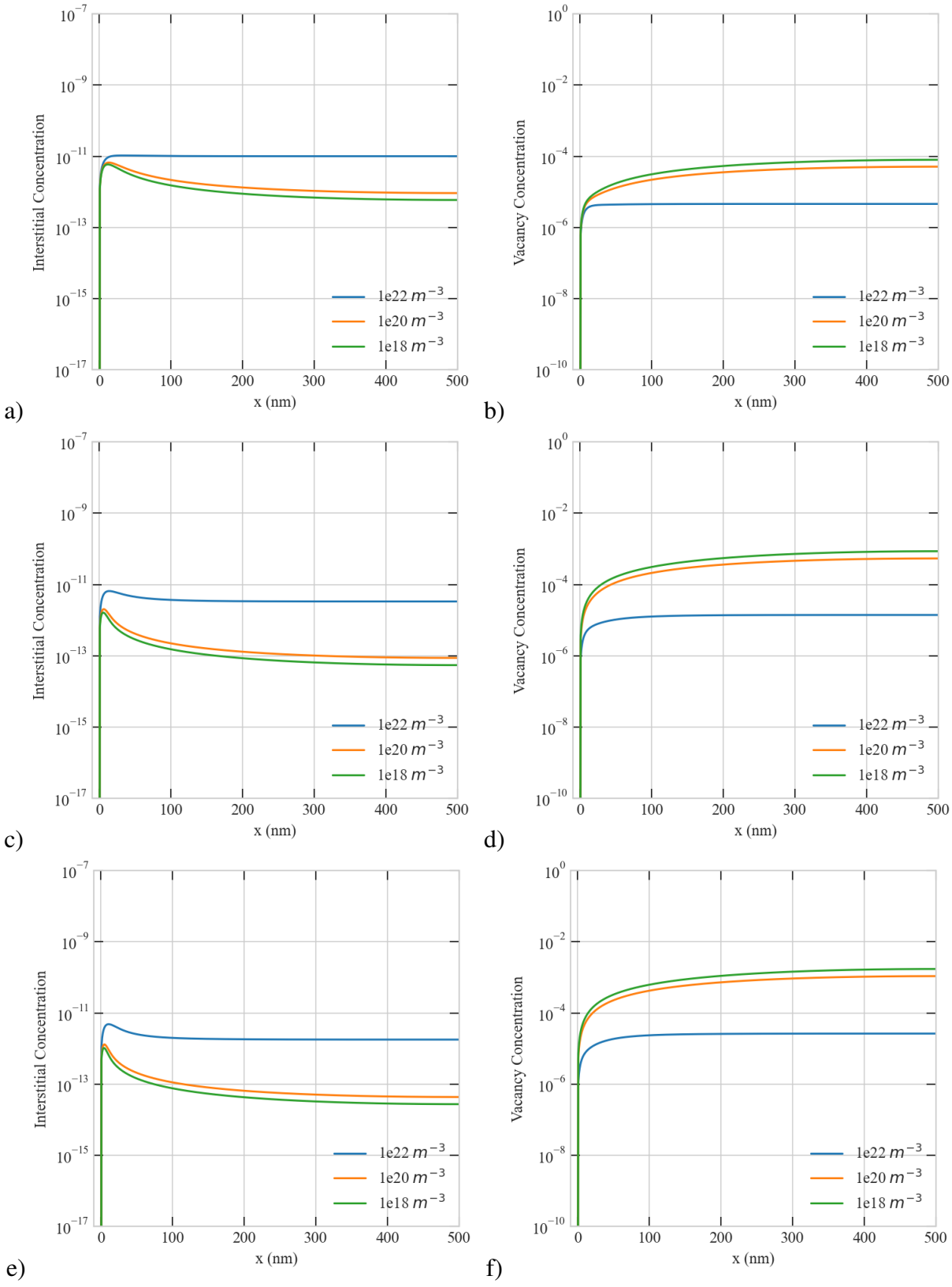

Figure 4.82: Effect of sink density on the steady-state concentration profiles of point defects in a 500 nm at 5.6e-6 dpa/s a) 1% bias, interstitial b) 1% bias, vacancy c) 10% bias, interstitial d) 10% bias, vacancy e) 20% bias, interstitial and f) 20% bias, vacancy concentrations.

Accumulation in Cr concentration in the vicinity of the boundary in 300 nm (see Fig. 4.77), begins to lose its persistence at the dose rate of 1e-4 dpa/s in 500 nm Fig. 4.83. In Fig. 4.84, at the dose rate of 1e-4 dpa/s, for all sink density cases, vacancy concentration increases, while the interstitial counterpart decreases with bias.

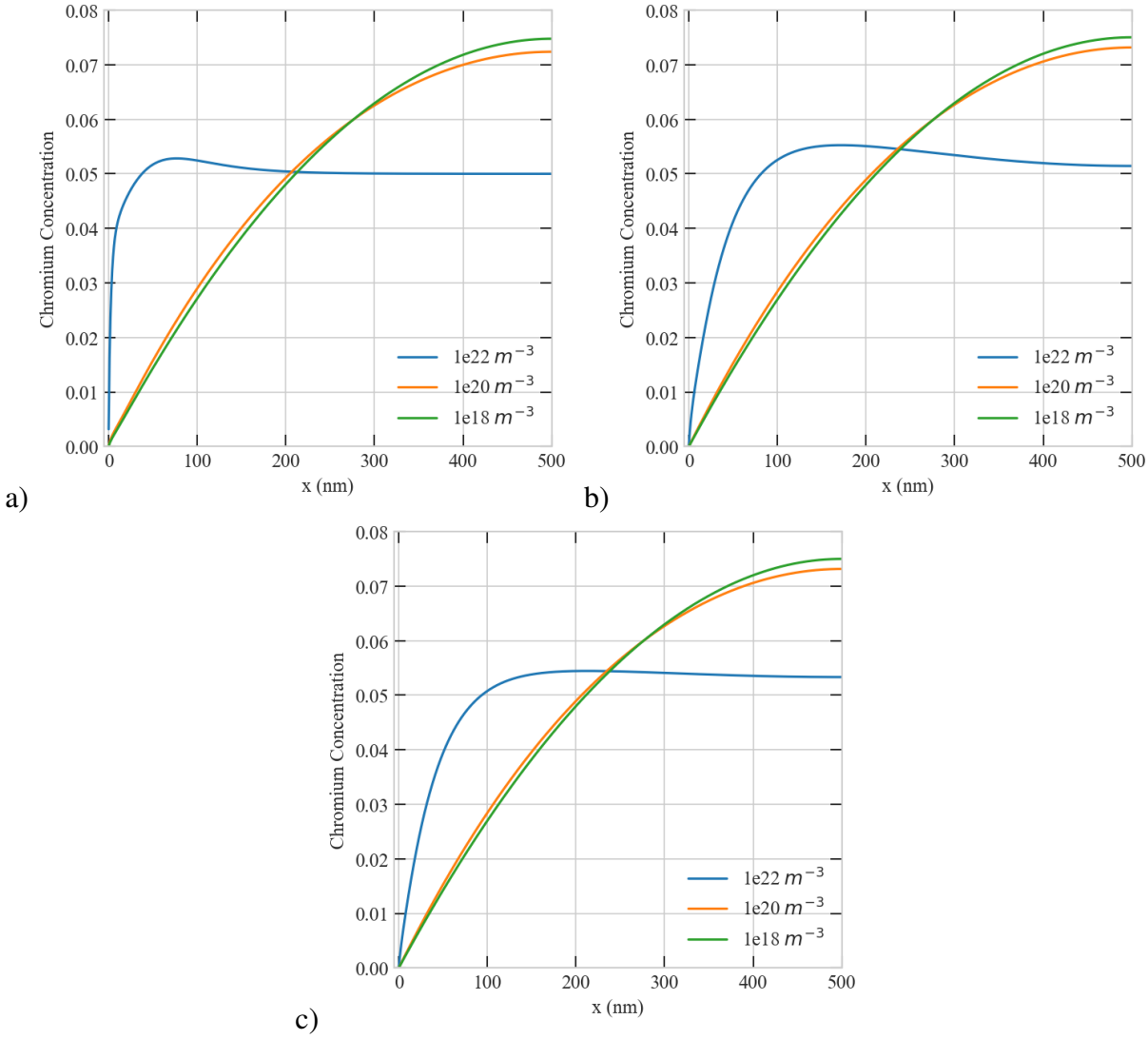

Figure 4.83: Effect of sink density on the steady-state concentration profiles of Chromium in a 500 nm at 1e-4 dpa/s a) 1% bias, Cr concentration b) 10% bias, Cr concentration c) 20% bias, Cr concentration.

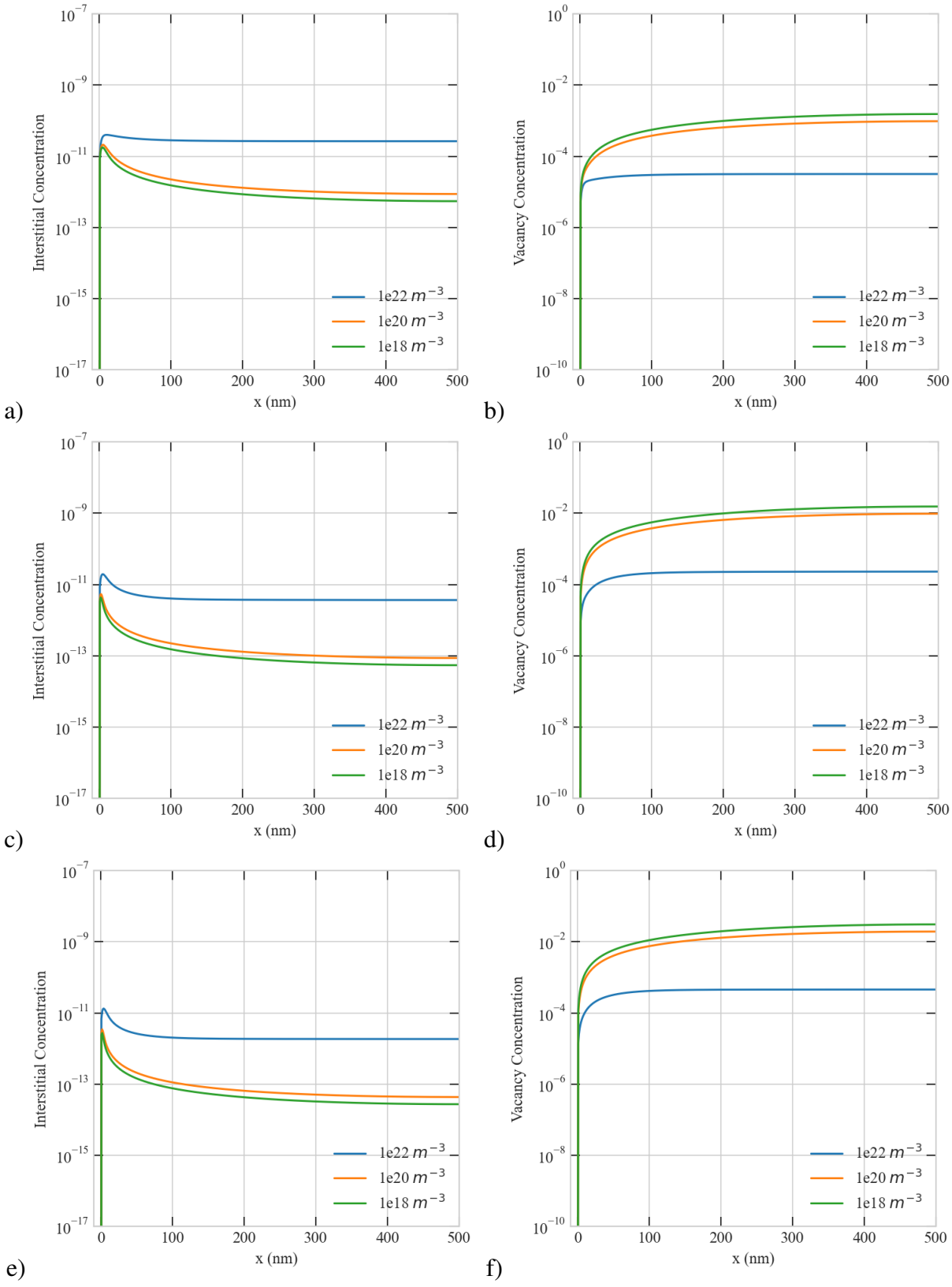

Figure 4.84: Effect of sink density on the steady-state concentration profiles of point defects in a 500 nm at 1e-4 dpa/s a) 1% bias, interstitial b) 1% bias, vacancy c) 10% bias, interstitial d) 10% bias, vacancy e) 20% bias, interstitial and f) 20% bias, vacancy concentrations.

At the dose rate of 1e-2 dpa/s, the effect of increasing production bias was lowest on interstitial and vacancy concentrations profile in 5000 nm. Moreover, Cr concentration profile remains significantly similar for three production biases. (see Fig.4.37 and Fig. 4.38).

At the dose rate of 5.6e-6 dpa/s, changing the sink density have a visible effect on the width of the Cr depletion layer in 7500 nm (see Fig. 4.86). In Fig. 4.86, interstitial and vacancy concentrations show strong dependence on production bias.

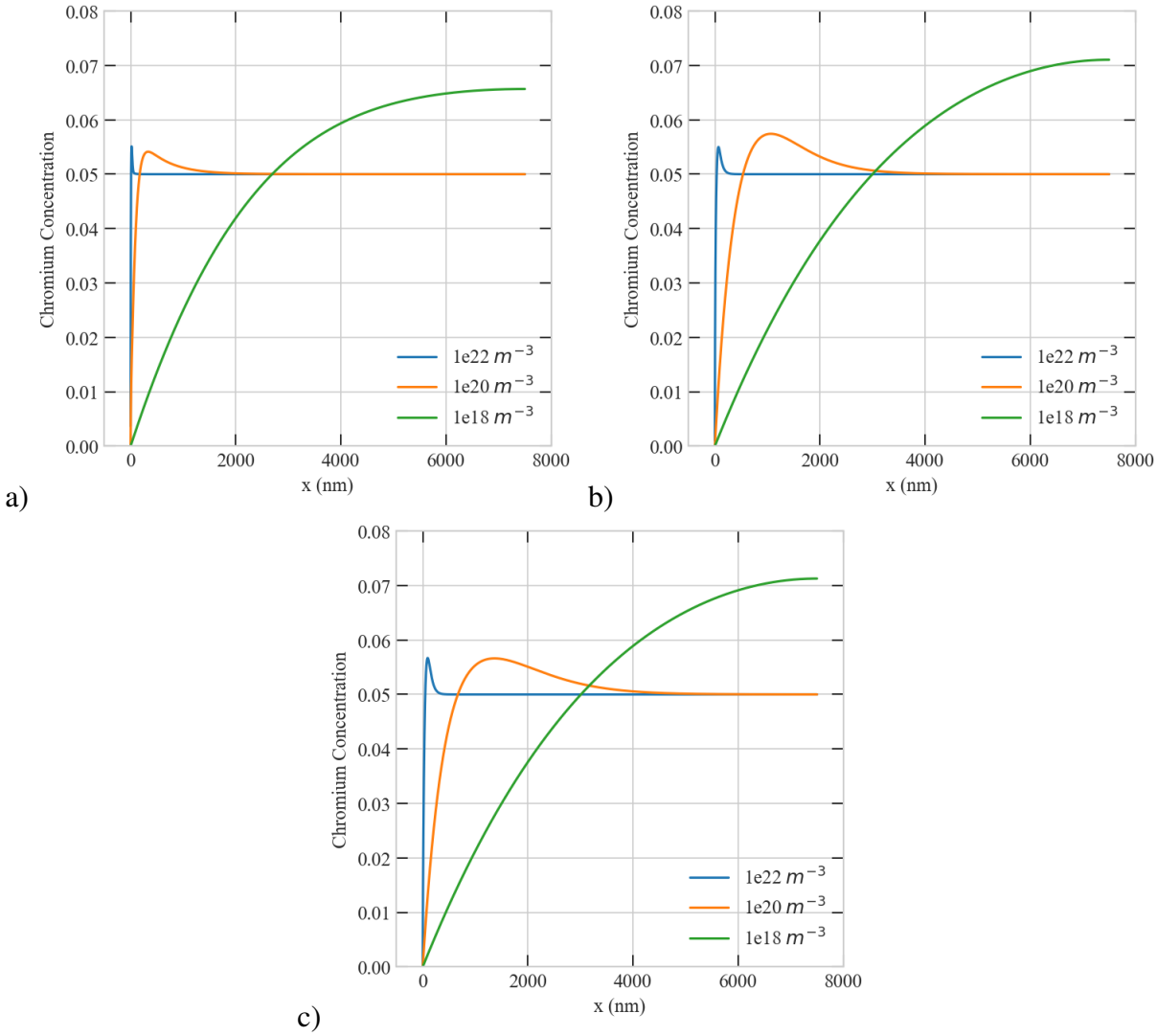

Figure 4.85: Effect of sink density on the steady-state concentration profiles of Chromium in a 7500 nm at 5.6e-6 dpa/s a) 1% bias, Cr concentration b) 10% bias, Cr concentration c) 20% bias, Cr concentration.

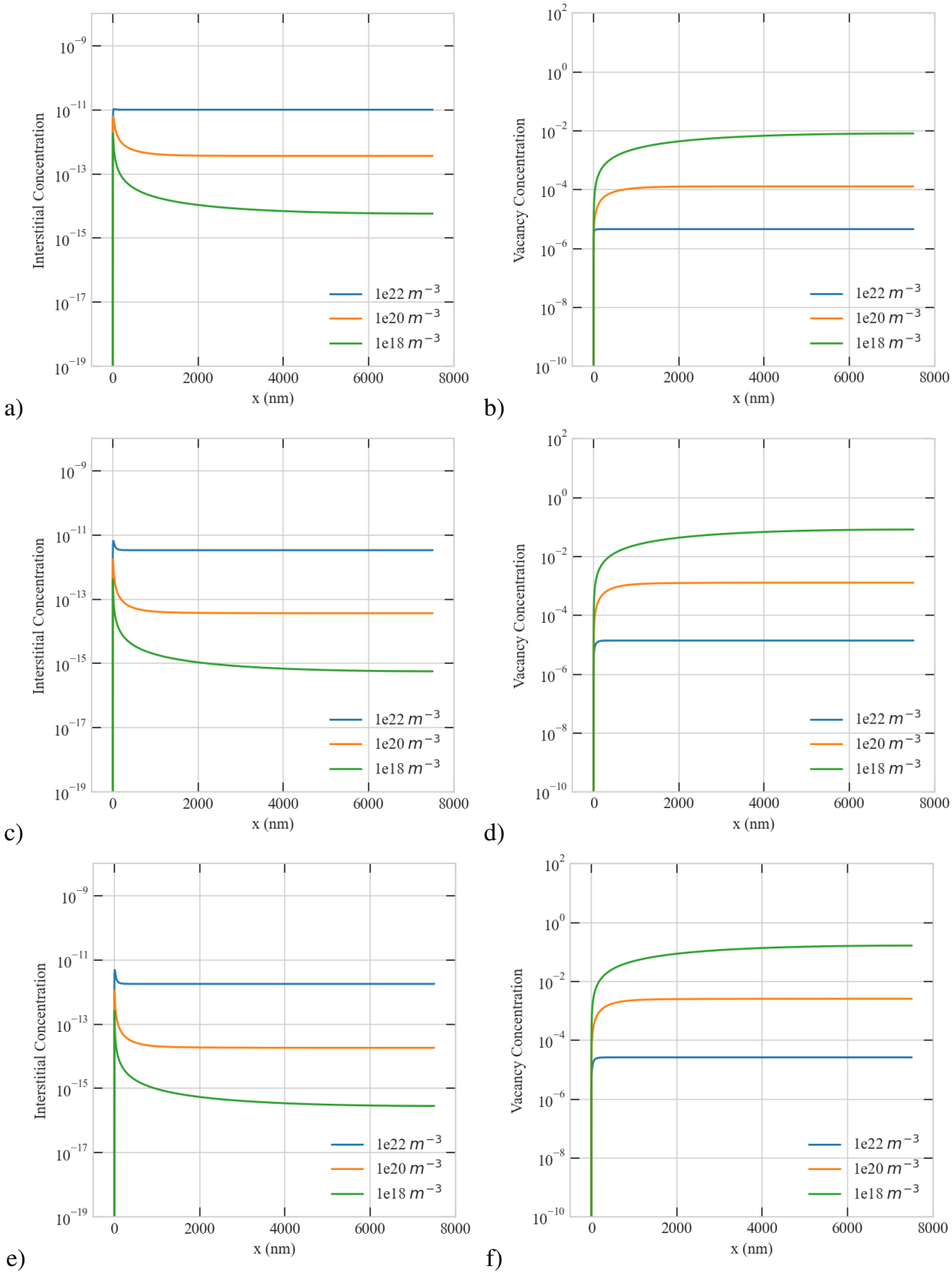

Figure 4.86: Effect of sink density on the steady-state concentration profiles of point defects in a 7500 nm at 5.6e-6 dpa/s a) 1% bias, interstitial b) 1% bias, vacancy c) 10% bias, interstitial d) 10% bias, vacancy e) 20% bias, interstitial and f) 20% bias, vacancy concentrations.

With the increase in temperature from 473 K to 773 K, the mobility of defects increases. Therefore, the recombination rate of vacancy and interstitials increases in response to temperature. A higher recombination rate reduces more vacancy, and hence, the gradient of vacancy in the vicinity of the boundary decreases. Moreover, our investigation shows that sink density affects Cr concentration in the vicinity of the boundary. More interestingly, its effect increases with the production bias and size, and therefore the width of the Cr depletion layer is widened.

On the other hand, a decrease in the sink density leads to an increase in vacancy gradient in the vicinity of the boundary, causing an increase in Cr depletion. Therefore, radiation damage becomes more severe near the boundary. Additionally, anomaly related to the accumulation of interstitials causes opposite trend on point defects. The beginning of this instability is attributed production bias. Production bias breaks the symmetry of the balance of point defects leading to non-uniform bulk recombination and non-uniform losses to surface/boundary, which ultimately bring about distinct steady-state profiles. We observed that this instability does not appear in 100 nm with production bias at the dose rate of 5.6e-6 dpa/s and 773 K. However, it appears effectively in 100 nm with production bias at the dose rate of 5.6e-6 dpa/s and 473 K.

4.6 Comparison with Experimental Data

We compared the results with the available experimental data in the literature [49]. At 773 K, sink density of 1e20 m^{-3} and 5.6e-6 dpa/s parameters is considered. Also, the average grain size is taken 145 μm as in experimental results. The experimental study indicated that RIS profiles show distinguished varieties as a function of the grain boundary character. The coherent boundary has a low interaction with vacancies, and hence grain boundary behaves as a weak defect sink. Therefore, Cr depletion is reduced at the boundary. On the other hand, the incoherent boundary has higher Cr depletion and behaves better defect sink than the coherent boundary. In our model, we treated the boundary as a perfect sink for point defects, fixing point defects at their thermal equilibrium values at the boundary. Consequently, the model results shows better agreement with the incoherent boundary. Furthermore, experimental samples were irradiated with heavy ion irradiation, and hence heavy ions create highly dense cascades, leading to high bias. It can be seen that

10% bias captures this qualitative behavior considerably well. Fig. 4.87 depicts model predictions for the case of 145 μm grain size and comparison with the available experimental data.

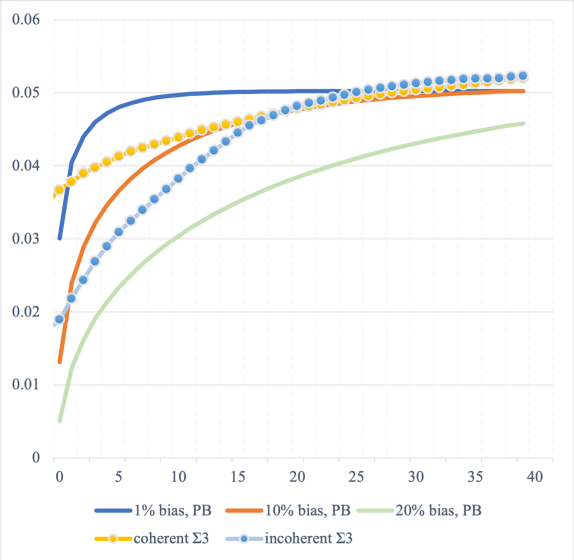

Figure 4.87: Model predictions for the case of 145 μm grain size and comparison with the available experimental data.

Here, the boundary is assumed as an ideal sink, enabling interstitials and vacancies to be immediately annihilated when they reach the sink. Thus, defect concentration near the sink is equivalent to the thermal equilibrium values. However, the boundary condition affects the sink efficiency [60] [61]. Also, Cr concentration may change from boundary to the boundary in materials under the same irradiation [49] [60] [62]. Evaluating the sink differently may provide a better agreement between RIS and grain boundary structures at different temperatures.

5. SUMMARY AND FUTURE DIRECTIONS

5.1 Summary

To better understand radiation-induced segregation in Ni–Cr alloys, spatially resolved rate-theory approach is employed. The calculations performed to estimate the rate equations for the alloy atoms and point defect concentrations for different irradiation conditions. We applied the production bias model (PBM) to investigate radiation-induced segregation and its effect on radiation damage. In this model, defects concentration profiles are consistent with the void denuded zones which cannot be described in terms of the conventional rate theory model. The balance equations for point defects and alloy atoms were solved simultaneously using a fully-coupled and fully-implicit scheme implemented in the Multiphysics Object-Oriented Simulation Environment (MOOSE) framework, considering the combined effects of dose rate, temperature, grain size, sink density, and defect production bias. Simulations have been conducted and compared with the available experimental data to validate the model.

The present study makes noteworthy contributions to the dependence of RIS on size, production bias, and temperature. Our results show that the accumulation of interstitials and the depletion of vacancies in the vicinity of the grain boundary consistent with void denuded zones. We also demonstrate that the magnitude of enrichment/depletion of Ni/Cr at the boundary increases with size, and the width of the enrichment/depletion layer also increases with size. Furthermore, as the temperature decreases, RIS becomes more apparent with higher segregation of Ni and depletion of Cr at the boundary as the production bias increases. It is also noteworthy to the point that RIS shows dependency on the irradiation type and conditions. Changing the sink density tends to alter the width of the enrichment/depletion layer of RIS. Moreover, when surface and size effects are considered, qualitative differences in the irradiation response of materials to different irradiation types are expected. Here, we proved that, in addition to its known dependence on material and size/microstructure, the surface/boundary sink strength is dependent on irradiation type.

5.2 Future Directions

In the current model, the boundary is assumed as an ideal sink. As a result, vacancies and interstitials are annihilated when they reach the sink. Thus, defect concentration in the vicinity of the sink is equivalent to the thermal equilibrium concentration. However, as we discussed earlier boundary conditions affect the sink efficiency.

Also, our results show that irradiation damage has become more severe at the boundary at low-temperature. This could be attributed to the uncertainties associated with interstitial diffusivities at low temperatures. Therefore, RIS model will require more accurate Ni and Cr interstitial diffusivities determination.

We will include a modified boundary condition that considers defect annihilation kinetics to improve the agreement with the experimental data for future work.

REFERENCES

[1] A. Barashev, Y. Osetsky, H. Bei, C. Lu, L. Wang, and Y. Zhang, "Chemically-biased diffusion and segregation impede void growth in irradiated Ni-Fe alloys," *Current Opinion in Solid State and Materials Science*, vol. 23, pp. 92–100, Apr. 2019.

[2] S. A. Briggs, C. M. Barr, J. Pakarinen, M. Mamivand, K. Hattar, D. D. Morgan, M. Taheri, and K. Sridharan, "Observations of defect structure evolution in proton and Ni ion irradiated Ni-Cr binary alloys," *Journal of Nuclear Materials*, vol. 479, pp. 48–58, Oct. 2016.

[3] G. S. Was, *Fundamentals of Radiation Materials Science*. New York, NY: Springer New York, 2017.

[4] G. Was, J. Busby, T. Allen, E. Kenik, A. Jensson, S. Bruemmer, J. Gan, A. Edwards, P. Scott, and P. Andreson, "Emulation of neutron irradiation effects with protons: validation of principle," *Journal of Nuclear Materials*, vol. 300, pp. 198–216, Feb. 2002.

[5] T. R. Anthony, "Segregation of Zinc to Vacancy Sinks in Aluminum," *Journal of Applied Physics*, vol. 41, pp. 3969–3976, Sept. 1970.

[6] S. Bruemmer, E. Simonen, P. Scott, P. Andresen, G. Was, and J. Nelson, "Radiation-induced material changes and susceptibility to intergranular failure of light-water-reactor core internals," *Journal of Nuclear Materials*, vol. 274, pp. 299–314, Sept. 1999.

[7] S. Zinkle and G. Was, "Materials challenges in nuclear energy," *Acta Materialia*, vol. 61, pp. 735–758, Feb. 2013.

[8] O. of Nuclear Energy, "Light Water Reactor Sustainability (LWRS) Program."

[9] M. Nastar and F. Soisson, "Radiation-Induced Segregation," in *Comprehensive Nuclear Materials*, pp. 471–496, Elsevier, 2012.

[10] J. Haley, S. de Moraes Shubeita, P. Wady, A. London, G. Odette, S. Lozano-Perez, and S. Roberts, "Microstructural examination of neutron, proton and self-ion irradiation damage in a model Fe9Cr alloy," *Journal of Nuclear Materials*, vol. 533, p. 152130, May 2020.

[11] C. Zheng and D. Kaoumi, "Radiation-induced swelling and radiation-induced segregation & precipitation in dual beam irradiated Ferritic/Martensitic HT9 steel," *Materials Characterization*, vol. 134, pp. 152–162, Dec. 2017.

[12] Y. Yang, K. G. Field, T. R. Allen, and J. T. Busby, "Roles of vacancy/interstitial diffusion and segregation in the microchemistry at grain boundaries of irradiated Fe–Cr–Ni alloys," *Journal of Nuclear Materials*, vol. 473, pp. 35–53, May 2016.

[13] S. Zinkle, P. Maziasz, and R. Stoller, "Dose dependence of the microstructural evolution in neutron-irradiated austenitic stainless steel," *Journal of Nuclear Materials*, vol. 206, pp. 266–286, Nov. 1993.

[14] T. R. Allen, L. Tan, G. S. Was, and E. A. Kenik, "Thermal and radiation-induced segregation in model Ni-base alloys," *Journal of Nuclear Materials*, p. 10, 2007.

[15] A. J. Ardell, "Radiation-induced solute segregation in metallic alloys," *Current Opinion in Solid State and Materials Science*, p. 25, 2016.

[16] K. Ahmed and A. El-Azab, "An analysis of two classes of phase field models for void growth and coarsening in irradiated crystalline solids," *Materials Theory*, vol. 2, p. 1, Dec. 2018.

[17] B. Tanguy, M. Sauzay, C. Robertson, and S. Perrin, "The Irradiation-Assisted Stress Corrosion Cracking (IASCC) Issue: some Examples of Studies Carried out at CEA," *EPJ Web of Conferences*, vol. 51, p. 04002, 2013.

[18] T. Allen, G. Was, and E. Kenik, "The effect of alloy composition on radiation-induced segregation in FeCrNi alloys," *Journal of Nuclear Materials*, vol. 244, pp. 278–294, Apr. 1997.

[19] J. Busby, G. Was, and E. Kenik, "Isolating the effect of radiation-induced segregation in irradiation-assisted stress corrosion cracking of austenitic stainless steels," *Journal of Nuclear Materials*, vol. 302, pp. 20–40, Apr. 2002.

[20] S. Watanabe, N. Sakaguchi, N. Hashimoto, and H. Takahashi, "Quantitative studies of irradiation-induced segregation and grain boundary migration in FeCrNi alloy," *Journal of Nuclear Materials*, vol. 224, pp. 158–168, Aug. 1995.

[21] K. J. Stephenson and G. S. Was, "Comparison of the microstructure, deformation and crack initiation behavior of austenitic stainless steel irradiated in-reactor or with protons," *Journal of Nuclear Materials*, vol. 456, pp. 85–98, Jan. 2015.

[22] J. Tucker, R. Najafabadi, T. Allen, and D. Morgan, "Ab initio-based diffusion theory and tracer diffusion in Ni–Cr and Ni–Fe alloys," *Journal of Nuclear Materials*, vol. 405, pp. 216–234, Oct. 2010.

[23] B. N. SINGH, "Void Volume Swelling dependent on Grain Size in an Austenitic Stainless Steel," *Nature Physical Science*, vol. 244, pp. 142–142, Aug. 1973.

[24] B. N. Singh, "Effect of grain size on void formation during high-energy electron irradiation of austenitic stainless steel," *The Philosophical Magazine: A Journal of Theoretical Experimental and Applied Physics*, vol. 29, pp. 25–42, Jan. 1974.

[25] A. Foreman, B. N. Singh, and A. Horsewell, "Diffusion Mechanisms for Enhanced Vacancy Accumulation Near Planar Sinks," *Materials Science Forum*, vol. 15-18, pp. 895–900, 1987. Publisher: Trans Tech Publications Ltd.

[26] M. Victoria and W. V. Green, "AND GROWTH IN ALUMINIUM DURING 600 MeV," p. 6.

[27] B. Singh and S. Zinkle, "Defect accumulation in pure fcc metals in the transient regime: a review," *Journal of Nuclear Materials*, vol. 206, pp. 212–229, Nov. 1993.

[28] C. English, "Low-dose neutron irradiation damage in FCC and BCC metals," *Journal of Nuclear Materials*, vol. 108-109, pp. 104–123, July 1982.

[29] T. Leffers and B. N. Singh, "Recombination cross section for interstitials and vacancies as a function of vacancy concentration," *Radiation Effects*, vol. 59, pp. 83–89, Jan. 1981. Publisher: Taylor & Francis.

[30] N. Q. Lam, S. J. Rothman, and R. Sizmanns, "Steady-state point-defect diffusion profiles in solids during irradiation," *Radiation Effects*, vol. 23, pp. 53–59, Jan. 1974. Publisher: Taylor & Francis.

[31] B. N. Singh and A. J. E. Foreman, "Calculated grain size-dependent vacancy supersaturation and its effect on void formation," *The Philosophical Magazine: A Journal of Theoretical Experimental and Applied Physics*, vol. 29, pp. 847–858, Apr. 1974. Publisher: Taylor & Francis.

[32] C. H. Woo and B. N. Singh, "The Concept of Production Bias and Its Possible Role in Defect Accumulation under Cascade Damage Conditions," *physica status solidi (b)*, vol. 159, pp. 609–616, June 1990. Publisher: John Wiley & Sons, Ltd.

[33] C. H. Woo and B. N. Singh, "Production bias due to clustering of point defects in irradiation-induced cascades," *Philosophical Magazine A*, vol. 65, pp. 889–912, Apr. 1992. Publisher: Taylor & Francis.

[34] B. N. Singh and A. J. E. Foreman, "Production bias and void swelling in the transient regime under cascade damage conditions," *Philosophical Magazine A*, vol. 66, pp. 975–990, Dec. 1992. Publisher: Taylor & Francis.

[35] B. N. Singh, M. Eldrup, S. J. Zinkle, and S. I. Golubov, "On grain-size-dependent void swelling in pure copper irradiated with fission neutrons," *Philosophical Magazine A*, vol. 82, pp. 1137–1158, Apr. 2002. Publisher: Taylor & Francis.

[36] H. Trinkaus, B. Singh, and A. Foreman, "Glide of interstitial loops produced under cascade damage conditions: Possible effects on void formation," *Journal of Nuclear Materials*, vol. 199, pp. 1–5, Dec. 1992.

[37] H. Trinkaus, B. N. Singh, and S. I. Golubov, "Progress in modelling the microstructural evolution in metals under cascade damage conditions," *Journal of Nuclear Materials*, p. 10, 2000.

[38] L. Shao, J. Gigax, D. Chen, H. Kim, F. A. Garner, J. Wang, and M. B. Toloczko, "Standardization of accelerator irradiation procedures for simulation of neutron induced damage in reactor structural materials," *Nuclear Instruments and Methods in Physics Research Section B: Beam Interactions with Materials and Atoms*, vol. 409, pp. 251–254, Oct. 2017.

[39] C. Sun, F. Garner, L. Shao, X. Zhang, and S. Maloy, "Influence of injected interstitials on the void swelling in two structural variants of 304L stainless steel induced by self-ion irradiation at 500 °C," *Nuclear Instruments and Methods in Physics Research Section B: Beam Interactions with Materials and Atoms*, vol. 409, pp. 323–327, Oct. 2017.

[40] J. P. Wharry and G. S. Was, "A systematic study of radiation-induced segregation in ferritic–martensitic alloys," *Journal of Nuclear Materials*, vol. 442, pp. 7–16, Nov. 2013.

[41] J. J. Kai, F. R. Chen, and T. S. Duh, "Effects of Grain Boundary Misorientation on Radiation-Induced Solute Segregation in Proton Irradiated 304 Stainless Steels," *MATERIALS TRANSACTIONS*, vol. 45, no. 1, pp. 40–50, 2004.

[42] L. Shao, C.-C. Wei, J. Gigax, A. Aitkaliyeva, D. Chen, B. Sencer, and F. Garner, "Effect of defect imbalance on void swelling distributions produced in pure iron irradiated with 3.5 MeV self-ions," *Journal of Nuclear Materials*, vol. 453, pp. 176–181, Oct. 2014.

[43] P. Okamoto and H. Wiedersich, "Segregation of alloying elements to free surfaces during irradiation," *Journal of Nuclear Materials*, vol. 53, pp. 336–345, Sept. 1974.

[44] A. D. Marwick, "Segregation in irradiated alloys: The inverse Kirkendall effect and the effect of constitution on void swelling," *Journal of Physics F: Metal Physics*, vol. 8, pp. 1849–1861, Sept. 1978.

[45] J. Perks, A. Marwick, and C. English, "A computer code to calculate radiation-induced segregation in concentrated ternary alloys," Tech. Rep. 0-7058-1104-2, United Kingdom, 1986. AERE-R–12121.

[46] T. R. Allen and G. S. Was, "Modeling radiation-induced segregation in austenitic Fe–Cr–Ni alloys," *Acta Materialia*, vol. 46, pp. 3679–3691, June 1998.

[47] L. Barnard, J. Tucker, S. Choudhury, T. Allen, and D. Morgan, "Modeling radiation induced segregation in Ni–Cr model alloys from first principles," *Journal of Nuclear Materials*, vol. 425, pp. 8–15, June 2012.

[48] H. Wiedersich, P. R. Okamoto, and N. Q. Lam, "A theory of radiation-induced segregation in concentrated alloys," *Journal of Nuclear Materials*, vol. 83, pp. 98–108, Aug. 1979.

[49] C. M. Barr, L. Barnard, J. E. Nathaniel, K. Hattar, K. A. Unocic, I. Szlurfarska, D. Morgan, and M. L. Taheri, "Grain boundary character dependence of radiation-induced segregation in a model Ni–Cr alloy," *Journal of Materials Research*, vol. 30, pp. 1290–1299, May 2015.

[50] Y. Yang, H. Huang, and S. J. Zinkle, "Anomaly in dependence of radiation-induced vacancy accumulation on grain size," *Journal of Nuclear Materials*, vol. 405, pp. 261–265, Oct. 2010.

[51] A. Ozturk, M. Gencturk, and K. Ahmed, "Surface and Size Effects on the behaviors of point defects in irradiated crystalline solids," p. 31.

[52] G. Was and S. Bruemmer, "Effects of irradiation on intergranular stress corrosion cracking," *Journal of Nuclear Materials*, vol. 216, pp. 326–347, Oct. 1994.

[53] K. Vörtler, M. Mamivand, L. Barnard, I. Szlufarska, F. Garner, and D. Morgan, "Simulated spatial and temporal dependence of chromium concentration in pure Fe and Fe 14%Cr under high dpa ion irradiation," *Journal of Nuclear Materials*, vol. 479, pp. 23–35, Oct. 2016.

[54] S. Choudhury, L. Barnard, J. Tucker, T. Allen, B. Wirth, M. Asta, and D. Morgan, "Ab-initio based modeling of diffusion in dilute bcc Fe–Ni and Fe–Cr alloys and implications for radiation induced segregation," *Journal of Nuclear Materials*, vol. 411, pp. 1–14, Apr. 2011.

[55] L. Barnard and D. Morgan, "Ab initio molecular dynamics simulation of interstitial diffusion in Ni–Cr alloys and implications for radiation induced segregation," *Journal of Nuclear Materials*, vol. 449, pp. 225–233, June 2014.

[56] M. Short, D. Gaston, M. Jin, L. Shao, and F. Garner, "Modeling injected interstitial effects on void swelling in self-ion irradiation experiments," *Journal of Nuclear Materials*, vol. 471, pp. 200–207, Apr. 2016.

[57] J. P. Wharry, Z. Jiao, and G. S. Was, "Application of the inverse Kirkendall model of radiation-induced segregation to ferritic–martensitic alloys," *Journal of Nuclear Materials*, vol. 425, pp. 117–124, June 2012.

[58] H. K. Zhang, Z. Yao, M. R. Daymond, and M. A. Kirk, "Elevated temperature irradiation damage in CANDU spacer material Inconel X-750," *Journal of Nuclear Materials*, vol. 445, pp. 227–234, Feb. 2014.

[59] G. S. Was, Z. Jiao, E. Getto, K. Sun, A. M. Monterrosa, S. A. Maloy, O. Anderoglu, B. H. Sencer, and M. Hackett, "Emulation of reactor irradiation damage using ion beams," *Scripta Materialia*, p. 4, 2014.

[60] K. G. Field, L. M. Barnard, C. M. Parish, J. T. Busby, D. Morgan, and T. R. Allen, "Dependence on grain boundary structure of radiation induced segregation in a 9wt.% Cr model ferritic/martensitic steel," *Journal of Nuclear Materials*, vol. 435, pp. 172–180, Apr. 2013.

[61] M. J. Demkowicz, R. G. Hoagland, B. P. Uberuaga, and A. Misra, "Influence of interface sink strength on the reduction of radiation-induced defect concentrations and fluxes in materials with large interface area per unit volume," *Physical Review B*, vol. 84, p. 104102, Sept. 2011.

[62] E. A. Marquis, R. Hu, and T. Rousseau, "A systematic approach for the study of radiation-induced segregation/depletion at grain boundaries in steels," *Journal of Nuclear Materials*, vol. 413, pp. 1–4, June 2011.